REPORT DOCUMENTATION PAGE

Form Approved
OMB No. 0704-0188

PLEASE DO NOT RETURN YOUR FORM TO THE ABOVE ADDRESS.

1. REPORT DATE *(DD-MM-YYYY)*	2. REPORT TYPE	3. DATES COVERED *(From - To)*
12-01-2021	Thesis	

4. TITLE AND SUBTITLE

Polymer and Concrete Composites in Industrial and Infrastructure Applications

5a. CONTRACT NUMBER

FA8051-20-C-0012

5b. GRANT NUMBER

5c. PROGRAM ELEMENT NUMBER

6. AUTHOR(S)

T. Trevor Painter

5d. PROJECT NUMBER

5e. TASK NUMBER

5f. WORK UNIT NUMBER

7. PERFORMING ORGANIZATION NAME(S) AND ADDRESS(ES)

Luna Innovations Incorporated & Virginia Polytechnic Institute and State University

8. PERFORMING ORGANIZATION REPORT NUMBER

9. SPONSORING/MONITORING AGENCY NAME(S) AND ADDRESS(ES)

Air Force Civil Engineer Center
Readiness Directorate
Requirements and Acquisition Division
139 Barnes Drive, Suite 1
Tyndall Air Force Base, FL 32403-5323

10. SPONSOR/MONITOR'S ACRONYM(S)

AFCEC/CXA

11. SPONSOR/MONITOR'S REPORT NUMBER(S)

AFCEC-CX-TY-TR-2021-0043

12. DISTRIBUTION/AVAILABILITY STATEMENT

DISTRIBUTION A: Approved for public release; distribution unlimited. AFCEC-202101, 12 January 2021

13. SUPPLEMENTARY NOTES

14. ABSTRACT

Composite materials have a wide range of applications in civil and structural engineering due to their advantages in mechanical properties and higher strengths than the base materials alone. Polymer-concrete composites are particularly attractive for use in industrial and infrastructure applications from combining the higher mechanical properties of the concrete in tension and the high tensile strength and ductile properties of the polymeric materials. However, these materials tend to be more expensive than typical concrete composites. This thesis explores the mechanical properties of two different polymer-concrete composites and their effectiveness in civil and structural applications: polymer concrete for rapid repair and 3D printed plastic-concrete composite members for energy absorption.

15. SUBJECT TERMS

Polymers, concrete composites, thesis, infrastructure, composite materials,

16. SECURITY CLASSIFICATION OF:			17. LIMITATION OF ABSTRACT	18. NUMBER OF PAGES	19a. NAME OF RESPONSIBLE PERSON
a. REPORT	b. ABSTRACT	c. THIS PAGE			19b. TELEPHONE NUMBER *(Include area code)*
U	U	U	UU	167	

Polymer and Concrete Composites in Industrial and Infrastructure Applications

T. Trevor Painter

Thesis submitted to the faculty of the Virginia Polytechnic Institute and State University in partial fulfillment of the requirements for the degree of

Master of Science
In
Civil Engineering

Alexander S. Brand, Chair
Eric Jacques
Scott W. Case

December 23, 2020
Blacksburg, VA

Keywords: polymer concrete, rapid repair materials, mechanical properties, composites, 3D printed plastic, bioinspired nacreous materials, cementitious materials, energy absorption

Polymer and Concrete Composites in Industrial and Infrastructure Applications

T. Trevor Painter

ACADEMIC ABSTRACT

Composite materials have a wide range of applications in civil and structural engineering due to their advantages in mechanical properties and higher strengths than the base materials alone. Polymer-concrete composites are particularly attractive for use in industrial and infrastructure applications from combining the higher mechanical properties of the concrete in tension and the high tensile strength and ductile properties of the polymeric materials. However, these materials tend to be more expensive than typical concrete composites. This thesis explores the mechanical properties of two different polymer-concrete composites and their effectiveness in civil and structural applications: polymer concrete for rapid repair and 3D printed plastic-concrete composite members for energy absorption.

The North Atlantic Treaty Organization requires that emergency repair of military runways should be completed within 4 hours. In coordination with Luna Innovations Incorporated, a polymer concrete was developed by Luna for use as a rapid repair material for military runways to meet this requirement through its rapid heat curing. Its mechanical properties including its compressive and flexural strength, bond strength in various orientations, workability, modulus of elasticity, and coefficient of thermal expansion were tested and compared against another rapid repair material.

The Tri-Service Pavements Working Group Manual for rigid repair materials was used as the requirements in determining whether the polymer concrete was an adequate rapid repair material. The polymer concrete formulation that was down-selected for further testing met these requirements for all tests except for the coefficient of thermal expansion. This was due to the resin itself having a high volumetric expansion when exposed to greater temperatures. As the polymer concrete is still under development, future tests are to be performed to determine the impact of the higher expansion on the surrounding runways.

Additionally, inspired from naturally forming nacre found in some seashells, a 3D printed plastic-concrete beam structure was developed and tested in flexure to determine its energy absorption capabilities. The nacreous structure allows the material to experience a strain-hardening behavior, thus allowing for energy dissipation in the beam as it deflects from further applied load. It is theorized that the energy absorption capabilities would be suitable for withstanding the effects of dynamic loadings in structures, such as earthquake and blast loads.

Multiple beam structures were developed and tested to determine the impact of percent-polymeric material and layout had on the energy dissipation. Overall, the specimens with more polymer in the cross-section observed larger load vs. crack mouth displacement curves and fracture energy. These specimens observed a higher toughness as well, making them more suitable for use in structural applications. As the project is still in development, future tests and analysis must be performed to determine their strength properties and feasibility as a structural material.

The implications of this thesis demonstrate the benefits of novel polymer composites in industrial and infrastructure applications, such as improved rapid setting characteristics and significantly enhanced mechanical and energy absorbing performance. Future work is needed to optimize these performance metrics, such as freeze-thaw cycling, fatigue, and durability tests for the polymer concrete and analysis of moment capacity for the bioinspired nacreous composites.

Polymer and Concrete Composites in Industrial and Infrastructure Applications

T. Trevor Painter

GENERAL AUDIENCE ABSTRACT

Composite materials have a wide range of applications in civil and structural engineering due to their advantages in mechanical properties and higher strengths than the base materials alone. Polymer concrete composites are not as widely used due to their more expensive upfront costs. However, they are very attractive for use in industrial and infrastructure applications from combining the higher mechanical properties of the concrete in tension and the high tensile strength and ductile properties of the polymeric materials. This thesis explores the mechanical properties of two different polymer-concrete composites and their effectiveness in civil and structural applications: polymer concrete for rapid repair and 3D printed plastic-concrete composite members for energy absorption.

The North Atlantic Treaty Organization requires that emergency repair of military runways should be completed within 4 hours. In coordination with Luna Innovations Incorporated, a polymer concrete was developed by Luna for use as a rapid repair material for military runways to meet this requirement through its rapid heat curing. Its mechanical properties were tested and compared against another rapid repair material. The polymer concrete formulation that was down-selected for further testing met the requirements of the military for all tests performed except for the coefficient of thermal expansion. As the polymer concrete is still under development, future tests are to be performed to determine the impact of the higher expansion on the surrounding runways.

Additionally, inspired from naturally forming nacre found in some seashells, a 3D printed plastic-concrete beam structure was developed and tested in flexure to determine its energy absorption capabilities. The nacreous structure allows the material to experience a strain-hardening behavior, thus allowing for energy dissipation in the beam as it deflects from further applied load. It is theorized that the energy absorption capabilities would be suitable for withstanding the effects of dynamic loadings in structures, such as earthquake and blast loads. Multiple beam structures were developed and tested to determine the impact of percent-polymeric material and layout had on the energy dissipation. Overall, the specimens with more polymer in the cross-section observed greater energy absorption capabilities. As the project is still in development, future tests and analysis must be performed to determine their strength properties and feasibility as a structural material.

The implications of this thesis demonstrate the benefits of novel polymer composites in industrial and infrastructure applications, such as improved rapid setting characteristics and significantly enhanced mechanical and energy absorbing performance. Future work is needed to optimize these performance metrics, such as freeze-thaw cycling, fatigue, and durability tests for the polymer concrete and analysis of moment capacity for the bioinspired nacreous composites.

Acknowledgements

I would like to deeply thank Dr. Alexander Brand, my committee chair, for his very helpful support and guidance through my research and graduate experience at Virginia Tech. Additionally, a special thanks to Dr. Eric Jacques and Dr. Scott W. Case for serving on my thesis committee.

I also greatly appreciate the contributions of the rest of the faculty, staff, and my classmates at Virginia Tech in helping me during this thesis and graduate school. Special thanks to David Mokarem, Brett Farmer, and Garret Blankenship for their assistance in my time at the structures lab. Thank you to Ebenezer Fanijo, Amir Behravan, and Matt deJong for helping me with tests and assisting me with general lab work, as well as making the lab work more enjoyable.

I extend my gratitude to Luna and its researchers for providing me with a unique project that I would have otherwise never been exposed to and learn from. I would like to directly thank Tyler Farnsworth, Andrew Williams, and Ashley Mullins for their aid and assistance in my research of polymer concrete.

Thank you to Emily Schwab for aiding me in casting and testing of the nacreous beams, as well as for making and 3D printing the plastic molds. I also thank Nicole MacCrate for her contributions to the nacre project and data analysis.

I am also grateful for the contributions of Darya Evans in the editing of my report and her encouragement. Finally, and most importantly, I would like to thank my mother and father, and the rest of my extended family, for their continued and lasting support of me throughout my life and years to come.

This material is based upon work supported by Luna Innovations Incorporated and AFCEC under Prime Contract No FA8051-20-C-0012.

Contents

List of Figures

List of Tables

Abbreviations and Nomenclature

- **ASTM** – ASTM International (formerly the American Society for Testing and Materials)
- **CA** – coarse aggregate
- **COTS –** commercial off the shelf
- **CTE** – coefficient of thermal expansion
- **CTS** – CTS Cement Manufacturing Corporation
- **CTS Concrete –** CTS Cement Rapid Set Concrete
- **cu ft –** cubic feet
- **cu in –** cubic inch
- **DIC** – digital imaging correlation
- **FA** – fine aggregate
- **ft or ’ –** feet
- **g –** gram
- **in or ” –** inches
- **kg –** kilogram
- **kip –** kilo pound
- **ksi –** kilo pound per square inch
- **L –** liter
- **lbf –** pound-force (pound)
- **Luna** – Luna Innovations Incorporated
- **m** – meter
- **mm** – millimeter
- **min** – minutes

- **mL** – milliliter
- **N** – Newton
- **NATO** – North Atlantic Treaty Organization
- **OD** – oven-dried
- **PC** – polymer concrete
- **psi** – pounds per square inch
- **s or sec** – seconds
- **SAP –** silica additive package
- **SSD** – saturated surface dry
- **TSPWG** – Tri-Service Pavements Working Group
- **w/c** – water to cement
- **VT** – Virginia Tech

1. INTRODUCTION

This chapter provides the objective and scope of the testing and analysis performed and the general organization of this thesis.

1.1 Objectives and Scope

Composite materials have been widely in use throughout civil engineering due to their advantages of higher strength properties of the composite material over the individual components themselves. The use of composites also allows unique properties of the material through geometric properties of the material matrices and composite action of the individual ingredients. Composites are also beneficial in industrial and commercial use as the introduction of cheaper ingredients can alleviate the overall cost of the composite material rather than the use of a single more expensive material. An example of this is through the addition of coarse and fine aggregates in concrete, which make the cost per volume of the mix more inexpensive as compared to cement paste alone, even offering additional strength properties depending on the strengths of the aggregates.

Polymer and concrete composites are particularly attractive for use in industrial and infrastructure applications as they can combine the higher mechanical and strength properties of the concrete in compression and the high tensile and ductile properties of the polymeric materials. This thesis reviews two particular polymer-concrete composites and their respective applicable uses: polymer concrete as a repair material and 3D-printed plastic-concrete composite beams used for energy absorption.

1.2 Organization of Thesis

This thesis will present the use of polymer and concrete composite materials in industrial and infrastructure applications, including repair materials and energy absorbing beam elements, and

how effective these materials are in their respective uses. The thesis has been split into two sections. Section I discusses the material properties of polymer concrete (PC) for repairs of military runways. Section II explores the use of 3D-printed plastic-concrete composite beams for energy dissipation.

Chapter 1 provides context towards the project and outlines the thesis structure. Background information for both sections of thesis and how each composite explored is relevant for use in industrial and infrastructure applications.

Chapter 2 provides further background in the development of polymer concretes, including its critical ingredients, strength properties, advantages over typical cementitious concretes, and applications and uses. Context for the bioinspired nacre structure and its advantages are also introduced and discussed.

Chapters 3 through 6 pertain to the development of the polymer concrete in Section I. Chapter 3 reviews the materials used in the formulations for the concretes tested. The mix designs, casting procedures, and curing procedures were also outlined. Chapter 4 discusses each of the tests performed on each of the repair materials being compared. Each test was separated into subsections, where the test procedure, results and observations, and conclusions from the tests were discussed. Chapter 5 summarized the results of all tests performed and provides a comparison of the two down-selected repair materials. Comparison of the materials at a cost basis was also performed and discussed. Final conclusions and recommendations were then summarized. Chapter 6 expands on the recommendations by describing future work to be performed on the development of the polymer concrete.

Chapters 7 through 10 pertain to the bioinspired 3D printed plastic-concrete composites in Section II. Chapter 7 outlines the materials used, casting procedures, and testing procedures for the 3D printed plastic-concrete composite members developed. Chapter 8 reports and discusses the results and observations from the tests. Chapter 9 summarizes the findings from the tests performed to compare each of the members and state any current conclusions of the bioinspired structure for structure energy absorption. Chapter 10 describes the future work for the project and lists any recommendations for further testing of the 3D printed plastic-concrete composites.

The attached appendices include photos of the test specimens for both Sections I and II. The raw data from the modulus of elasticity tests in Section I have also been included in the appendices.

1.3 Section I: Material Properties of Polymer Concrete for Repairs of Military Runways

When an airfield is damaged due to an airstrike, various craters are left in the runway slabs that must be repaired prior to any further operations. According to the current North Atlantic Treaty Organization (NATO) crater repair standard, the airfield should be recovered within 4 hours of the attack for emergency operations [1]. Current repair materials used by the U.S. Air Force do not meet this standard, as studies have shown that an average of 8 hours was needed to repair a large crater, which have primarily concerned the use of various types of rapid setting cement-based concrete [2].

To meet the NATO standard, a polymer concrete (PC) was developed by Luna Innovations Incorporated (Luna). Through the use of external heat curing, the Luna PC was able to achieve a usable concrete within minutes of the initial pour. In addition to the rapid curing time, other critical considerations were taken into account when developing the PC. The mix was designed to be easily

workable and mixed, so that the repair could be performed by a small man crew and using readily available tools, such as a mixing drum and trowels. The repair must have adequate bond with the existing runway concrete, so the slab can act compositely, and no further damage of the existing concrete would be observed. The repair material was also designed to withstand the rolling load of the aircraft through its high strength properties.

1.4 Section II: Energy Dissipation of 3D Printed Plastic-Concrete Composite Beams

For structures subjected to dynamic loadings, such as earthquakes or blast loadings, energy dissipation is needed to reduce the impact of these loads and protect the occupants. This is especially true for blast loadings, where the explosions can cause immediate damage and high velocity shrapnel if the energy of the explosions is not dissipated through the structure or its members. Energy dissipation is typically achieved through the use of plastic deformations in the member, as its ductility allows for the overall deflection and local deformations to absorb the energy prior to rupture. This can also be coupled with strain-hardening behaviors in the stress-strain curve, where more applied load is needed to further deform the member, allowing for even more energy to be dissipated in the member as it is being deformed.

Typical concrete without any reinforcement is inherently brittle and very weak under tension. As a result, concrete does not dissipate much energy when experiencing flexure due to its very limited load-deflection curve. To increase the ductility of the concrete, a 3D-printed plastic-concrete composite beam structure was designed inspired by a naturally forming material known as nacre.

Nacre is naturally formed in seashells where its microscopic structure produces an overall material that has high energy dissipation. The structure has a “brick-and-mortar” type of

architecture where aragonite platelets are surrounded in three-dimensions by thin organic joints [3–5]. In this architecture, the aragonite platelets act as the "bricks" that are irregularly stacked and connected with the organic material which acts as the "mortar," as observed in Figure 1.1 and 1.2.

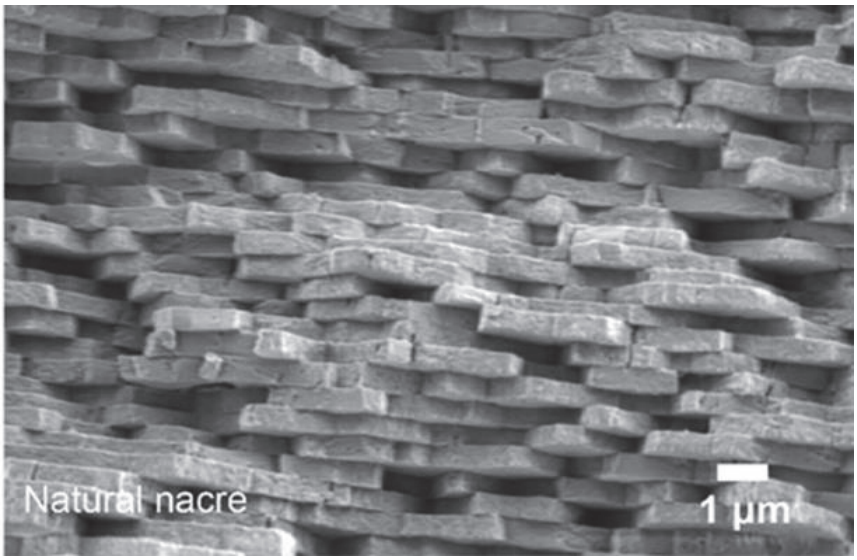

Figure 1.1: Electron Micrograph of "Brick-and-Mortar" Architecture of Natural Nacre from Biswas et al., 2017 [3]

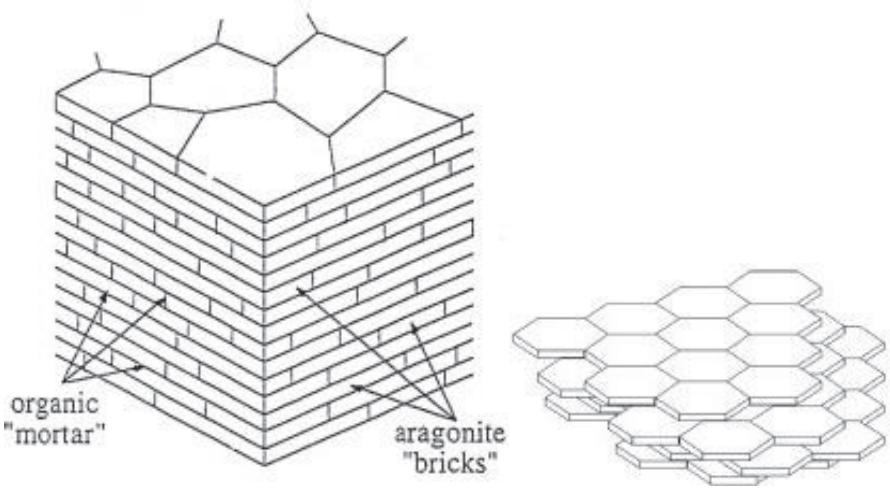

Figure 1.2: Ideal Schematics of Platelet Arrangements from Sarikaya, 1994 and Meyers et al., 2008 [4,5]

While independently these materials are relatively weak, under this structure, the composite material has increased stiffness, strength, and toughness [6]. This can be attributed to the structure artificially increasing the required crack length needed to rupture the member as it goes between or through the bricks. The architecture enables plastic deformations of the overall material to occur and introduces a strain-hardening type behavior to the material.

To simulate the nacreous structure, a high strength cement paste was used as the "bricks" with the 3D-printed plastic as the "mortar." The 3D-printed plastic also acted as the mold to form and bond with the cement paste bricks. Previous studies have shown that concrete with 3D-printed formworks can be substituted for steel reinforcing and produce similar behaviors in the ductility of the beams [7].

2. LITERATURE REVIEW

2.1 Polymer Concrete

PC is a composite material in which the hydraulic cementitious binders of conventional cement-based concrete are replaced by polymer binders, and it is a type of concrete-polymer composite. Generally, the same aggregates that are used in cementitious-based concrete are acceptable for use in PC. The major difference is that the aggregates must be well-graded to minimize the required resin, and thereby additional costs, to reduce the void ratio of the concrete. PC is advantageous for its higher strength properties than typical cement-based concretes but is more expensive from employing polymer binders rather than Portland cement [8,9].

2.1.1 Polymeric Resin Binders and PC Ingredients

Liquid resins are the principal polymeric binder in PC. While various types of resins have been used in PC, the most common are thermosetting resins due to their high thermal stability. A summary of the types of resins used is shown in Figure 2.1. Among the thermosetting resins, epoxy resins are the most widely used due to their strong adhesion, low shrinkage, creep and fatigue resistance, and low water sorption [10–12].

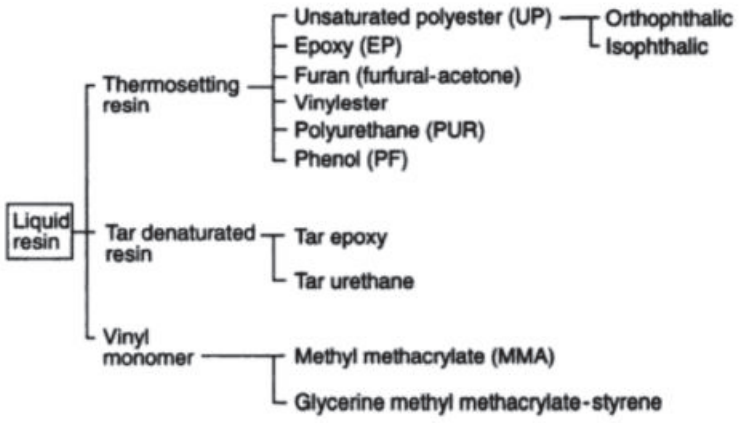

Figure 2.1: Types of Liquid Resins used in Polymer Concrete from Kim, D., 1995 [12]

For most PC formulations, the percentage of resin required by weight ranges from 9-25% with more resin increasing the overall strength properties of the mix [12]. The aggregates used must be dry and free of organic materials, as the addition of either reduces the overall bond strength of the polymeric binder and the aggregates [8,10]. The use of fly ash, silica fume, and other waste products is acceptable for use in PC and beneficial since they improve the physical properties of the formulation, in particular the compressive and flexural strengths [13,14].

The natural curing time of PC is generally less than one day and can be accelerated even further through controlled temperatures and the addition of chemical additives such as catalysts. Inclusion of such additives can increase curing time within hours or minutes of the initial cure once subjected to the controlled temperatures [10,12].

2.1.2 Strength Properties

Polymeric binders strongly bind to the aggregates in the PC. This creates a homogenous, densely-packed composite material that overall increases the strength properties of the material relative to typical cementitious-based concrete composites. Much like cementitious concretes, the properties of the PC differ greatly on its mix and formulation. Both the compressive and flexural strengths of the PC are dependent on the resin content and increase with the increase in polymer content [15–18]. The increase in strength diminishes with the increase in resin content, where these strengths either decrease or remain relatively constant after reaching the peak. It is observed that maximum flexural and compressive strength is typically obtained between 14 and 16% resin weight percent [16,19].

There have been a limited number of studies of the fatigue behavior of PC. Of those, the two-million cycle fatigue endurance limit has been reported as a stress level of 59% [20]. This is

very similar to cementitious concretes, making PC a viable alternative for fatigue scenarios with higher applied loads or stresses, due to its inherent higher compressive and flexural strengths.

2.1.3 Applications and Cost Benefits

Due to the use of polymers as the binder rather than typical Portland cement, PC typically costs substantially more than conventional cement-based concretes. The resin itself is the driving factor in the overall cost due to its own high cost to manufacture, while recycled plastic waste may be included in the overall resin mixture to help reduce the cost [21–23]. As such, PC is used only in applications where the increased cost is outweighed by its superior material properties and/or the need for rapid setting.

In general, the use of PC as a repair material for deteriorated or damaged structures is the most cost-efficient application for the material. This is due to its high moisture and corrosion resistance, making it very suitable for pavements, buildings, bridges, slabs, and dams [24–28].Previous studies have shown that PC is a suitable repair material for military runways, specifically from its improved durability and high strength and adhesion properties to the existing concrete [29–31]. The largest deterrent in using it as a consistent repair material is its upfront costs. However, from its increased durability, it was theorized that the initial costs of the PC could be offset by the minimal maintenance on the patches over time leading to future potential cost savings [31,32].

2.2 Nacreous Bioinspiration

Naturally forming nacre, found in certain seashells, has an overlapping and offset “brick-and-mortar” microstructure, as observed in Figures 1.1 and 1.2. The platelets are made of aragonite, a calcium carbonate ($CaCO_3$) polymorph, and are bound by a protein. By volume, the composition is approximately 95% platelets and 5% protein [33]. The aragonite platelets are hexagonal in shape

with a diameter ranging from 5 to 8 μm and a thickness ranging from 200 to 900 nm. The protein surrounding the platelets is approximately 10 to 50 nm thick [5,33].

2.2.1 Material Properties

From the layout of the platelets and protein, nacre exhibits much greater toughness and strength properties than either of the individual components [34]. The total fracture energy of nacre was found to be up to 2000 to 3000 times greater than monolithic $CaCO_3$ [5,33]. The Mode I critical facture toughness (K_{Ic}) can be up to 20 to 40 times greater than monolithic $CaCO_3$ [5,33]. The strength and modulus of the nacre depends on the platelet volume and its aspect ratio. Figure 2.2 summarizes the increase in the tensile strength and modulus, comparing the experimental data with the predicted strengths.

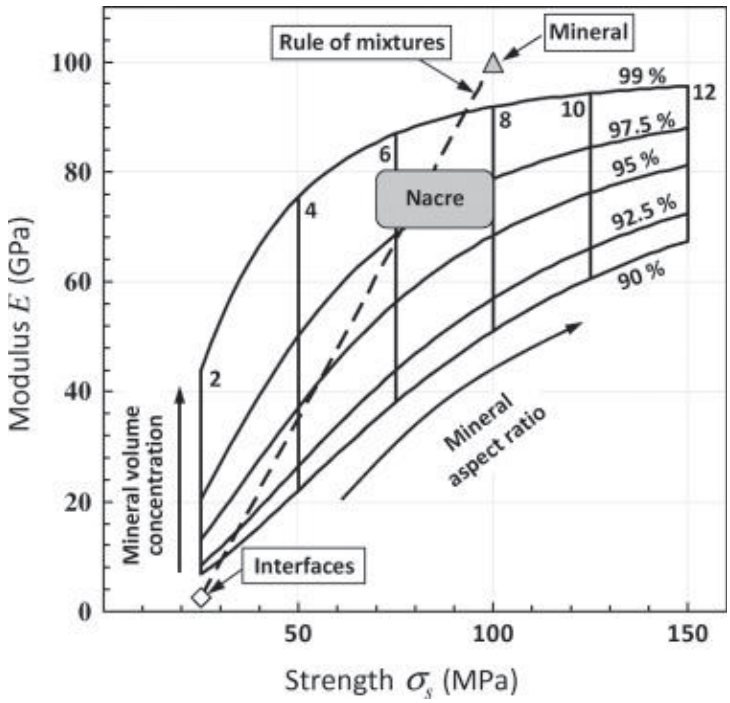

Figure 2.2: Strength and Elastic Modulus of Nacre with Increasing Platelet Volume and Aspect Ratio from Barthelat et al., 2011 [6]

Due to its microstructure, nacre experiences anisotropic behavior, meaning its strength varies depending on the direction of loading or how the object is oriented. When perpendicular to

the platelets, the nacre has compressive and tensile strengths around 540 MPa and 5 MPa [5], respectively. However, when parallel with the platelets, the nacre experiences compressive and tensile strengths around 235 MPa and 170 MPa, respectively [5].

Recent data on the structure of nacre have suggested that "brick-bridge-mortar" is a more accurate description of the nacre microstructure rather than "brick-mortar." This is due to the mineral bridges between the "bricks" have shown to have a significant impact on the mechanical properties of nacreous materials [35]. This unique stacking microstructure allows nacre to undergo substantial plastic deformations prior to failure and exhibit strain-hardening behaviors [36].

Nacre attributes its superior toughness over monolithic $CaCO_3$ to four primary mechanisms as shown in Figure 2.3. These mechanisms allow the microstructure of nacre to dissipate local stresses while also allowing for ductile behavior without great loss in strength.

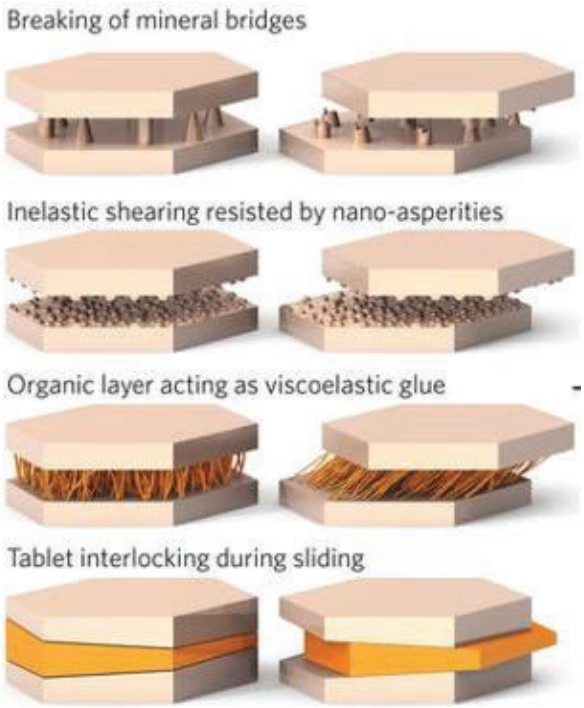

Figure 2.3: Four Main Mechanisms in Nacre that Result in its High Toughness from Wegst et al., 2015 [33]

2.2.2: Energy Absorbing Composites under Static and Dynamic Loading

Most research of nacreous bioinspired materials has considered the nano- or microstructural aspects of biomimicry with few studies scaling to tens of centimeters [37]. For civil and structural applications in industry, the energy absorption and dissipation benefits of nacreous design would need to be scaled up to an order of meters.

Current structural applications requiring greater energy absorption capacity consider the addition of discrete fibers to the concrete composites. These fibers include steel, glass, polymer, and carbon fibers, among others. Fiber reinforced concrete has been shown to improve the fracture toughness properties of brittle concrete. This is due to the transferring of the tensile loads to the fibers, which bridge the crack openings of the concrete as the member deforms [38].

2.3 Digital Image Correlation

Stereo-digital image correlation is a tool that is used to measure and calculate local strains and displacements along the face of various members. This is an optical method which compares photos over a time interval and tracks the change in shape and location of multitudes of reference nodes [39]. To properly use the digital image correlation (DIC) method, the surface of the material being analyzed must be sprayed with a contrasting speckle pattern so individual nodes and areas may be referenced by the DIC. Figure 2.4 shows an example of this speckling pattern with black spots on a white background.

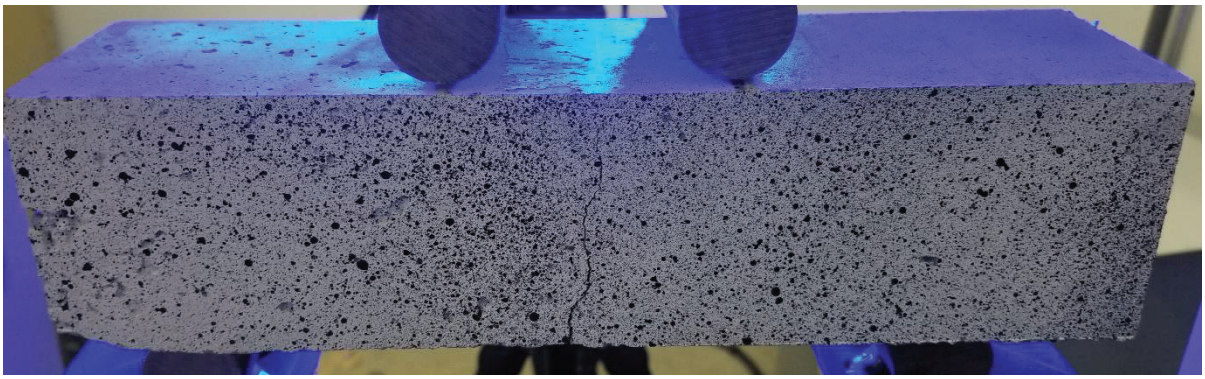

Figure 2.4: Speckle Pattern Applied to Beam Specimen

By tracking the speckles as individual nodes on the specimen's surface, the DIC can measure plastic deformations and monitor crack initiations and propagations through the specimen [40]. The speckling pattern tracked over time using the DIC can also determine the strains at any location or region on the surface. By identifying a reference image or stage, the strains are determined by their displacement relative to the reference as illustrated in Figure 2.5.

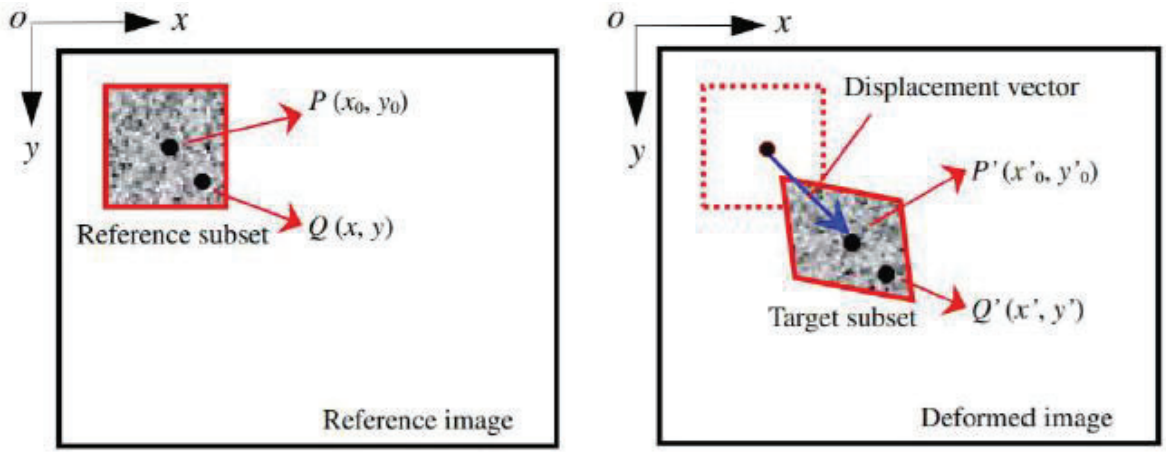

Figure 2.5: DIC Strain and Displacement Calculations from Speckle Pattern and Reference Stage from Pan et al., 2010 [41]**.**

Through post-processing each frame taken against the reference stage, the strains can be analyzed at a more localized or global level from altering the density of the subset grid or the point distance. While the DIC is a powerful non-contact method, many sources of error can be accumulated through poor resolution, camera angles, and lighting. The test surface must also be

properly prepared to prevent any additional error. Considerations about the surface such as its smoothness and the proper contrast of the speckle pattern must be taken into account [42].

Section I: Material Properties of Polymer Concrete for Repair of Military Runways

3. SECTION I: MIX DESIGN AND CASTING PROCEDURE

3.1 Concrete Materials

3.1.1 Luna Polymer Concrete

An epoxy-based resin was used in both Phases I and II as the binder for the PC. The mix design developed by Luna is proprietary, so the exact formulation of the resin, as well as their proportions, will not be included in this thesis.

In Phase I of developing the polymer concrete, the coarse aggregate (CA) consisted of locally sourced ASTM C33 #78 graded dolomite having a maximum diameter of 1/2 inch [43]. Phase II focused on down-selecting the types of aggregates to be used. To vary the CA, locally sourced #57 graded dolomite, #68 graded dolomite, and #68 graded granite were used in some mixes. The maximum diameter of each CA was 1¼ inches, 3/4 inch, and 3/4 inch, respectively. For both Phases I and II, the fine aggregate (FA) used was a well-graded, locally sourced natural sand.

For each mix of PC, the bulk density (specific gravity) and absorption capacity of the aggregates influenced the weight proportions of the CA and FA as well as the resin. To determine these values, ASTM C127 [44] was performed on each CA and ASTM C128 [45] was performed on the FA used. These tests were performed only once to obtain a rough estimate for the densities and the absorption of each aggregate. A summary of the bulk specific gravity and absorption of each of the aggregates can be found in Table 3.1.

Table 3.1: Bulk Specific Gravity and Absorption of Aggregates

Aggregate	Bulk Specific Gravity	Absorption (%)
#78 Dolomite	2.72	1.07%
#68 Dolomite	2.59	1.28%
#57 Dolomite	2.54	1.47%
#68 Granite	2.50	1.65%
Natural Sand	2.61	1.08%

Previous trials observed that foaming of the resin occurred when moist aggregates were used, likely attributed to the high temperature curing. This severely impacted the integrity of the mix and effectively made the mix unusable. Due to this, each of the coarse and fine aggregates were oven-dried (OD) at a temperature of 100°C (±5°C) for at least 16 hours to ensure no moisture was present in the aggregates. Oven-dried bulk density of the aggregates was then used in any subsequent calculations for proportioning the mixes.

To prevent separation of the resin and the aggregates, an amorphous silica was included in the mixes developed in Phase I and some mixes in Phase II. The amorphous silica has an extremely low bulk density, which produces a strong thickening effect [46]. This effect helps reduce the separation of the resin and the aggregates and reduces seepage of the resin.

Other types of silica products were also included to increase the packing density of the PC from their reduced particle size [47–49]. The silica products are characterized by very high surface area to volume ratio from their small particle size. The exact silica materials used in development of the PC and their proportions will not be disclosed in this thesis, as this information is proprietary. The combined silica materials were noted as silica additive packages (SAP) when included in the Luna PC mixes, to differentiate between similar mix designs.

A catalyst was included in the mixes to increase the rate of the chemical reaction which cures the PC. The addition of the catalyst allows the PC to cure rapidly if exposed to a heat source. Without a heat source, the catalyst will cure the PC within approximately 16 hours at room temperature. In addition to the resin, the specific catalyst used in design, as well as its proportion in the PC mixes, will not be disclosed in this thesis as this information is proprietary.

3.1.2 CTS Cement Rapid Set Concrete Mix (CTS Concrete)

The CTS Cement Rapid Set Concrete (CTS concrete) is a patching material that has been tested and researched for use by the military in the rapid repair of runways [2,50,51]. To compare the results and performance of the Luna polymer concrete, each test was also performed on CTS concrete specimens.

A 60-pound bag of CTS Cement Rapid Set Concrete Mix was used for each batch of CTS concrete. This mix contained a proprietary rapid setting calcium sulfoaluminate cement, 3/8 in. coarse aggregates, and fine aggregates. One 60-pound bag requires 3.5-4.0 quarts of water to properly set and cure.

3.1.3 Typical Cement-Based Concrete

Because the PC will be used as a repair material, some tests required the formulation of a typical concrete mix for military runways to simulate the bond strength of the repair material with the existing runway concrete. For these mixes, a locally sourced ASTM C150 Type I/II Portland cement was used as the binder [52].

The coarse aggregate was a locally sourced dolomite #78 stone. The CA had a maximum diameter of 1/2 inch. The fine aggregate used was a locally sourced, well-graded natural sand.

Both the coarse and fine aggregates were the same as the CA and FA used in the Phase I formulation of the Luna polymer concrete.

The mix design for the typical concrete required a low water-to-cement (w/c) ratio. To improve the workability of the mix, approximately 30 mL of a polycarboxylate-based superplasticizer was introduced.

3.2 Mix Design

3.2.1 Luna Polymer Concrete – Phase I

In Phase I, the resin was proportioned to be 17 wt.% of the total concrete weight. A coarse-to-fine aggregate weight ratio of 60:40 was used with OD aggregates. Various types of silica particles were proportioned and combined to form a silica additive package (SAP) included with the resin. The SAP was not included in the calculations of the total concrete weight for proportioning the resin due to its low density and small proportion in the mix, less than 5 wt.% of resin. The catalyst was also proportioned relative to the weight percent of the resin and not included in total weight calculations. The mix data for a typical 5-gallon bucket of the PC developed in Phase I is shown in Table 3.2.

3.2.2 Luna Polymer Concrete – Phase II

Many mixes were created in Phase II to down select a better mix for strength, workability, and to potentially reduce the amount of resin and fumed silica to lower the overall cost of the PC. In each mix, the coarse-to-fine ratio remained constant at 60:40 of OD aggregates, the same ratio used in Phase I.

To down select the final mix, the resin weight percent, type of CA used, different proportions of the SAP, and amount of catalyst were all factors that varied between mixes. The

mix used in Phase I acted as the control mix. The addition of SAP or the catalyst were not included in the total weight of the PC when calculating the weight of the resin, as in Phase I. Table 3.2 shows the material proportions of a 6.5-liter mix for each formulation developed in Phase I and II.

Table 3.2: Material Weight Proportions for 6.5 Liter Mix

Concrete Mix	Material Weight (g)			
	Coarse Aggregate	Fine Aggregate	Resin	Total
Luna PC Phase I: 17 wt.% Resin w/ SAP 1	7189	4793	2454	**14436**
Luna PC Phase II: 17 wt.% Resin w/ #68 Dolomite	7042	4695	2404	**14142**
Luna PC Phase II: 17 wt.% Resin w/ #57 Dolomite	6982	4655	2383	**14020**
Luna PC Phase II: 17 wt.% Resin w/ #68 Granite	6940	4627	2369	**13935**
Luna PC Phase II: 10 wt.% Resin w/ #78 Dolomite	8381	5587	1552	**15520**
Luna PC Phase II: 10 wt.% Resin w/ #68 Dolomite	8183	5455	1515	**15153**
Luna PC Phase II: 10 wt.% Resin w/ #57 Dolomite	8101	5401	1500	**15002**
Luna PC Phase II: 10 wt.% Resin w/ #68 Granite	8044	5363	1490	**14897**
Luna PC Phase II: 12 wt.% Resin	8022	5348	1823	**15194**
Luna PC Phase II: 15 wt.% Resin	7512	5008	2209	**14730**
Luna PC Phase II: 17 wt.% Resin w/ SAP 3	7189	4793	2454	**14436**
Luna PC Phase II: 17 wt.% Resin w/ SAP 4	7189	4793	2454	**14436**

3.2.3 Typical Cement-Based Concrete

This concrete mix was developed to simulate the properties of a typical airfield concrete pavement. The mix was designed to have a 7-day compressive strength of 4,500 psi. A low w/c ratio was used to achieve this higher strength and durability. The mix design for a typical 1 cu ft batch is shown in Table 3.3. OD aggregates were used, thus increasing the required water to achieve the desired w/c ratio.

Table 3.3: Typical Cementitious-Based Concrete Mix Design

Material Weight (lbf)				
Coarse Aggregate	**Fine Aggregate**	**Cement**	**Water**	**Total**
62.2	53.0	22.2	11.0	**148.4**
w/c ratio = 0.437				

3.3 Casting and Curing Procedure

3.3.1 Luna Polymer Concrete

For small scale mixes (≤ 10L), the polymer concrete was mixed in a 5-gallon bucket using an electric, handheld, single-paddle concrete mixer, shown in Figure 3.1. Larger scale mixes (> 10L) were mixed using a 3.5 cu ft epoxy drum mixer. The mixer consists of a thick polyethylene drum to prevent adhesion of the resin and easier clean up, as shown in Figure 3.2.

Figure 3.1: Electric Handheld Single-Paddle Mixer

Figure 3.2: Epoxy Drum Mixer

The resin was proportioned first in a 5-gallon bucket and then mixed using a trowel or handheld mixer until homogenous. Afterwards, if any SAP was present in the mix, it was weighed and added to the resin. The bucket was then covered using aluminum foil around the mixer to prevent the silica particles from escaping, as it was being mixed, due to their very low densities. The SAP was mixed for 5 to 15 minutes or until homogenous with the resin. The catalyst was then weighed, introduced, and mixed with the resin until homogenous. Figure 3.3 shows the resin mixed in the 5-gallon bucket.

Figure 3.3: Resin Being Mixed in a 5-gallon Bucket

Both the coarse and fine aggregates were weighed and measured in individual 5-gallon buckets prior to or during the mixing of the resin ingredients. Once the resin had been completely mixed, the coarse aggregates were introduced in two half-weight flights. The first flight of CA was then mixed with the resin until uniform, after which the second flight of CA was introduced and mixed completely. Subsequently, the fine aggregate was included in two half-weight flights, both being mixed until homogenous with the polymer concrete before the addition of more ingredients Figure 3.4 shows the CA after being mixed into the PC and the PC being mixed after the addition of FA.

Figure 3.4: Luna PC Mixed After the Addition of CA (left) and FA (right)

Before any PC was poured into the molds, a releasing agent was applied to each preventing the permanent adhesion of the PC to the steel molds and to help with demolding. All cylinder specimens were cast in three lifts of equal depth and all beam specimens were cast in two lifts of equal depth. Each specimen was compacted by hand tamping and rodded in accordance with ASTM C31 [53]. Once the specimens were cast and the exposed surfaces were smoothed with a trowel, the specimens were then placed in an oven set to a temperature of 100°C (±5°C) and

allowed to heat cure for 1 hour. After heat curing, the specimens were removed from the oven and cooled at room temperature for a minimum of 1-hour. Once cooled, the specimens were demolded prior to testing. Figure 3.5 shows various PC specimens cooling after cure prior in steel molds.

Figure 3.5: Luna PC Specimens Cured and Cooling Prior to Demolding

3.3.2 CTS Concrete

A drum mixer was used to mix the CTS Concrete, as shown in Figure 3.6. The 60-pound bag was emptied inside the drum and 4.0 quarts of water were added and mixed for approximately three (3) minutes or until a uniform mixture was noted. All cylinder specimens were cast in three lift and all beam specimens were cast in two lifts. Each specimen was compacted by hand tamping and rodded in accordance with ASTM C31. Once the specimens were cast and the exposed surfaces were smoothed with a trowel, the specimens were then either covered with plastic or placed in a moist curing room to ensure proper curing and prevent loss of moisture. Once cured, the specimens were demolded prior to testing.

Figure 3.6: CTS Concrete Mixed in Drum Mixer

3.3.3 Typical Cement-Based Concrete

A drum mixer was used to mix the typical concrete. All ingredient proportions were weighed and measured prior to their addition into the mix. The coarse and fine aggregates were the first ingredient added to the drum. After the addition of some water to lubricate the blade and the aggregates, the aggregates were mixed until uniform. The cement was then added and mixed into the aggregates along with half the remaining water. The mixer was run for approximately three (3) minutes, after which the remaining water was added to the mix. Due to the low w/c ratio, a superplasticizer was then added to increase the workability of the concrete and allow for easier molding of the specimens.

The cylindrical specimens were cast in three flights of equal depth and all beam specimens were cast in two flights. Each specimen was compacted by hand tamping and rodded in accordance with ASTM C31. Afterwards, the exposed surfaces were smoothed with a trowel. To ensure proper curing of the concrete and prevent loss of moisture, the specimens were either covered with plastic

or placed in a moist curing room. After one day of curing, the specimens were demolded and placed back into the moist curing room. The specimens were cured for a minimum of seven (7) days prior to use or testing.

4. SECTION I: TEST PROCEDURES AND RESULTS

This section will review the different tests performed in Phases I and II of the formulation of the Luna polymer concrete. The test methods and procedures are summarized for each test, as well as the results from each test and any empirical observations. Individual conclusions were also made for each test as the results from some influenced the down selection in subsequent tests.

Phase I results have been summarized separately from tests performed in Phase II, as needed, for clarity in showing how the Luna polymer concrete performed relative to the current repair patching material in the CTS concrete. A summary of results from both phases was included to compare the different PC formulations against each other as well as the CTS concrete.

Phase I of the formulation of the Luna PC tested the compressive and flexural strengths of the patch alone. The bond strength of the patch against typical concrete used in military runways was also tested. The shear bond strength was tested, as well as both the horizontal and vertical flexural bond strengths.

Phase II of the project was focused on workability of the PC and how different formulations and proportions of the ingredients will impact the workability as well as previously tested material strengths. The compressive, shear bond, and flexural strengths were all tested again in Phase II using the down selected mixes to compare the new formulations to the mix design of Phase I.

In addition, during Phase II, the modulus of elasticity was tested to determine the rigidity of the repair material. The coefficient of thermal expansion (CTE) was also measured, as PC tends to expand more than cement-based concrete when exposed to a wide range of temperatures. A higher CTE is a potential issue as it could lead to the repair material debonding with the existing runway concrete as the patch experiences heating and cooling cycles. To determine the effects of

temperature cycling on the bond strength, the shear bond strength and vertical bond strength of the PC were also tested after the specimens experienced five (5) freeze-thaw cycles.

All specimens were cast at the Thomas M. Murray Structures and Materials Laboratory at Virginia Tech (VT) or at the Luna Innovations Incorporated Blacksburg laboratory. All tests were either performed at the Thomas M. Murray Structures and Materials Laboratory or the Norris Laboratory at VT. Special care was taken to ensure each batch of concrete was as nearly identical as possible.

4.1 Compressive Strength

The compressive strength of each of the repair materials was tested to determine whether the mixes could withstand the applied load of military aircraft that would pass over the patch materials. Because the patching materials will be used for rapid repairs, high early strength of the concretes is most desirable, so specimens of different curing times were tested to determine their early strengths. In Phase II, different formulations of the Luna PC were tested to determine how different materials and their proportions would impact the strength of the concrete. The results of each test were compared against one another to determine the best mix for the Luna PC.

4.1.1 Test Method and Procedure

All cylindrical compressive tests were performed in accordance with ASTM C39 [54]. A hydraulic press applied a constantly increasing compressive force on each specimen as can be seen in Figure 4.1.1. Each specimen was loaded at a rate of 35 psi/s until the specimen strength decreased to 70% of the ultimate applied load or failure occurred. The ultimate load applied on each specimen was recorded. The compressive strength was determined using Equation 1:

$$f_{cm} = \frac{4P}{\pi D^2} \quad (1)$$

where f_{cm} is the recorded compressive strength of the specimen in psi, P is the ultimate applied load in lbf, and D is the average measured diameter of the specimen in inches.

Figure 4.1.1: Compression Testing Apparatus at the VT Structures Lab

All 2" cube specimens were tested following the procedures of ASTM C109 [55] and C579 [56] for the CTS concrete and Luna PC specimens, respectively. The ultimate load applied on each specimen was recorded. The compressive strength was determined using Equation 2:

$$f_m = \frac{P}{A} \quad (2)$$

where f_{cm} is the recorded compressive strength of the specimen in psi, P is the ultimate applied load in lbf, and A is the average area of the specimen in square inches.

In Phase I, (3) 2” cubes were cast for both the CTS concrete and the Luna PC and then tested in compression after seven (7) days of curing. Figures 4.1.2 and 4.1.3 show a 2” cube specimen both before and after testing for both the CTS concrete and the Luna PC, respectively.

In both phases, (3) 3” diameter by 6” tall cylinder specimens were made for the CTS concrete and various down selected Luna PC mixes. The first set of CTS cylinders were capped using 4” diameter rubber caps prior to testing. All other cylindrical specimens were capped using poured sulfur caps prior to testing. Figures 4.1.4 and 4.1.5 show a side-by-side comparison of 3” cylinder specimens of the CTS concrete and the Phase I Luna PC, respectively, prior to and immediately after testing.

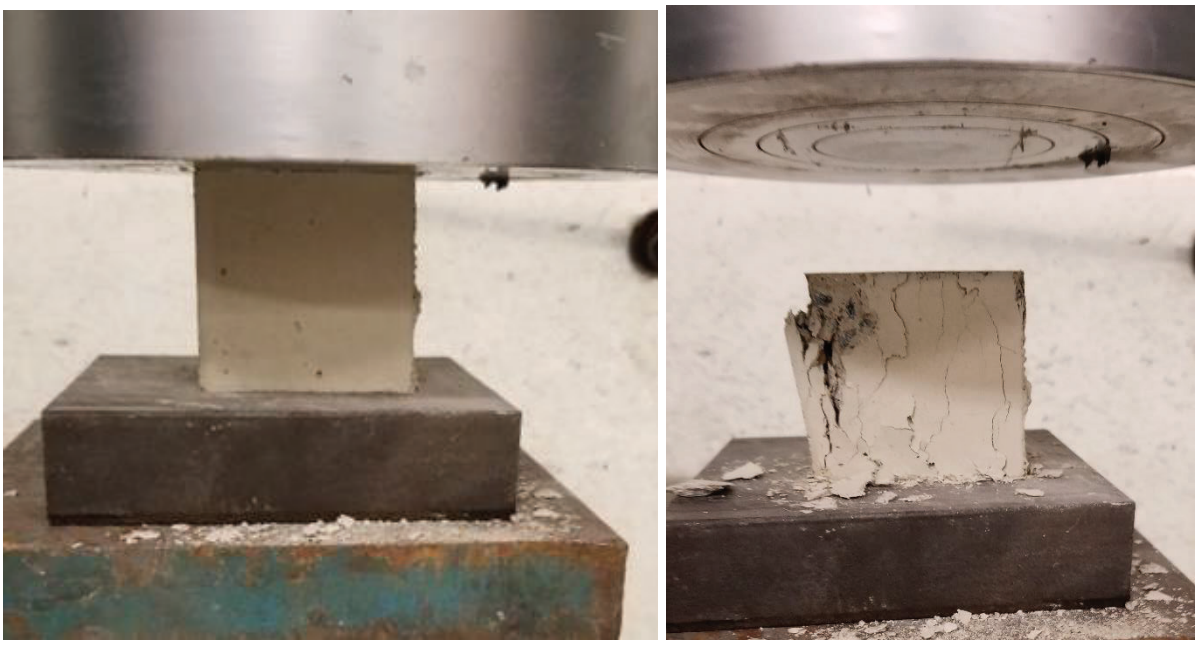

Figure 4.1.2: CTS Concrete 2” Cube Prior to Testing (Left) and After Testing (Right)

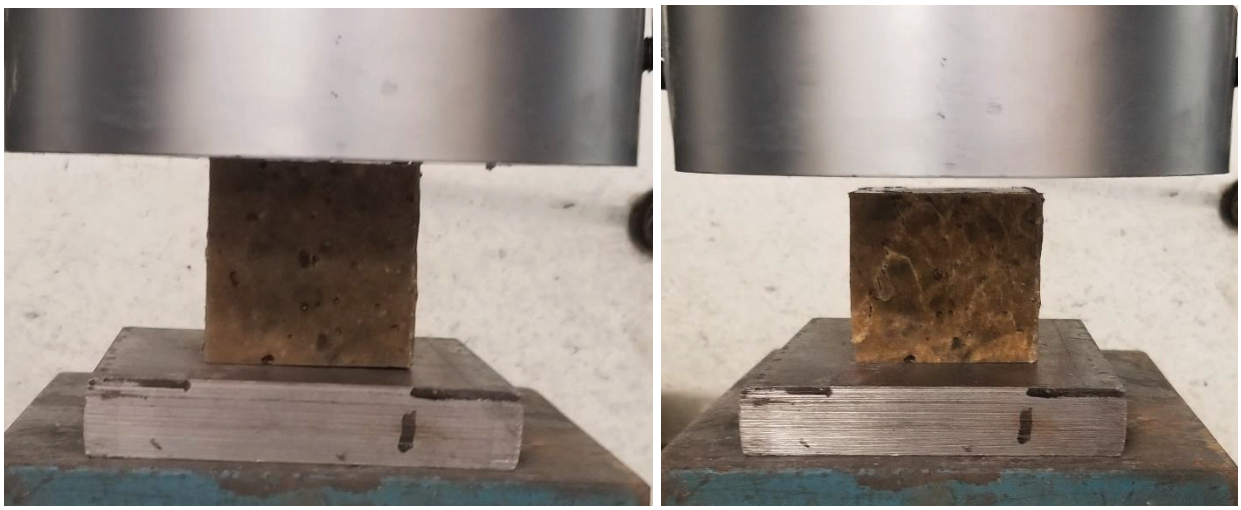

Figure 4.1.3: Phase I – Luna PC 2” Cube Prior to Testing (Left) and After Testing (Right)

Figure 4.1.4: CTS Concrete 3” Cylinder Prior to Testing (Left) and After Testing (Right)

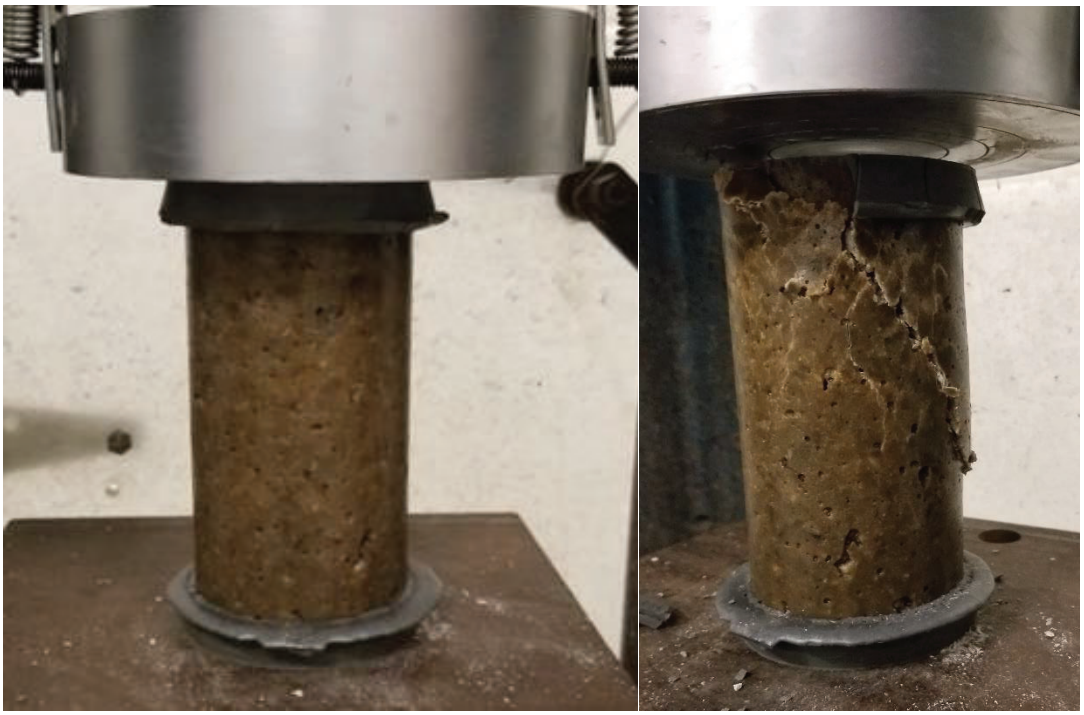

Figure 4.1.5: Phase I – Luna PC 3" Cylinder Prior to Testing (Left) and After Testing (Right)

4.1.2 Results and Observations

The compression test results for the 2" cube specimens are summarized in Table 4.1.1 and is organized by the concrete mix. The recorded compressive strength was rounded to the nearest 10 psi. The average and standard deviation for each of the mixes was calculated and recorded. These results have been plotted in Figure 4.1.6.

Table 4.1.1: Compressive Strength Results for 2" Cubes

Concrete Mix	Specimen Identifier	Ultimate Load, P (lbs)	Compressive Strength, f_m (psi)	Average Compressive Strength (psi)	Standard Deviation (psi)
CTS Concrete	1	16317	4080	4340	220
	2	17920	4480		
	3	17792	4450		
Luna PC Phase I: 17 wt.% Resin w/ SAP 1	A	59569	14890	14760	150
	B	58361	14590		
	C	59183	14800		

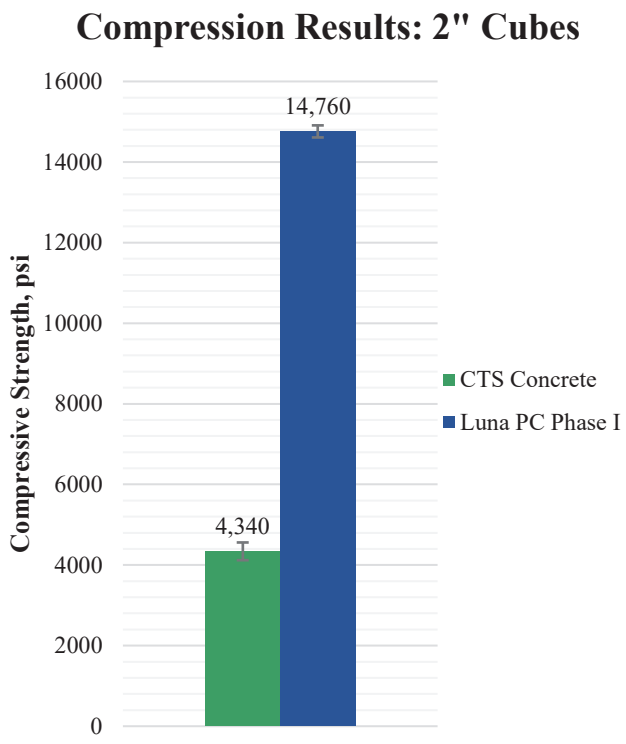

Figure 4.1.6: Compressive Strength Results for 2" Cubes

When testing the 2" cubes, spalling of the concrete was noticed for each of the CTS concrete specimens. An example of this can be observed in Figure 4.1.2. However, no spalling was noted in the Luna PC specimens. Each of the Luna specimens deformed and cracked, but the specimens remained relatively intact after failure due to the adhesion of the resin, as can be seen in Figure 4.1.3.

The compression test results for the 3" cylinders are summarized in Table 4.1.2. The table is organized by the concrete mix tested. The age of the concrete when the specimens were tested was recorded. The recorded compressive strength was rounded to the nearest 10 psi. The average and standard deviation for each of the mixes was calculated and recorded. The average compressive strength was displayed graphically in Figure 4.1.7 for specimens that had cured for at least 1 day.

Table 4.1.2: Compressive Strength Results for 3" Cylinders

Concrete Mix	Age of Concrete	Specimen Identifier	Ultimate Load, P (lbs)	Compressive Strength, f_m (psi)	Average Compressive Strength (psi)	Standard Deviation (psi)
CTS Concrete	1-day	1	32376	4580	4680	190
		2	34688	4910		
		3	31230	4420		
		4	34077	4820		
		5	32944	4660		
CTS Concrete	7-day	A	32137	4550	4880	390
		B	37544	5310		
		C	33854	4790		
Luna PC Phase I: 17 wt.% Resin w/ SAP 1	1-day	1	88630	12540	12160	540
		2	83276	11780		
Luna PC Phase II: 10 wt.% Resin w/ #78 Dolomite	>7-day	1	59772	8460	8630	1080
		2	69165	9780		
		3	54024	7640		
Luna PC Phase II: 10 wt.% Resin w/ #68 Dolomite	>7-day	1	63208	8940	10010	970
		2	72445	10250		
		3	76549	10830		
Luna PC Phase II: 12 wt.% Resin	>7-day	1	89089	12600	11320	1120
		2	74503	10540		
		3	76549	10830		
Luna PC Phase II: 15 wt.% Resin	>7-day	1	87770	12420	11470	1880
		2	89727	12690		
		3	65730	9300		
Luna PC Phase II: 17 wt.% Resin w/ SAP 3	1-day	1	77910	11020	11240	330
		2	78280	11070		
		3	82126	11620		
Luna PC Phase II: 17 wt.% Resin w/ SAP 4	1-day	1	73235	10360	10310	230
		2	71115	10060		
		3	74295	10510		
Luna PC Phase II: 17 wt.% Resin w/ SAP 4	2-hour	1	57652	8160	8520	510
		2	58662	8300		
		3	64346	9100		

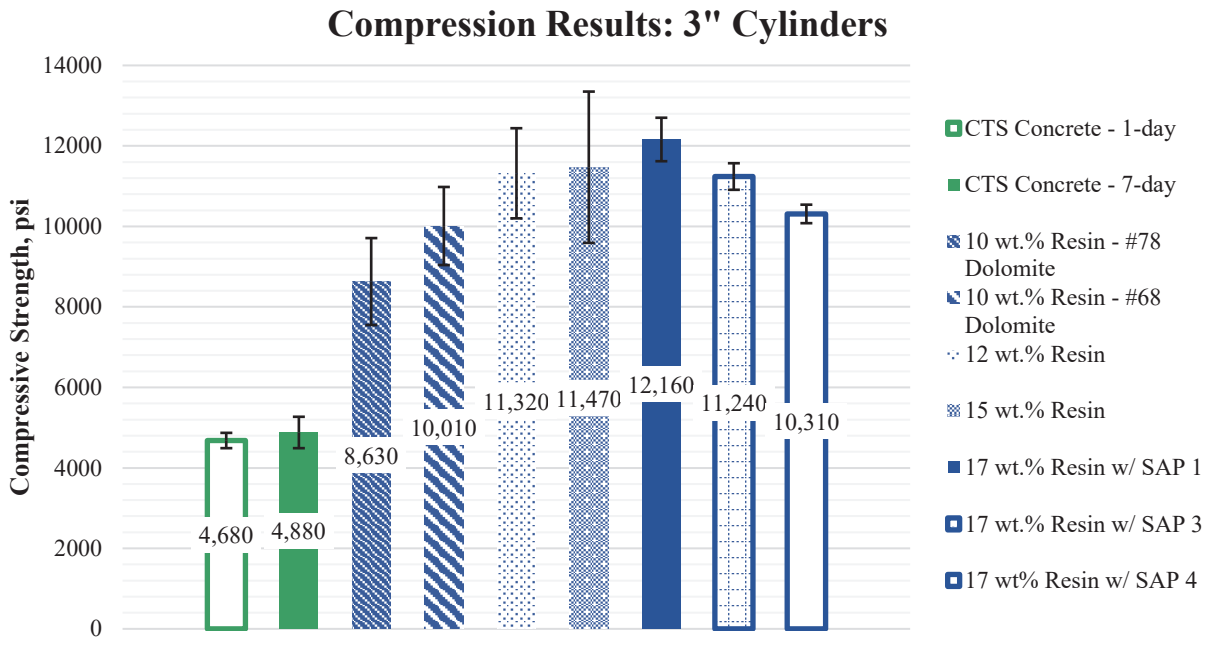

Figure 4.1.7: Compressive Strength Results for 3" Cylinders

Figure 4.1.8 shows the average compressive strength after 2-hours and 1-day of curing for the Phase II down-selected mix of 17 wt.% resin with SAP 4. The CTS concrete 1-day compressive strength was also plotted to compare the results.

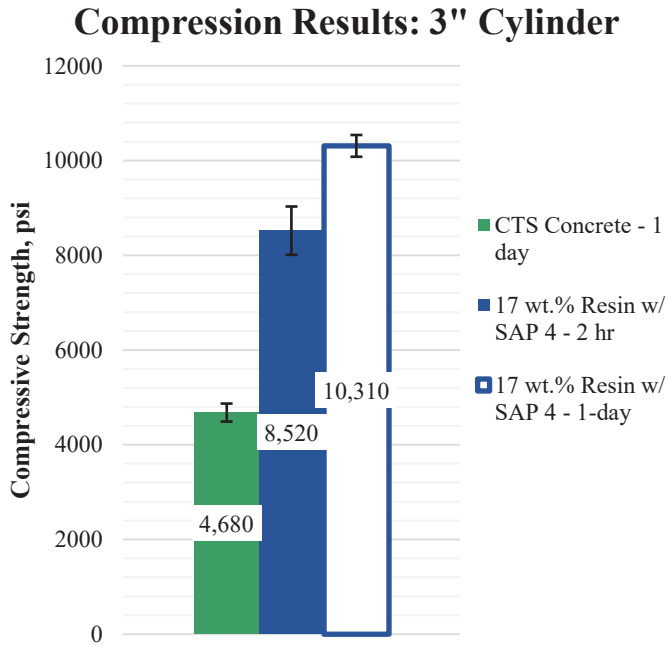

Figure 4.1.8: Compressive Strength of 3" Cylinders for Different Curing Times

Various cylindrical specimens of the Luna PC and CTS concrete were displayed in Figure 4.1.9 to display the visual differences between each cured mix. The 17 wt.% resin with SAP 4 Luna PC cylinders were shown in Figure 4.1.10.

Figure 4.1.9: 3" Cylinder Specimens of Various Concrete Mixes Prior to Testing

Figure 4.1.10: 3" Cylinder Specimens of the Down-Selected Luna PC Prior to Testing

4.1.3 Conclusions

For both sets of compression tests, the Luna PC formulations all outperformed the CTS concrete specimens. Observing the data from Figure 4.1.8, after only 2 hours of curing, the Luna PC down-selected mix had a strength more than twice that observed of the CTS concrete after 7-days of curing.

The strength calculated for the 2” cube specimens was found to be higher than the 3” cylindrical specimens because of both the platen restraint effects and the smaller size of the specimens [57]. Because of these effects, 2” cubes routinely give higher compressive results than cylinders. As a result, the Tri-Service Pavements Working Group (TSPWG) Manual, which was used as the guidelines in developing the PC, explicitly forbids the use of 2” cubes for compressive strength measurements [58]. For both these reasons, the cylindrical specimens were used to test all formulations created after Phase I to record a more accurate uniaxial compressive strength.

Comparing the Luna PC mixes, an increase in the compressive strength was observed as the resin content of the mix increased. However, the increase of strength begins to diminish as the resin wt.% is increased past 12 wt.%. The average compressive strength increased by only 7.4% between 12 wt.% and 17 wt.% resin, whereas the average increased by 31.2% from 10 wt. % to 12 wt.% resin. These diminishing returns on strength show that a resin wt.% range of 12 to 17% is the most desirable to achieve the preferred strength while minimizing the amount of resin. Thereby minimizing additional costs of the mix.

Observing the effects of the CA used, the larger maximum diameter stone, #68 stone, produced specimens with higher compressive strength. While this may be due to the aggregate, this is most likely a result of poor consolidation of the concrete cylinders from the low resin wt. % making the concrete unworkable. The poor consolidation produced very inconsistent data, which

can be observed by their high standard deviations. To verify that a larger maximum diameter CA will increase the compressive strength, more tests should be performed with more workable resin wt.%.

The addition of the SAPs influenced the observed compressive strength. The inclusion of SAP 3 in the PC decreased the average compressive strength by 7.6% compared to the Phase I Luna PC mix with SAP 1. The current down-selected mix of 17 wt.% resin with SAP 4 also had a decrease in strength of 15.2% compared to the Phase I mix. The decrease in strength was due to both Phase II mixes having higher silica content relative to the Phase I mix. However, the decrease of strength is outweighed by the beneficial thickening effects of the SAP as they prevent separation of the resin and improve the overall workability of the concrete. The PC down selections also maintained a higher compressive strength than that of the CTS concrete despite the overall strength reduction compared to Phase I.

Observing the effects of curing time, the average compressive strength of the down-selected mix increased by 21.0% from 2-hours of curing to 1-day of curing, as can be seen in Figure 4.1.8.

4.2 Flexural Strength

The flexural strength of the CTS concrete and the Luna PC in Phase I and the down-selected mix in Phase II were tested to determine the repair materials' strength in bending. When subjected to bending, a tension force is observed on the member, which for concrete, is significantly lower than the compressive strength. The direct tensile strength is approximately 10% of the compressive strength and is what controls the flexural strength. Concrete flexural strength ranges from 11% to 23% of the compressive strength [59]. The flexural tests recorded the modulus of rupture for the repair materials, and their results were compared and discussed.

4.2.1 Test Method and Procedure

To test the flexural strength of the repair materials, the procedures as defined by ASTM C293 [60] and ASTM C78 [61] were followed. Three (3) 3”x3”x12” beams were cast using steel molds of both the CTS concrete and the Phase I formulation of the Luna PC.

When following ASTM C293, the beams were loaded using center-point loading and were tested at a constant rate until failure. The loading rate is calculated by Equation 3 from the ASTM standard:

$$r = \frac{2Sbd^2}{3L} \tag{3}$$

where r is the loading rate in lbf/min, S is the rate of increase in stress on the tension face in psi/min, b is the width in inches, d is the depth in inches, and L is the span length of the beam in inches. Using a rate of stress increase of 175 psi/min, the loading rate was calculated to be 350 lbf/min and was used for each specimen.

The peak load applied to each specimen was then recorded and used to calculate the modulus of rupture for the material as determined using Equation 4:

$$R = \frac{3PL}{2bd^2} \tag{4}$$

where R is the modulus of rupture in psi, P is the ultimate applied load in lbf, L is the span length in inches, b is the width in inches, and d is the depth in inches of the specimen.

When following ASTM C78, the beams were loaded using third-point loading and were tested at a constant rate until failure. The loading rate is calculated by Equation 5 from the ASTM standard:

$$r = \frac{Sbd^2}{L} \tag{5}$$

where r is the loading rate in lbf/min, S is the rate of increase in stress on the tension face in psi/min, b is the width in inches, d is the depth in inches, and L is the span length of the beam in inches. Using a rate of stress increase of 125 psi/min, the loading rate was calculated to be 375 lbf/min and was used for each specimen.

The peak load applied to each specimen was then recorded and used to calculate the modulus of rupture for the material as determined using Equation 6:

$$R = \frac{PL}{bd^2} \tag{6}$$

where R is the modulus of rupture, P is the ultimate applied load, L is the span length, b is the width, and d is the depth of the specimen.

In Phase I, the modulus or rupture for both the CTS concrete and Luna PC was tested and calculated using ASTM C293. These specimens were tested in the Norris Laboratory at Virginia Tech and were tested at 5-day strength. Figure 4.2.1 shows a Luna PC specimen in the testing apparatus, and Figure 4.2.2 shows both the CTS concrete and Luna PC specimens after failure.

Figure 4.2.1: Luna PC Phase I Specimen in Testing Apparatus for Center-Point Loading

Figure 4.2.2: CTS Concrete (top) and Luna PC Phase I (bottom) Specimens after Failure in Flexure

In Phase II, the down-selected Luna PC was tested at 2-hours and 1-day of curing following the procedures of ASTM C78. The change in test method was to meet the requirement of the U.S. Air Force and to follow their preferred procedures. Figure 4.2.3 shows a test specimen for the down-selected mix loaded in testing apparatus for third-point loading.

Figure 4.2.3: Luna PC Specimen in Testing Apparatus for Third-Point Loading

4.2.2 Results and Observations

A summary of the flexural tests performed in Phase I is tabulated in Table 4.2.1 and shown graphically in Figure 4.2.4. The modulus of rupture was recorded to the nearest 5 psi. The average modulus of rupture and standard deviation for each material was also calculated and recorded.

Table 4.2.1: Center-point Loading Flexure Strength Results

Concrete Mix	Specimen Identifier	Span Length, L (in)	Avg. Width, b (in)	Avg. Depth, d (in)	Ultimate Load, P (lbs)	Modulus of Rupture, R (psi)	Average (psi)	Standard Deviation (psi)
CTS Concrete	1	9	3	3	1634.3	815	765	45
	2	9	3	3	1448.2	725		
	3	9	3	3	1511.9	755		
Luna PC Phase I: 17 wt.% Resin w/ SAP 1	1	9	3	3	7993.6	3995	3780	225
	2	9	3	3	7087.8	3545		
	3	9	3	3	7609.1	3805		

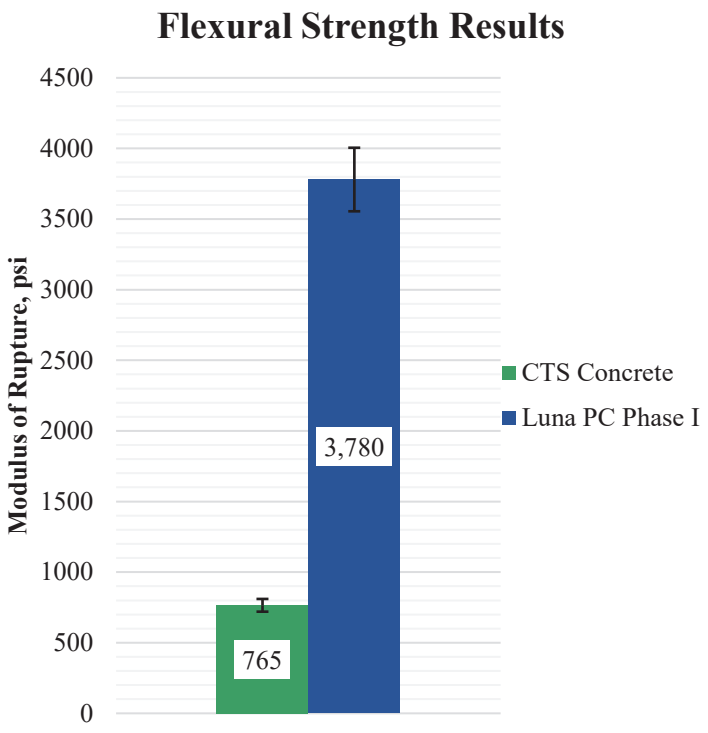

Figure 4.2.4: Center-point Loading Flexure Strength Results

The flexural strength results for the down-selected Luna PC mix is summarized in Table 4.2.2 and Figure 4.2.5. The age of the concrete was specified, and the modulus of rupture was recorded to the nearest 5 psi.

Table 4.2.2: Third-Point Loading Flexure Strength Results

Concrete Mix	Age of Concrete	Specimen Identifier	Span Length, L (in)	Avg. Width, b (in)	Avg. Depth, d (in)	Ultimate Load, P (lbs)	Modulus of Rupture, R (psi)	Average (psi)	Standard Deviation (psi)
Luna PC Phase II: 17 wt.% Resin w/ SAP 4	**2-hour**	1	9	3	3	6747.0	2250	2830	560
		2	9	3	3	8590.0	2865		
		3	9	3	3	10109.0	3370		
Luna PC Phase II: 17 wt.% Resin w/ SAP 4	**1-day**	1	9	3	3	9983.0	3330	3075	260
		2	9	3	3	9241.9	3080		
		3	9	3	3	8432.9	2810		

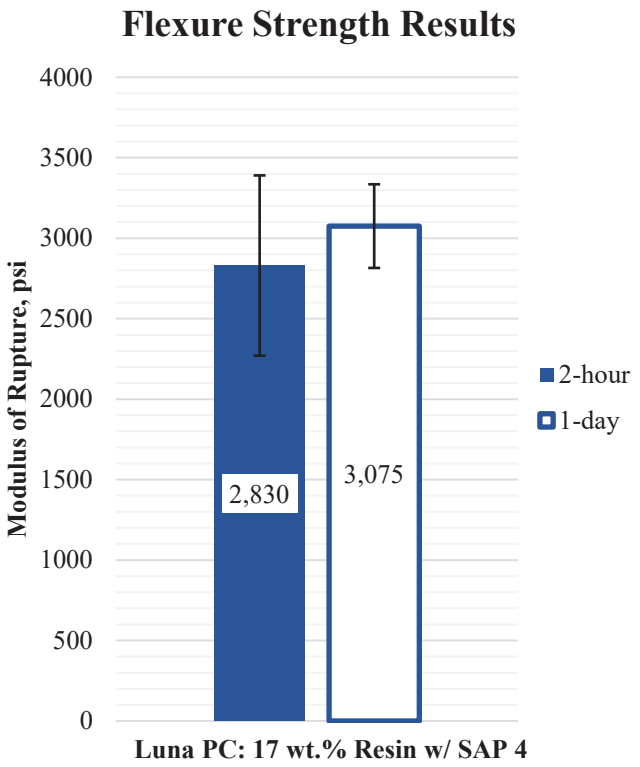

Figure 4.2.5: Third-Point Loading Flexure Strength Results

4.2.3 Conclusions

In Phase I, the Luna PC had a modulus of rupture nearly 4 times higher than that of the CTS concrete at 5-day strength (394%). At failure, due to its higher strength, the PC had a more explosive break than the CTS concrete. This is due to the brittle nature of the resin binder at room temperature after curing, and in general, concrete with higher compressive strength tends to be more brittle [59]. The CTS concrete remained slightly intact at the compression face of the specimen after failure, as observed in Figure 4.2.2.

The down-selected Luna PC mix only had a small increase in flexural strength from 2 hours to 1 day of curing. After curing for 1 day, the PC has a modulus of rupture increase 8.7%. Due to the long duration of the tests that came before it, specimen 3 of the 2-hour samples was

tested after approximately 3 hours of curing. This extra hour of curing most likely increased its actual modulus of rupture at 2 hours and contributed to the skew of the data.

4.3 Bond Strength

4.3.1 Test Method and Procedure

To test the bond shear strength of the repair materials, ASTM C882 was performed on various specimens in both Phases I and II. ASTM C882 is the test method for measuring the bond strength of epoxy-resin systems by testing cylindrical specimens in slant shear [62].

Using the typical concrete mix, 3” cylinders were cast and cured for a minimum of 7 days. After curing, the cylinders were cut using a tile saw at a 30-degree angle along their length, shown in Figure 4.3.1. These half cylinders were then placed back inside the 3” molds, where afterwards the repair material was then cast cured onto the cut cylinders. Figure 4.3.2 shows capped 3” slant shear specimens for the CTS concrete and Luna PC prior to testing.

Figure 4.3.1: Half-Cut Typical Concrete Cylinders

Figure 4.3.2: 3" Slant Shear Specimens Prior to Testing (Left: CTS) (Right: Luna PC)

The specimens were then tested in compression in accordance with ASTM C39. The incline, or slant, causes the bond of the repair material and the concrete to experience a shearing stress along the bond cross-section. Because this bond is typically weaker than the compression strength of the individual materials during loading, the bond strength can be determined from the maximum applied load using Equation 7:

$$\tau = \frac{P}{0.7854ab} \tag{7}$$

where τ is the bond strength in psi, P is the ultimate applied load in lbf, and the denominator is the area of an ellipse, where a and b are the lengths of the two major axes recorded in inches. For a typical 3" cylinder cut at a 30° incline, a is equal to 3 inches, b is equal to 6 inches, and the elliptical bonding surface area is equal to 14.13 in^2.

4.3.2 Results and Observations

Each of the specimens were tested at a strength of 1 day. The results are summarized in Table 4.3.1, with the bond strength recorded to the nearest 10 psi. The average and standard deviation are given for each repair material. These values are displayed graphically in Figure 4.3.3.

Table 4.3.1: Bond Strength Slant Shear Test Results

Concrete Mix	Specimen Identifier	Ultimate Load, P (lbs)	Bond Strength, τ (psi)	Average Bond Strength (psi)	Standard Deviation (psi)
CTS Concrete	1	19069	1349	1260	320
	2	20026	1417		
	3	18098	1280		
	4	10028	709		
	5	21504	1521		
Luna PC Phase I: 17 wt.% Resin w/ SAP 1	1	21151	1500	1640	200
	2	25152	1780		
Luna PC Phase II: 17 wt.% Resin w/ SAP 4	1	26845	1900	1450	390
	2	17574	1240		
	3	16928	1200		

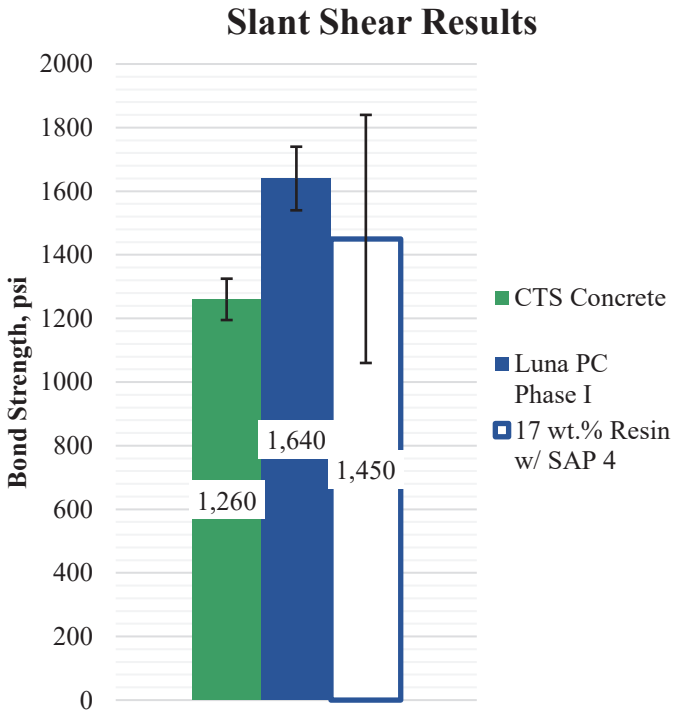

Figure 4.3.3: Bond Strength Slant Shear Test Results

For both repair material specimens, failure occurred cleanly along the bond surface. No other defects, such as spalling, were noticed for any of the half-cylinder samples. Pictures of the CTS concrete and Luna PC test specimens after failure can be found in Figures 4.3.4 and 4.3.5, respectively.

Figure 4.3.4: CTS Concrete Slant Shear Specimen After Failure

Figure 4.3.5: Luna PC Slant Shear Specimen After Failure

4.3.3 Conclusions

Phases I and II of the Luna PC down-selections had a higher average bond strength than the CTS concrete. A large variability was observed for the Phase II down-selection. More tests would need to be performed to determine whether Specimen 1 of that mix was an outlier.

4.4 Vertical Bond Strength

Because runways do not experience direct shear or direct tension, further tests were developed to determine the bond strengths for the repair materials in flexural scenarios. In the application of military aircraft passing over the patch and runway, the slab will experience bending due to applied load from the aircraft and the ground supporting the slab. It is critical that the repair material does not delaminate from the existing runway from this loading.

This section describes the test procedures and results for the bond strength applied vertically in flexure. These tests attempt to simulate the vertical edges and boundaries of the patch

and determines their effective strength. This effective strength was quantified through the composite beam's modulus of rupture. These tests were only performed in Phase I of developing the Luna PC.

4.4.1 Test Method and Procedure

A modified version of ASTM C78 was performed on 3"x3"x12" beam specimens. These specimens comprised two (2) 3"x3"x6" halves split vertically. The first half was made of the typical runway concrete and the other half was made of the repair patching material.

To form the specimens, multiple standard 3"x3"x12" beams were cast using the typical concrete mix. The mix and casting procedures followed the same outline as noted in Section 3. After seven (7) days of curing, the beam specimens were cut vertically into two (2) equal 6-inch-long halves using a wet tile saw. The half-beams were then stored in the curing room for later use.

On the day of casting the repair material, the beam molds were prepared by placing the typical concrete half-beams on one side of the mold with the roughened end facing up. Proper care was taken with the releasing agent for the Luna PC specimens to ensure none was applied to the exposed concrete side. Figure 4.4.1 shows the molds prepared with the typical concrete half beams prior to the casting of the repair materials. The patching material was then poured on the open half and cured, so a bond could form on the center cross-section of the beam. The demolded Luna PC specimens for vertical adhesion tests are shown in Figure 4.4.2.

Figure 4.4.1: Typical Concrete Half Beams in Molds Prior to Casting of Repair Materials

Figure 4.4.2: Cured and Demolded Luna PC Vertical Adhesion Specimens

After the patching material had cured for a minimum of 7 days, the beams were tested in third-point loading. The beams were loaded using the same apparatus and loading rate calculated using Equation 5 for flexural strength of 375 lbf/min and were tested until failure. The modulus of rupture was calculated and recorded for each beam using Equation 6.

Figures 4.4.3 and 4.4.4 show the CTS concrete and Luna PC specimens, respectively, placed inside the test apparatus before and after failure. Both specimens were oriented so the typical concrete half is resting on the right support.

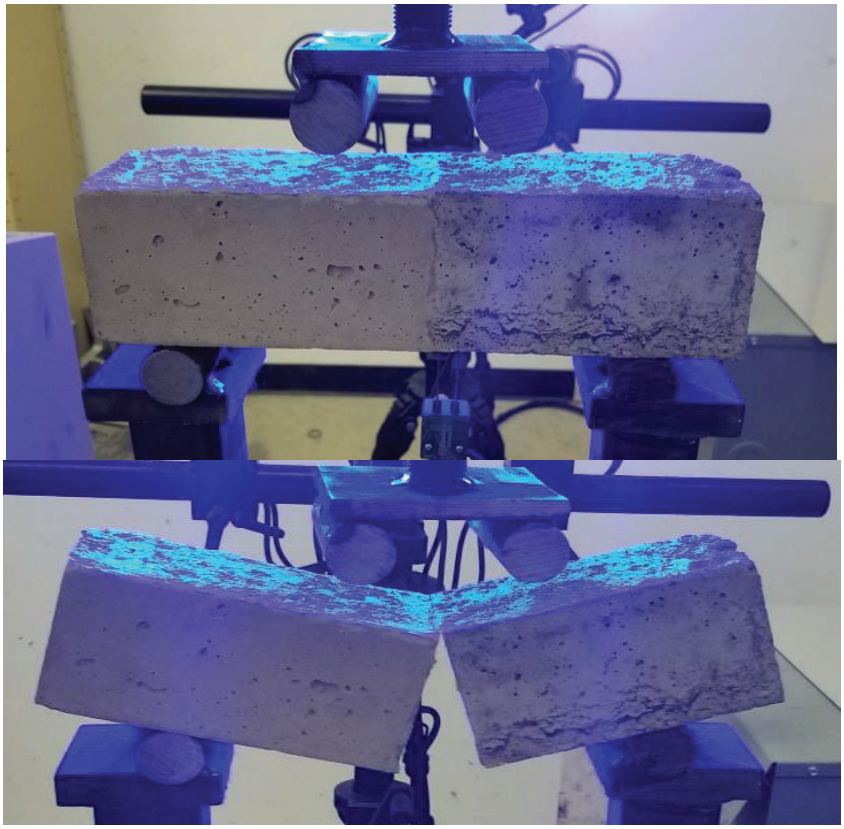

Figure 4.4.3: CTS Concrete in Vertical Adhesion Before (Top) and After (Bottom) Loading

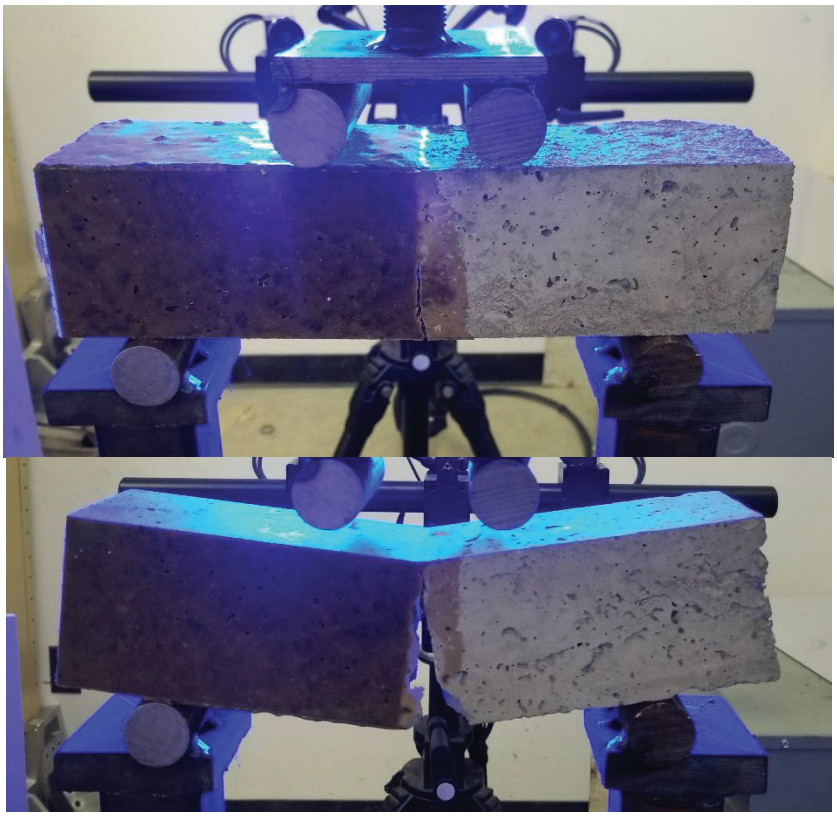

Figure 4.4.4: Luna PC in Vertical Adhesion Before (Top) and After (Bottom) Loading

4.4.2 Results and Observations

The results from the vertical adhesion tests were summarized in Table 4.4.1. For both concrete mixes, the beam dimensions and ultimate load were recorded. The modulus of rupture was then calculated and recorded to the nearest 5 psi. The average and standard deviation was listed for each mix type and displayed graphically in Figure 4.4.5.

Table 4.4.1: Vertical Bond Strength Results

Concrete Mix	Specimen Identifier	Span Length, L (in)	Avg. Width, b (in)	Avg. Depth, d (in)	Ultimate Load, P (lbs)	Modulus of Rupture, R (psi)	Average (psi)	Standard Deviation (psi)
CTS Concrete	1	9	3	3	927.1	310	285	65
	2	9	3	3	1086.4	360		
	3	9	3	3	656.2	220		
	4	9	3	3	739.2	245		
Luna PC Phase I: 17 wt.% Resin w/ SAP 1	1	9	3	3	1090.4	365	490	100
	2	9	3	3	1422.7	475		
	3	9	3	3	1554.6	520		
	4	9	3	3	1814.0	605		

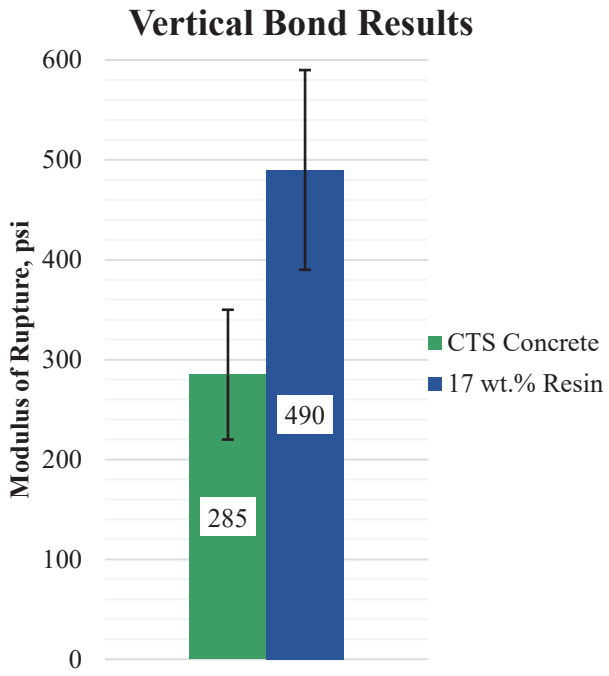

Figure 4.4.5: Vertical Bond Strength Results

Specimens 1 and 3 of the CTS Concrete beams had a recorded length of 11.5 inches, while every other specimen had a length of 12 inches. The span length for each specimen was 9 inches, so it is likely that the shortened lengths did not impact the results. For each of the CTS concrete specimens, failure occurred cleanly through the bond plane. Each failure was brittle and rapid with no signs of failure for either half-beam, only along the bond plane.

All specimens of the Phase I Luna PC experienced brittle failures. Specimens 1 and 3 had clean breaks along the bond, similar to the CTS specimens. Specimens 2 and 4, however, saw failure propagate through the typical concrete half-beam adjacent to the bond plane. This can be observed for Specimen 2 in Figure 4.4.4.

4.4.3 Conclusions

The Luna PC vastly outperformed the CTS concrete specimens by having an average modulus of rupture nearly double the CTS concrete or a 71.9% increase of strength. There is much variability

from these tests, as evident by the large standard deviations. However, even with such variability, the weakest Luna PC specimens still outperformed the strongest specimens of the CTS concrete. In addition to the strength results, the two specimens that did not fail along the bond suggest that the bond strength may be higher than the strength of the typical concrete alone, further indicating the PC is a good repair material with high bond strength.

4.5 Horizontal Bond Strength

In addition to vertical bond strength being a critical consideration of the repair materials, the horizontal bond strength was also simulated and determined. The majority of repairs of runways are not the full depth of the slab, but rather only partial depth repairs that are wider spread in surface area. The horizontal bond strength of the repair material prevents the delamination between this base layer of existing runway concrete and the repair material.

The bond of the repair material resists the shearing stress of the applied load through the slab as it bends in the transverse direction. This bond ensures that the composite slab acts cohesively and does not experience sliding along the horizontal plane of the bond. Figure 4.5.1 is an example of these effects from a transversely loaded cantilever beam made of multiple layers, and how, when bonded, the boards deflect and elongate at a collective unit.

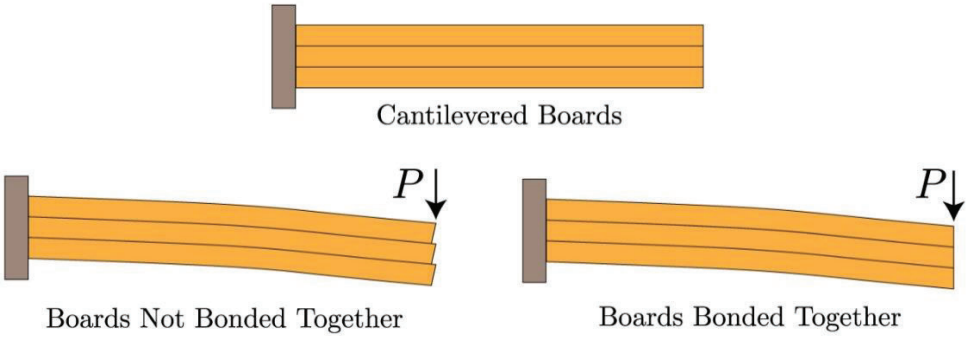

Figure 4.5.1: Effects of Horizontal Bonding for Members Subjected to Transverse Loads [63]

This section describes the test procedures and results for the horizontal bond strength of the repair materials when subjected to flexure. These tests attempt to simulate the base of the patch to the top face of the exposed concrete and determines their effective strength. This effective strength was quantified through the composite beam's modulus of rupture. These tests were performed only in Phase I of developing the Luna PC.

4.5.1 Test Method and Procedure

A modified version of ASTM C293 was performed on 3"x3"x12" beam specimens. These specimens were comprised of two (2) unequal depths of different concrete materials. The top 2 inches of the beam was made of the typical runway concrete, where the remaining 1 inch of depth was comprised of the patching material.

To form the specimens, 3"x3"x12" beam molds were used to cast the typical concrete mix to the desired 2" of depth. The mix and casting procedures followed the same outline as noted in Section 3. After one (1) day of curing, the partial specimens were demolded and stored in the curing room until seven (7) days of curing had occurred, minimum.

On the day of casting the repair material, the beam molds were prepared by placing the typical concrete partial-beams inside the mold allowing for the 1" of patching material to be cast on top, as shown in Figure 4.5.2. Proper care was taken with the releasing agent so that none of it was applied to the exposed concrete. The patching material was then poured onto the concrete and then cured. This casting method allowed the patching material to bond to a horizontal plane along the beam. Once cured, the beams were demolded. A picture of the Luna PC specimens once cured and demolded can be found in Figure 4.5.3.

Figure 4.5.2: Typical Concrete Partial Beams in Molds Prior to Casting of Repair Materials

Figure 4.5.3: Cured and Demolded Luna PC Horizontal Adhesion Specimens

After the patching material had cured for a minimum of 7 days, the beams were tested using center-point loading. The beams were loaded using the same apparatus and loading rate

calculated using Equation 3 for flexural strength of 350 lbf/min and were tested until failure. The modulus of rupture was calculated and recorded for each specimen using Equation 4.

4.5.2 Results and Observations

When configuring the testing apparatus, the Luna PC specimens were incorrectly loaded using a third-point bending load head. Due to time constraints, these specimens were not recast or retested. The ASTM C78 standard states that third-point bending generally produces values lower than center-point bending. Because of this, the modulus of rupture calculations was updated to match this loading method and kept.

The results from the horizontal adhesion tests were summarized in Table 4.5.1. For both concrete mixes, the beam dimensions and ultimate load were recorded. The modulus of rupture was then calculated and recorded to the nearest 5 psi. The average and standard deviation was listed for each mix type and displayed graphically in Figure 4.5.4.

Table 4.5.1: Horizontal Bond Strength Results

Concrete Mix	Specimen Identifier	Span Length, L (in)	Avg. Width, b (in)	Avg. Depth, d (in)	Ultimate Load, P (lbs)	Modulus of Rupture, R (psi)	Average (psi)	Standard Deviation (psi)
CTS Concrete	1	9	3	3	1419.6	710	735	70
	2	9	3	3	1363.7	680		
	3	9	3	3	1618.8	810		
Luna PC Phase I: 17 wt.% Resin w/ SAP 1	1	9	3	3	8476.0	2825	2825	295
	2	9	3	3	7590.0	2530		
	3	9	3	3	9337.6	3115		

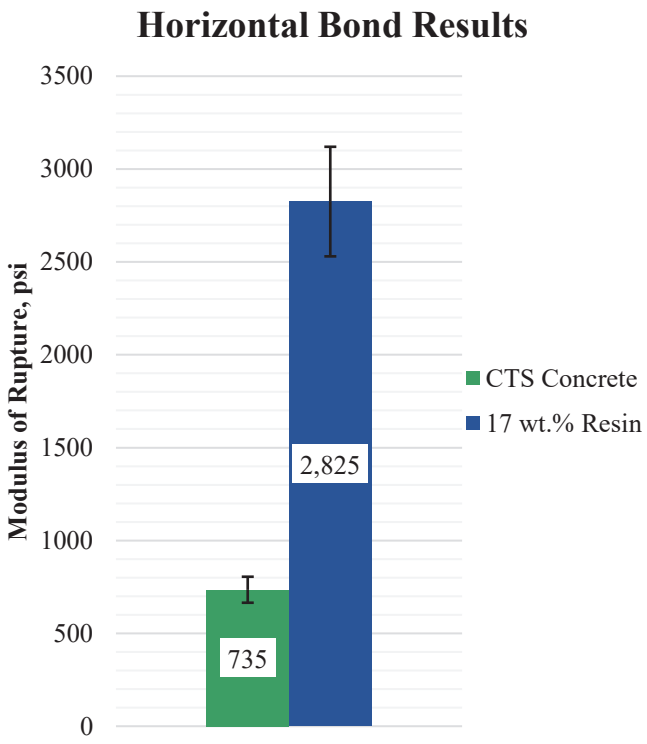

Figure 4.5.4: Horizontal Bond Strength Results

For each of the specimens, failure was very brittle and rapid. The Luna PC specimens were very explosive at failure with each shooting off the test apparatus as the crack quickly propagated through the member. Figure 4.5.5 shows a Luna PC specimen after failure. The CTS beams remained hinged at the tension face at failure, as can be seen in Figure 4.5.6.

Figure 4.5.5: Luna PC Specimen in Horizontal Adhesion after Failure

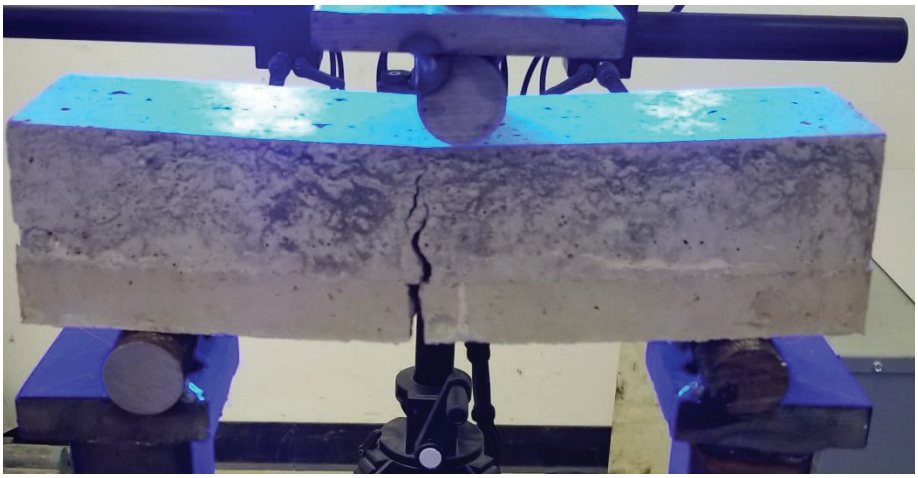

Figure 4.5.6: CTS Concrete Specimen in Horizontal Adhesion after Failure

Cracks began to form in the typical concrete prior to complete failure through the repair materials, which implies some local delamination at these areas. Specimen 2 of the Luna PC observed a shear failure from being loaded in third-point bending rather than center-point bending.

4.5.3 Conclusions

The Luna PC greatly outperformed the CTS concrete specimens. The PC modulus of rupture was determined to be 284% higher than the CTS concrete. When comparing these results to the full flexure results of the repair material alone in Phase I, the results appear similar. This suggests that for both repair materials, the horizontal bond was strong enough to transfer all tension loads to the repair material cross section and work compositely with the typical concrete.

4.6 Workability

In Phase II, the workability of the PC repair material was a critical design consideration. When used as a repair material, the mixes need to be flowable, mixable, and castable. The increased workability allows the repair of the runway to be rapid, easily poured, and compacted by hand, in the field. Various mixes of the PC were developed to determine how changing different factors

affect the mix workability. From these tests, if the workability of the mixes were found to be adequate, the formulations would then be down selected and used in further tests.

4.6.1 Test Method and Procedure

As workability is an empirical property, the test procedure of ASTM C143 was performed on each developed mix of the repair materials to better quantify which mixes were more workable. ASTM C143 is the test method for measuring the slump of hydraulic-cement concrete, where higher slumps indicate more workable mixes [64].

After the concrete was mixed until homogeneous, the concrete was then poured into the slump cone in three (3) flights of equal depth. Between each depth, the concrete was rodded, and hand tamped a minimum of 25 times. Once the slump cone was filled, the exposed surface was smoothed using a trowel. Afterwards, the slump cone was slowly lifted, and the concrete was allowed to slump and spread under its own self-weight. The slump was recorded by measuring the distance between the top of the slump cone and the apex of the slumped concrete.

When testing the workability, in addition to the measured slump, observations about the ease in mixing and the flowability of the concrete were noted. As an example, if the slump of the mix was relatively good, but the mix was very resistant/stiff when mixing or stuck to the sides of the mixing drum or bucket, this mix would be considered undesirable. The ideal mix design was to have high slump, flowability, compact ability, and mixability. The mix would also have low separation of the resin and aggregates.

For the different mixes of PC tested, the first round of testing kept the same mix proportions as Phase I, with only the type of CA used as the variable. Only the first test included SAP, so that it would have the same proportions as the mix design from Phase I. No SAP was used in subsequent

mixes due to lack of adequate supply. The second round of testing varied the CA used as well, while this time using a 10 wt.% resin mix instead of the 17 wt.% resin mix in Phase I. The third round of slump tests varied the weight percent of the resin, while keeping the rest of the mix design the same as Phase I. In the final round of slump tests, the proportions of silica packages were altered to determine their effects on the workability and slump. From these variations, a down selection of PC was chosen for all further tests.

4.6.2 Results and Observations

Table 4.6.1 summarized each of the concrete mixes that were tested for slump. The tests were organized by the date and order they were performed. The slump was recorded to the nearest 1/4 inch and data bars were used to better visualize which mixes had higher slumps. The final column of Table 4.6.1 recorded whether the concrete was easy to mix. While this is not included in the ASTM, this empirical factor was included to better choose between mixes that had similar slumps. Below the table is a legend for this column that explains what each “yes” and “no” option means in more detail. Detailed pictures of each slump test have been included in Appendix A.

No noticeable differences in slump were observed between the first eight (8) tests that varied the CA used. For the 17 wt.% resin mixes, each mix had similar, high recorded slump due to the relatively high resin wt.%. The smaller aggregates sizes were easier to work with, in general. For the 10 wt.% resin mixes, the PC mixtures appeared very “dry” and gravel-like. As a result, the mixes were generally unworkable and difficult to mix. A majority of their recorded slumps were from shear failures.

Table 4.6.1: Slump Test Results

Date	Concrete Type	Wt.% Resin	Coarse Aggregate	Fine Aggregate	Silica Additive Package	Recorded Slump (in)	Easy to Mix?
9/9/2020	Luna	17%	#78 Dolomite	Natural Sand	SAP 1	9.25	Yes
	Luna	17%	#68 Granite	Natural Sand	--	10	Yes
	Luna	17%	#57 Dolomite	Natural Sand	--	10.5	Yes
	Luna	17%	#68 Dolomite	Natural Sand	--	9.5	Yes*
9/11/2020	Luna	10%	#78 Dolomite	Natural Sand	--	8.25	No*
	Luna	10%	#68 Granite	Natural Sand	--	0	NO
	Luna	10%	#57 Dolomite	Natural Sand	--	3.5	NO
	Luna	10%	#68 Dolomite	Natural Sand	--	6.5	No*
9/14/2020	CTS Concrete	--	#78 Dolomite	Natural Sand	--	2.25	Yes*
9/16/2020	Luna	12%	#78 Dolomite	Natural Sand	--	4.5	Yes+
	Luna	15%	#78 Dolomite	Natural Sand	--	6.25	Yes
10/9/2020	Luna	15%	#78 Dolomite	Natural Sand	SAP 2	2	No
	Luna	17%	#78 Dolomite	Natural Sand	SAP 3	6.5	Yes
10/21/2020	Luna	17%	#78 Dolomite	Natural Sand	SAP 4	5.5	Yes
	Luna	17%	#78 Dolomite	Natural Sand	SAP 5	5	No
	Luna	17%	#78 Dolomite	Natural Sand	SAP 6	6	No

"Easy to Mix?" Legend:

Yes - Mixed well in a 5-gallon bucket, and was fairly flowable. Little sticking to the sides of the bucket was observed.

Yes* - Mixed fairly easily, but there was some resistance either from large aggregates or from the concrete sticking to the sides of the bucket.

No* - More difficult to mix compared to higher resin contents, but not as difficult to mix as the larger coarse aggregate mixes. This mix was much more gravel-like than a fluid concrete mix.

No - Difficult to mix in a 5-gallon bucket. There was much resitance against the mixing blade and concrete was packing against the sides and bottom, most likely from a denser packing of the concrete mix.

NO - Very unworkable. The larger aggregates were very resistant to the mixing blade, and much of the concrete stuck to the sides and bottom further causing mixing issues. This mix was very dry and gravel-like.

+ - Initial slump was recorded to be 0.5 inches, but after a very small amount of pressure was applied to the top of the cone, a shear failure was observed and that slump was recorded.

Increasing the resin wt.% appeared to increase the slump of the mixes. The 12 wt.% resin mix was still dry and generally unworkable but was slightly more workable than the 10 wt.% resin

mixes. The 15 wt.% resin had good slump and was relatively easy to mix. This mix retained the slump cone shape moreso than the 17 wt.% resin.

Noticeable separation of the resin and aggregates was observed for the PC mixes with any SAP. As the slump cone was being filled, the resin would seep out the bottom of the mold. These effects were drastically reduced with the addition of the silica packages due to its thickening effect. However, the mixes with SAP also saw a significant decrease in workability due to the increase in packing density. These mixes had slumps that more closely resembled typical cement-based concrete mixes in that the slump retained the cone shape rather than completely shearing or spreading out like a puddle.

The CTS concrete observed relatively low slump compared to the higher wt.% resin PC mixes and typical concrete. The CTS concrete was fairly easy to mix, since a drum mixer was used, and it was simple to compact into the slump cone when compared to the lower wt.% resin PC mixes.

4.6.3 Conclusions

Overall, different CA do not affect the overall desired slump. The mixability of the PC is decreased by larger aggregate sizes due to the resistance against the mixing blade. A higher wt.% resin is more desirable to achieve higher workability and flowability for the patching material. The higher wt.% resin prevents the concrete from appearing “dry” and allows for better consolidation when compacting into molds.

The addition of SAP is crucial to prevent separation of the resin from the aggregates, while the thickening effect does partially decrease the recorded slump. The addition of SAP is also beneficial to darken the color of the concrete as well as increase the packing density, thus allowing

the concrete to retain its shape for longer. Too much SAP, however, will lead to very unworkable mixes that become increasingly more difficult to mix.

The higher wt.% resin mixes outperformed the CTS concrete in slump and were easier to mix and compact by hand. The resin acted as a lubricant between the aggregates themselves and other objects such as the walls of the bucket and slump cone. This prevented the PC from adhering to the 5-gallon bucket and increased its flowability. The CTS concrete, on the other hand, was generally more unworkable due to its low w/c ratio, thus acting more solid when compacted into the slump cone.

The Luna PC mix design of 17 wt.% resin w/ #78 CA, SAP 4 was determined to be the best balance of each of the above described proportions. Its observed slump was relatively high and retained the slump cone shape, similar to typical cement-based concrete. The higher resin wt.% and smaller CA allowed it to be more flowable and mixable. The silica package, SAP 4, reduced the seeping and separation of the resin, as well as increased its packing density. As such, this mix was down-selected for further testing in Phase II.

4.7 Modulus of Elasticity

The Tri-Service Pavements Working Group (TSPWG) Manual from the Department of Defense describes repair materials that have elastic moduli greater than 1,000 ksi as rigid repair materials [58]. Rigid repair materials are designed to closely exhibit the properties of ordinary Portland cement concrete. Table 2-1 of the TSPWG Manual 3-270-01.08-2 further describes that the rigid repair material must have a modulus of elasticity greater than 2,000 psi after 2 hours of curing. To determine whether the Luna PC meets these criteria, the moduli of elasticity of the PC and CTS concrete were tested and compared.

4.7.1 Test Method and Procedure

The modulus of elasticity was determined following the procedures in accordance with ASTM C469 [65]. For each repair material tested, three (3) 4” diameter cylinders were cast and cured. A compressometer was then centered on the cylinder and screwed into place. The aluminum stabilizers were unscrewed from the compressometer after it was tightened onto the cylinder and prior to testing. The specimens were capped using 4” diameter rubber caps and placed in the testing apparatus as shown in Figure 4.7.1. The gage length of the compressometer was recorded to be 5.5 inches.

Figure 4.7.1: Modulus of Elasticity Specimen in Testing Apparatus with Compressometer

To gather more precise data than what is described in the ASTM standard, the cylinders were loaded in increments of 5000 lbf and the measured displacement of the compressometer was

recorded. Each cylinder was loaded three (3) times with only the second and third loadings being recorded. The specimen was first loaded without recorded measurements to ensure proper readings of the compressometer and that the cylinder and caps were settled.

To prevent the cylinders from experiencing inelastic deformations, the specimens were loaded to a maximum of 40% of their ultimate compressive strength. For the Luna PC specimens, the cylinders were loaded to a maximum of 30 kips, approximately 20% of ultimate strength, except for the first specimen tested. This was due to the observation of inelastic deformations in the cylinder despite being within the assumed elastic region. Subsequent tests appeared very linear with no noted inelastic deformations.

When calculating the modulus of elasticity for each specimen, the applied loads were then converted to compressive stresses using Equation 1 for 4" diameter cylinders. The strain of the cylinder was calculated using Equation 8:

$$\varepsilon = \frac{dL}{2L} \tag{8}$$

where ε is the recorded strain in inches per inches (in/in), dL is the measured displacement of the compressometer in inches, and L is the gage length of the compressometer, also in inches. The recorded displacements were halved due to the geometry of the compressometer used and considering the rotation of the pivot point of the compressometer [66].

The applied stresses and recorded strains were then plotted against each other and a linear trendline was fit to the data for each cylinder. The y-intercept was set to the origin, as it is assumed there is no initial stress in the member. The slope of the trendline was recorded as the modulus of elasticity of the specimen.

4.7.2 Results and Observations

The results of the modulus of elasticity tests were summarized in Table 4.7.1. For each repair material tested, the age of concrete was recorded, and the modulus of elasticity was calculated and recorded to the nearest 50 ksi. The average and standard deviation of each mix was calculated and plotted in Figure 4.7.2. All plots of the stress-strain curves can be found in Appendix B.

Table 4.7.1: Modulus of Elasticity Results

Concrete Mix	Age of Concrete	Specimen Identifier	Modulus of Elasticity, E (ksi)	Average (ksi)	Standard Deviation (ksi)
CTS Concrete	**>3-day**	1	3800	4050	600
		2	4750		
		3	3600		
Luna PC Phase II: 15 wt.% Resin	**>3-day**	1	3600	3900	300
		2	4150		
		3	3900		
Luna PC Phase II: 17 wt.% Resin	**>3-day**	1	3200	3450	200
		2	3550		
		3	3550		
Luna PC Phase II: 17 wt.% Resin w/ SAP 3	**3-day**	1	3400	3350	650
		2	2700		
		3	4000		
Luna PC Phase II: 17 wt.% Resin w/ SAP 4	**2-hour**	1	2750	2750	50
		2	2750		
		3	2700		

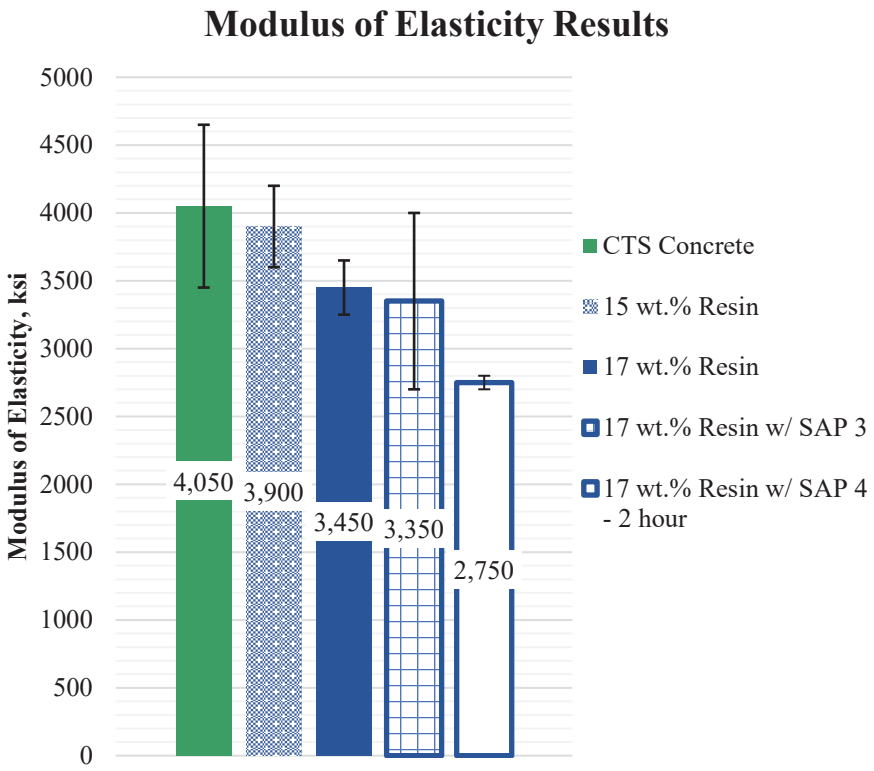

Figure 4.7.2: Modulus of Elasticity Results

Analysis was performed on the samples with greater than 3-day strength using t-tests to determine the statistical significance of the Luna PC modulus averages compared to the CTS concrete. Table 4.7.2 displays the results of the t-tests for each Luna PC formulation and their significance level of assuming the concrete mixes are unequal.

Table 4.7.2:* t-*Test Results Comparing the Modulus of Luna PC vs. CTS Concrete

Concrete Mix	Probability
Luna PC Phase II: 15 wt.% Resin	**69.9%**
Luna PC Phase II: 17 wt.% Resin	**21.8%**
Luna PC Phase II: 17 wt.% Resin w/ SAP 3	**25.7%**

Using a 95% confidence interval, the above results show the average modulus for each Luna PC formulation, while lower than the CTS concrete, are not statistically significant. Factoring in the scatter of the data, the Luna PC and CTS concrete moduli of elasticity can have the same value.

4.7.3 Conclusions

Each repair material met the TSPWG Manual requirement for a minimum modulus of elasticity of 2,000 ksi. The CTS concrete had a much higher modulus than any of the Luna PC mix designs. This is most likely due to the resin having a lower modulus than a cement paste. The addition of more resin wt.% tends to decrease the modulus. Because the aggregates are the stiffer ingredient of the PC, reducing the percentage of aggregates will reduce the weighted stiffness from the resin and aggregates.

Due to the limited number of trials, it is not possible to determine the effects of the SAP appropriately, while it appears the SAP does not impact the modulus due to its low concentration in the mix as a whole. The down-selected Phase II Luna PC mix had precise test results, as evident by its low standard deviation. Further tests should be performed on the same mix after longer curing times to determine the increase in modulus.

Due to the Luna PC cylinders entering plastic deformation sooner than anticipated given their high compressive strengths, it is likely that the PC experiences viscoelastic behavior in its stress-strain diagram. Further tests should be performed to determine an accurate stress-strain curve and whether the PC does exhibit this viscoelastic property. These tests are outside the scope of this thesis.

4.8 Coefficient of Thermal Expansion

The repair materials, after being cast, will experience a wide range of temperatures through their extended use. Over time and through these temperature ranges, the patching materials will undergo expansion and contraction. These cycles could potentially cause damage to the existing runway concrete and the bond between it and the patch. To assess these potential issues, the coefficient of thermal expansion (CTE) was determined for each repair material. Higher CTE values suggest that the concrete will experience larger increases and decreases in volume as the temperatures fluctuate. The TSPWG Manual 3-270-01.08-2 requires that rigid repair materials have a measured CTE less than or equal to 7 x 10^{-6} in/in/°F [58].

4.8.1 Test Method and Procedure

The CTE of the repair materials were tested using the procedures described in ASTM C531 [67]. Three 3”x3”x12” bar specimens were prepared for each repair material. Prior to casting, the molds were prepared with 3”x3”x1/2" steel plates, with a centered 1/4” diameter threaded hole on each end of the mold. Quarter-inch gage studs were then screwed into the plates to then be cast with the concrete bars so the length of the bars can be measured using a length comparator. After casting, the bars were then cured and demolded, as described in Section 3. Figure 4.8.1 shows several CTE specimens with the gage studs placed in an oven.

Figure 4.8.1: CTE Specimens with Gage Studs (Left: CTS) (Right: Luna PC)

To accurately measure the CTE and to ensure its linearity, multiple measurements were taken at various temperature ranges. The measurements were taken at approximately 0°F, 74°F, 150°F, and 225°F (±4°F for each). The specimens were cooled using an industrial freezer and heated using an oven, each for 24 hours.

At each of the above temperature ranges, the lengths of the beams were measured using the length comparator with a digital indicator. The length of the steel rod was recorded, then used to tare the digital indicator, as shown in Figure 4.8.2. Each specimen was placed into the comparator by resting the studs into the seats, as shown in Figure 4.8.3. The change in length of the comparator was recorded and added to the length of the steel rod. This measurement was recorded as the length of the specimen. The temperature of the bar was measured using a handheld infrared thermometer and the average of the bar was recorded. The length of one stud was recorded at 0°F as 0.809 inches.

Figure 4.8.2: Length Comparator Zeroed with Steel Rod

Figure 4.8.3: Luna PC CTE Specimen Loaded in Length Comparator

The CTE of each specimen was recorded by plotting the measured strains by their respective recorded temperatures. The strain at each temperature was calculated using Equation 9:

$$\varepsilon = \frac{Z - kX(T_2 - T_1) - W}{W - X} \tag{9}$$

where ε is the strain due to the elevated temperature, T_2, recorded in inches per inches (in/in), Z is the length, in inches, of the bar at T_2, k is the linear coefficient of thermal expansion per °F of the gage studs, X is the length of two studs at the lower temperature, T_1, and W is the length of the bar at the lower temperature, T_1, recorded in inches. Both temperatures T_1 and T_2 were measured in degree Fahrenheit (°F). For all calculations, k and X were assumed to be 7.2×10^{-6} in/in/°F and 1.618 inches, respectively.

For each strain calculation of every bar, the measurements recorded at the freezing temperatures (0 ±4°F) was used as the low temperature readings. Since the data is relative, the freezing temperature values were used as a reference, so that no strains were recorded as negative. After the strains were calculated for each specimen, the strains and temperatures were plotted against each other and a linear trendline was fit through the data. The slope of this trendline was recorded as the specimen's CTE in in/in/°F.

4.8.2 Results and Observations

The raw data from the tests results can be found in Appendix C. For each concrete mix, the specimen identifier, temperature, and length of the bar at that temperature were recorded. The strain was then calculated using Equation 9 with the freezing temperatures as the low temperatures to normalize the data. The recorded strains in milli-strain (mε) were plotted against the temperatures in °F and a linear trendline was fit for each mix in Figure 4.8.4.

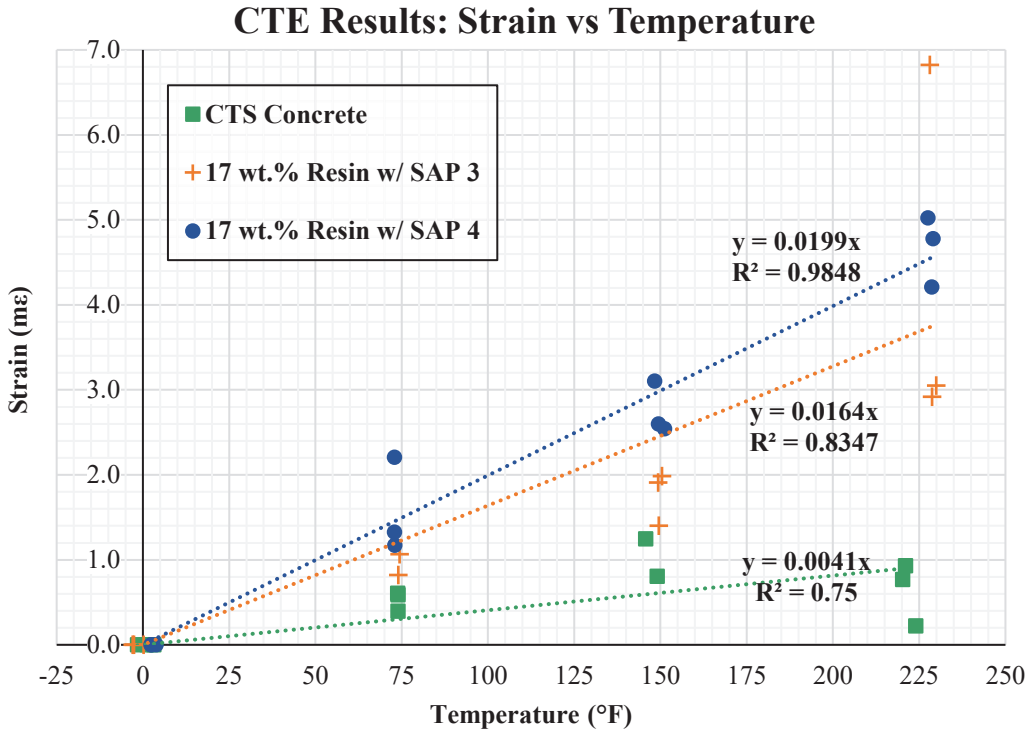

Figure 4.8.4: Strain vs. Temperature Plot

The slopes of each trendline estimated the CTE for their associated concrete mix. Table 4.8.1 summarizes the calculated CTE values in micro-strain per degree Fahrenheit (10^{-6} in/in/°F or με/°F). The R-squared values were also recorded to illustrate how closely the linear trendline fit the data. Specimen 3 of the PC with SAP 3 at room temperature and Specimen 3 of the CTS concrete at 150°F were omitted from the data as their calculated strains were negative and skewed the data.

Table 4.8.1: CTE Results from Strain vs. Temperature Plot

Concrete Mix	Coefficient of Thermal Expansion, CTE με/°F (10^{-6} in/in/°F)	R-Squared (R^2)
CTS Concrete	4.07	0.7500
Luna PC Phase II: 17 wt.% Resin w/ SAP 3	16.4	0.8340
Luna PC Phase II: 17 wt.% Resin w/ SAP 4	19.9	0.9848

The CTE for typical cementitious concretes ranges from 3.2 to 7.3 με/°F with an average around 5.5 με/°F [68–70]. The CTS concrete meets this range as it is similar to ordinary cementitious concretes. However, the Luna PC formulations are much higher. Previous studies have observed the CTE for PC is often 3 to 4 times higher than that of ordinary concretes, ranging from around 12.0 to 17.3 με/°F [71,72]. The Luna PC CTE are similar to these previous studies, though they are in the upper end of the range.

The coefficient of thermal expansion of aggregates ranges from 0.55 to 5 με/°C (0.3 to 2.7 με/°F) [70]. From this, it is most likely that the large CTE values for the Luna PC stem from the cured resin with very little contribution from the aggregates.

4.8.3 Conclusions

Both Luna PC mixes had a significantly higher CTE than the CTS concrete and exceed the allowable limit set by the TSPWG Manual of $7x10^{-6}$ in/in/°F. This higher CTE was expected as the resin itself has a higher CTE than cement paste. Nevertheless, these measurements are still a cause for concern as they are well beyond the threshold by an approximate factor of 2.3 and 2.8 for the SAP 3 and 4 mixes, respectively. Cracking along the edges and boundaries of the patches

may occur from the larger volumetric expansions due to temperature. Further tests must be performed to determine the impact this expansion would have on patch in the field.

The CTS concrete had a low R^2 value indicating that the trendline was not a close fit for the recorded data. Each of the strains recorded at 225°F temperature range appeared much lower than expected from the trendline and the other temperature ranges. This discrepancy most likely arose from precision and accuracy of the comparator. A tiny adjustment to the top seat, such as tilting it to one side, noticed a change in measurement of around 0.01 inches. While special care was taken to ensure each specimen was recorded as precisely as possible and in an identical manner, this error may have persisted from recording these bars at a different tilt than the other measurements.

5. SECTION I: DISCUSSION AND CONCLUSIONS

Taking into consideration the results of the performed tests, the Luna PC mix was down-selected to use 17 wt.% resin w/ SAP 4. The mix maintained strength properties similar to other PC mixes. It also had a higher workability that compacted and flowed similarly to typical cementitious-based concrete.

The mix used a 17 wt.% resin proportion due to its increased workability from resin acting as a lubricant to the aggregates, as well as its higher strength from a higher resin proportion. The mix utilized the 60:40 coarse-to-fine aggregate ratio using #78 graded dolomite and locally sourced natural sand. This ratio and the use of a finer graded CA with smaller maximum diameter allowed the mix to be more workable and increased the packing density of the concrete from a well-graded aggregate mix. The silica package, SAP 4, produced the desired thickening effect, which reduced the separation of the resin and aggregates, as well as reducing the leaching of the resin outside the molds or into cracks. The SAP also helped to increase the packing density of the mix allowing for the slump of the mix to better retain its shape, similar to ordinary cementitious concretes.

5.1 Comparison of Results and Cost-Benefit Analysis

Using the down-selected 17 wt.% resin w/ SAP 4 mix as the Luna PC, Table 5.1 summarizes the test results of each test performed and compares the results alongside the CTS Concrete. The TSPWG Manual requirements were also listed for each applicable test to be used as a guideline for the comparison. To quantify whether or not the Luna PC outperformed the CTS concrete, the Luna PC-to-CTS Concrete ratio was determined for each test by dividing the PC results by the CTS results, if applicable. The CTS concrete strength properties were taken from the specification sheets provided by CTS if these mechanical properties were not tested during the duration of this thesis [73].

Table 5.1: Material Property Results Summary and Comparison

Material Property	ASTM Standard	TSPWG Manual Requirement	Concrete Type						Luna PC-to-CTS Concrete Ratio
			CTS Concrete			Luna PC			
			Results	Units	Pass/Fail	Results	Units	Pass/Fail	
Compressive Strength	C39	2-hour: ≥ 2,500 psi	3000	psi (1)	**Pass**	8520	psi	**Pass**	2.84
		1-day: ≥ 4,000 psi	4680	psi	**Pass**	10310	psi	**Pass**	2.20
Flexural Strength	C78/C293	2-hour: ≥ 350 psi	--	psi	**Pass**	2830	psi	**Pass**	--
		7-days: ≥ 500 psi	765	psi (2)(3)	**Pass**	3780	psi (2)(3)	**Pass**	4.94
Bond Strength: Slant Shear	C882	1-day: ≥ 1,000 psi	1260	psi	**Pass**	1450	psi	**Pass**	1.15
Vertical Bond Strength	Modified C78	--	285	psi	**N/A**	490	psi (2)	**N/A**	1.72
Horizontal Bond Strength	Modified C293	--	735	psi	**N/A**	2825	psi (2)	**N/A**	3.84
Workability/Slump	C143	≥ 3 inches within 5 minutes of added water	2.25	in	**Fail** (4)	5.5	in	**Pass**	2.44
Modulus of Elasticity/Stiffness	C469	2-hour: ≥ 2,000 ksi and ≤ 6,000 ksi	4050	ksi (5)	**Pass**	2750	ksi	**Pass**	0.68
Coefficient of Thermal Expansion (CTE)	C531	≤ 7 με/°F	4.07	με/°F	**Pass**	19.9	με/°F	**Fail**	--

(1) - From CTS Specification for 1-hour of curing time [73]
(2) - Only performed using the Phase I Luna PC mix. Need to be retested using the down-selected Luna PC
(3) - Test performed at 5-day strength
(4) - CTS specifications report a slump consistency of 4 inches [73]
(5) - Test performed at ≥3-day strength

As observed in Table 5.1, the Luna PC outperformed the CTS concrete and passed the TSPWG requirements for each test apart from CTE. More tests are needed to determine the negative consequences of the high CTE of the PC for use as a repair material and whether the PC is adequate despite being beyond the limit. Modulus of elasticity is the other material property where the CTS concrete outperforms the Luna PC. The Luna PC is most advantageous in flexure strength compared to the CTS concrete by having nearly 5 times the strength.

An internal market assessment was performed on the unit costs for various competing PC currently available to the commercial market. From this market assessment, it was found that the cost of a commercial off the shelf (COTS) PC kit ranged from $100 to $200 per cubic foot. The CTS concrete can be purchased commercially for a unit cost of approximately $25 per cubic foot [74]. From comparing these unit prices, COTS PC is approximately 4 to 8 times more expensive than the CTS concrete.

Using the average of $150/cu ft for the COTS PC as the unit price of the developed PC, Table 5.2 compares the two repair materials strength properties per unit price. Values that are higher imply that the associated mix is the more economical of the two.

Table 5.2 – Comparison of the Repair Materials at a Cost Basis

Material Property	ASTM Standard	Concrete Type				Concrete Type	
		CTS Concrete		Luna PC		CTS Concrete	COTS PC[6]
		Results	Units	Results	Units	Strength per Unit Price Unit/($/cu.ft.)	
Compressive Strength	C39	3000	psi [1]	8520	psi	120	57
		4680	psi	10310	psi	187	69
Flexural Strength	C78/C293	--	psi	2830	psi	--	19
		765	psi [2][3]	3780	psi [2][3]	31	25
Bond Strength: Slant Shear	C882	1260	psi	1450	psi	50	10
Vertical Bond Strength	Modified C78	285	psi	490	psi [2]	11	3
Horizontal Bond Strength	Modified C293	735	psi	2825	psi [2]	29	19
Workability/Slump	C143	2.25	in	5.5	in	0.09	0.04
Modulus of Elasticity/Stiffness	C469	4050	ksi [5]	2750	ksi	162	18
Coefficient of Thermal Expansion (CTE)	C531	4.07	με/°F	19.9	με/°F	0.16	0.13

(1) - From CTS Specification for 1-hour of curing time [72]
(2) - Only performed using the Phase I Luna PC mix. Need to be retested using the down-selected Luna PC
(3) - Test performed at 5-day strength
(4) - CTS specifications report a slump consistency of 4 inches [72]
(5) - Test performed at ≥3-day strength
(6) - Commercial Off the Shelf (COTS) price was used when determining the strength per unit cost

As can be observed in Table 5.2, the CTS concrete is more economical in each test over the Luna PC at a strength per unit cost basis, using the COTS PC unit price. The Luna PC provides roughly half the economic efficiency of the CTS concrete for each strength property per unit cost. The key driving factor that increases the average cost of PC is the price to manufacture or purchase the resin and any other synthetically produced ingredients in the mix, such as SAP. If the cost of production, the proportioning of the resin or other costly ingredients were to be reduced, the economic viability of the PC would increase due to its higher unadjusted strengths.

Strength properties are not the only consideration for cost comparisons. Lower curing times and longer durability are not as easily quantifiable but can justify the increased cost. Lower curing times allow for rapid repair and let the patch become operational sooner, while a longer durability can help prevent future costs from further maintenance of the patch or the surrounding areas. These tests and analyses are beyond the scope of this thesis but may further emphasize the benefits or detriments of the PC.

5.2 Final Conclusions

The down-selected Luna PC formulation was found to be an adequate rigid repair material per the TSPWG requirements except for in CTE. Its increased strength properties and rapid curing make it viable for rapid repairs. When compared to CTS concrete, a current rapid repair material used by the military, the Luna PC outperforms it in every material property test aside from CTE and modulus of elasticity. In addition, it is estimated that through heat curing, a patch of Luna PC may be cured and ready for use within 1-hour after casting if heat cured for 15 minutes. Including the time to set up for the mix and cast, the time frame to complete the repair would be below or meet the current NATO standard of 4 hours and would significantly improve upon the 8 hour time frame for the current repair materials, such as the CTS concrete. The PC is currently uneconomical compared to the current patching materials, at a strength per unit cost basis. Further tests are needed to determine whether the increased cost of the PC is justifiable for other factors such as durability.

6. SECTION I: FUTURE WORK

The development of the Luna PC mix is still in the early phases and further tests are being performed on its different material properties.

- The TSPWG Manual was updated in the middle of Phase II. As a result, not all mechanical properties have been tested to meet these requirements. To meet the standards brought by the updated TSPWG Manual, many of the material properties will need to be retested for the down-selected mix at different curing times, such as compressive and flexural strength. If the design of the Luna PC is altered, any of the previously aforementioned tests must also be retested.
- The TSPWG Manual also has requirements on the bond strength of the repair material with itself. The slant shear tests will need to be performed with a half-cylinder of the PC as the base half cylinder and the cast half cylinder.
- As the PC will experience temperature cycling, specimens should be cast and subjected to freeze-thaw cycles then the strength properties of the patching material should be tested to determine if there is any loss of strength from these cycles.
- Fatigue is another consideration that needs to be tested. When used as a repair patch for runways, the repeated, cycled loads from the aircraft could lead to fatigue issues. A rolling load test with a C17 cart would simulate the impact of the aircraft on the patch and should be performed on the repair materials.
- The long-term durability of the PC needs to be determined. If the PC can withstand longer durations of extended use with little to no maintenance, this may assist in justifying the increased initial cost of the repair material through reducing the required maintenance costs.
- Larger scale tests of the patching material should be performed. These tests should simulate full scale patches in the field and can be cured by an industrial infrared (IR) heater. These tests

would also determine how well the patches can be cast using a drum mixer for larger batches and the use of readily available tools, such as trowels.

Initial large-scale tests have been performed on a 24”x24”x4” deep patch to observe how well the patch cures through its depth by applying heat to its surface with the IR heater. The curing time and the evenness of the applied heat and curing through the patch was recorded. Figure 6.1 to 6.6 show the Heat Design Equipment, HDE P200 IR heater, the PC being mix, and the patch being cast, and heat cured.

Figure 6.1: Luna Industrial IR Heater

Figure 6.2: Luna PC Mixing in Drum Mixer before Addition of FA

Figure 6.3: Luna PC Large-Scale Patch Filled to Half Depth

Figure 6.4: Luna PC Large-Scale Patch Cast to Full Depth

Figure 6.5: Luna PC Large-Scale Patch under IR Heater

Figure 6.6: Luna PC Large-Scale Patch after Heat Curing

Section II: Energy Dissipation of 3D Printed Plastic-Concrete Composite Beams

7. SECTION II: MATERIALS, CASTING, & TESTING PROCEDURES

7.1 Concrete Materials

An ASTM C150 Type I/II Portland cement was used as the binder for the cement paste [52]. To increase its strength and modulus, silica fume was substituted for 10% of the cement content. A w/c ratio of 0.30 was used. The mix design for 100 cu in of cement paste is summarized in Table 7.1. To increase the workability of the mix, approximately 20 mL of a polycarboxylate-based superplasticizer was introduced, as needed.

Table 7.1: Cement Paste Mix Design

Material Weight (g)			
Portland Cement	**Silica Fume**	**Water**	**Total**
2,388.6	265.4	796.2	**2,653.9**
w/c ratio = 0.30			

To determine the compressive strength of the mix, ASTM C109 was performed on 2" cube specimens of the cement paste after 14 days of curing [55]. The specimens were loaded at a constant rate of 35 psi/s until failure and the maximum load applied was recorded. Table 7.2 shows the results of the compression tests recorded to the nearest 10 psi. The average and standard deviation of the compressive strength was also recorded.

Table 7.2: Compressive Strength Results for Cement Paste at 14-day Strength

Specimen Identifier	Ultimate Load, P (lbs)	Compressive Strength, f_m (psi)	Average Compressive Strength (psi)	Standard Deviation (psi)
1	33,124	8,280	9,630	940
2	40,268	10,070		
3	43,556	10,890		
4	35,820	8,960		
5	40,588	10,150		
6	37,584	9,400		

7.2 Polymer Materials

The plastic molds that acted as the mortar structure were 3D-printed in the 3D Design Studio located in the Carol M. Newman Library at Virginia Tech. The specimens were printed using a polylactic acid (PLA) filament. PLA has an average tensile strength at room temperature of 69.4 MPa and average modulus of elasticity of 2.54 GPa [75]. The plastic molds had outside dimension of 3”x3”x8” with a 0.1”x0.25” notch at the bottom center of the beam. The thickness of the outer plastic shell was 0.25 in with the thickness at the bottom of the shell increased to 0.5 in to accommodate the notch. Figure 7.1 illustrates a plastic mold and its dimensions after 3D-printing.

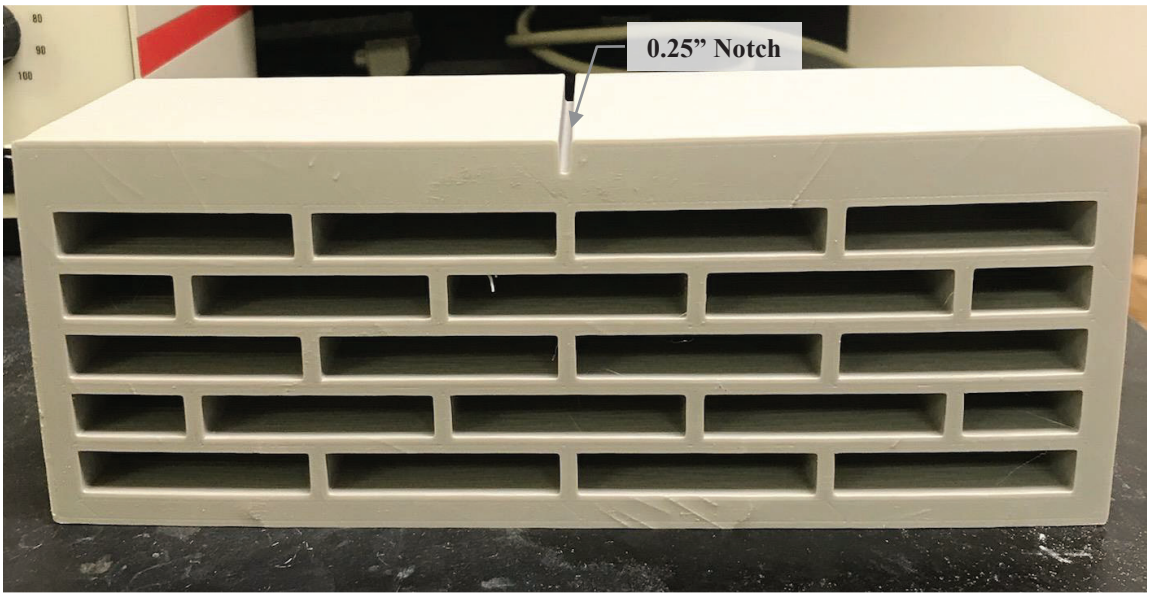

Figure 7.1: 3D-Printed Plastic Mold Example

7.2.1 3D-Printed Plastic Mold Nomenclature

Three beam types were created: the control specimens (Controls), specimens with three rows of blocks (3-Rows), and specimens with five rows of blocks (5-Rows). The Controls were 3D-printed with a single center block. The 3-Row and 5-Row specimens then varied the number of blocks that were subdivided and the thickness of the plastic between each block. 3-Row specimens used either 10 or 16 blocks, while 5-Row specimens used either 17 or 22 blocks. The thickness of the plastic between blocks was either 0.1 or 0.25 inches.

To better identify the different types of molds used, a naming convention was created to distinguish between the patterns of the 3-Row and 5-Row specimens. The notation for each beam listed the number of rows, blocks, and the plastic thickness:

[Rows]R-[Blocks]B-[Thickness]T

For the example beam shown in Figure 7.2, the beam has 3 rows, a total of 10 blocks on its face, and the thickness between each block is 0.1 inches. Following the naming convention above, the beam was named **3R-10B-0.1T**.

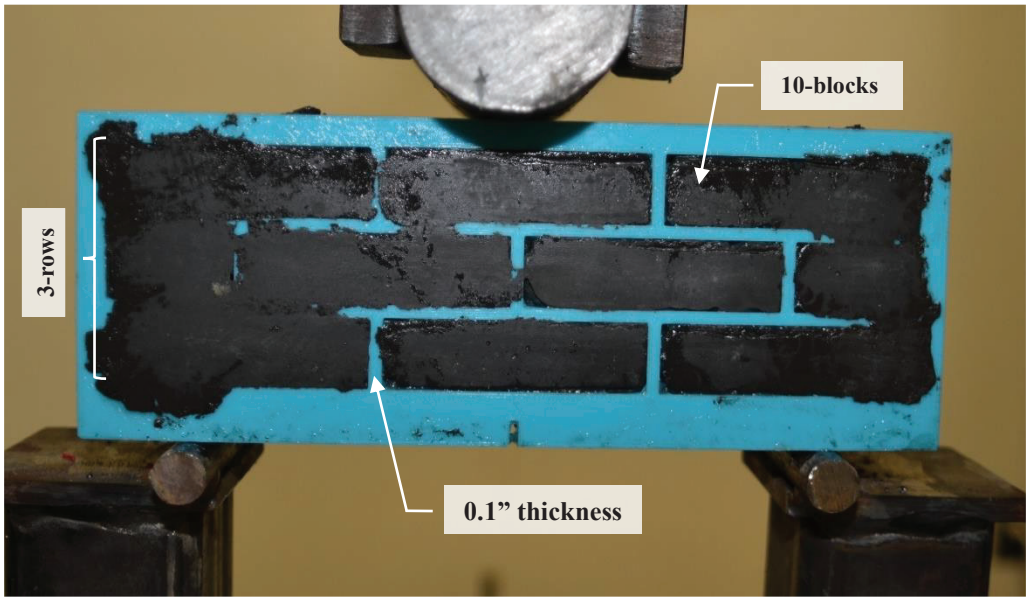

Figure 7.2: Beam Notation Example Beam

7.3 Casting Procedures

Each plastic mold was 3D-printed prior to casting of the cement paste. The cement paste was mixed following the procedures of ASTM C309 [76]. The water was first introduced to the mixing bowl, then the cement and SF were added. The bowl was then covered to prevent any loss of the cement or SF. The paste was mixed at a slow speed for 30 seconds then increased to a medium speed for an extra 90 seconds. The paste was then poured into each mold and each block was rodded to rid the paste of air voids and allow it to settle in the mold. Once the mold was filled, the top surface was smoothed using a trowel and covered using a plastic sheet to prevent the loss of moisture. The specimens then cured for 14-days prior to testing.

7.4 Testing Procedures

Once cured, prior to testing, the front face of the beams was spray-painted white and then sprayed over with a black speckled pattern. Figure 7.3 shows a control beam with the speckled pattern loaded inside the testing apparatus. This allowed for the DIC to determine the localized stresses, strains, and displacements along its face. The DIC camera was calibrated, and great care was taken to ensure there was no movement or impact with the camera. Figure 7.4 shows the set up DIC camera after calibration and data output.

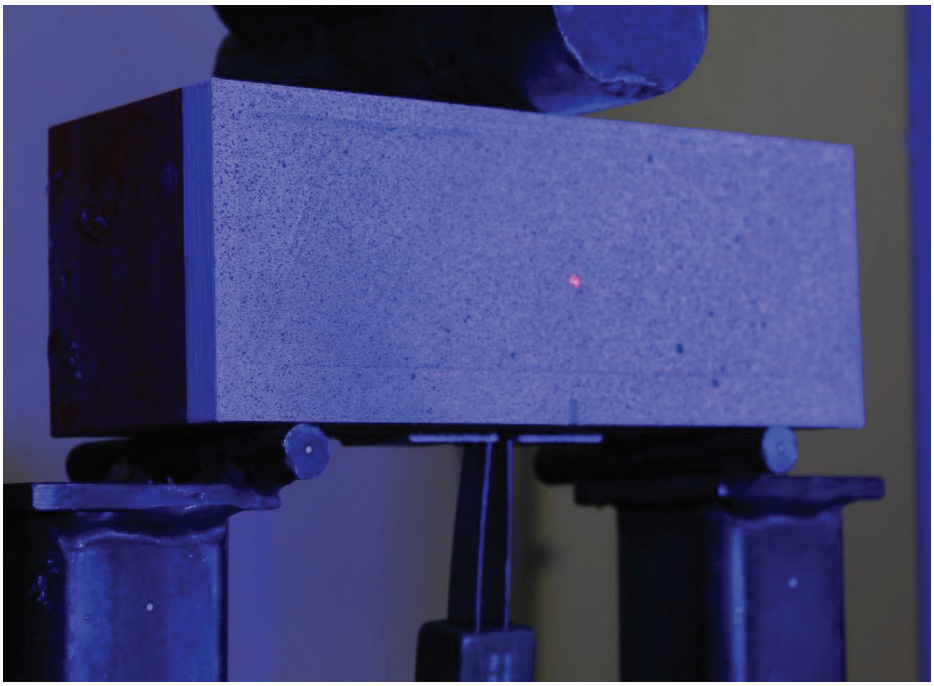

Figure 7.3: Control 2 with Speckled Pattern Prior to Testing

Figure 7.4: DIC Camera and Data Capture

Each specimen was tested following the procedures of a modified version of ASTM C293 for center-point loading [60]. The beams were centered in the testing apparatus, with a span length

between supports of 6 inches. Figure 7.5 shows Control specimen 2 loaded in the testing apparatus prior to testing. The beams were loaded at a constant rate of 1 mm/min until failure was observed or until the applied load of the specimen remained relatively constant while experiencing increasing deformation. The applied load and load head displacement were recorded with time. Pictures of each specimen were taken and are located in Appendix D.

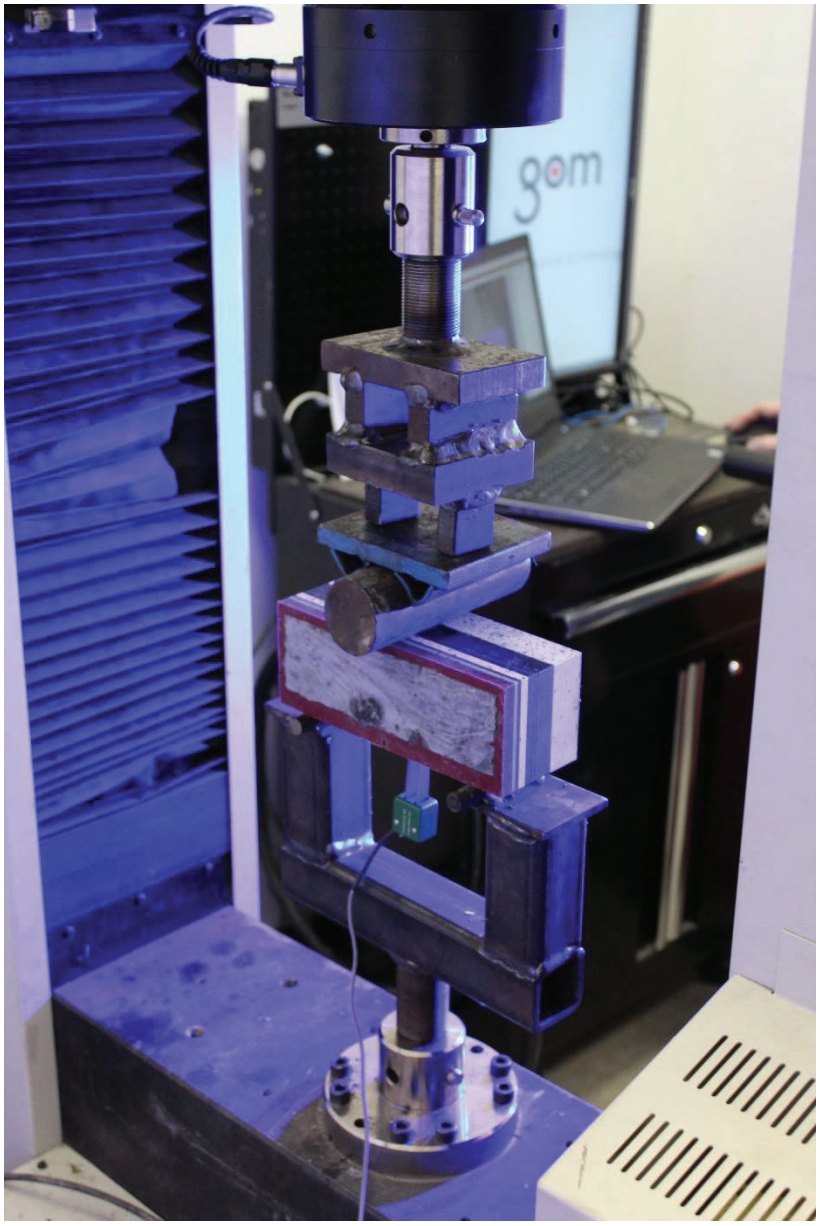

Figure 7.5: Control 2 Centered in Testing Apparatus Prior to Testing

Using the DIC, the crack mouth displacements (CMOD) and localized strains along the beam were calculated along the face of the beam for each frame taken. Figure 7.6 shows a sample output of the DIC data for Control 2 just before complete failure. The maximum strains at the concrete cracks and in the 3D-printed plastic were called-out and a gradient of the strains were shown. In addition, the CMOD of the beam was also displayed in mm. Each of these were plotted over each frame taken, as shown in the right portion of the figure.

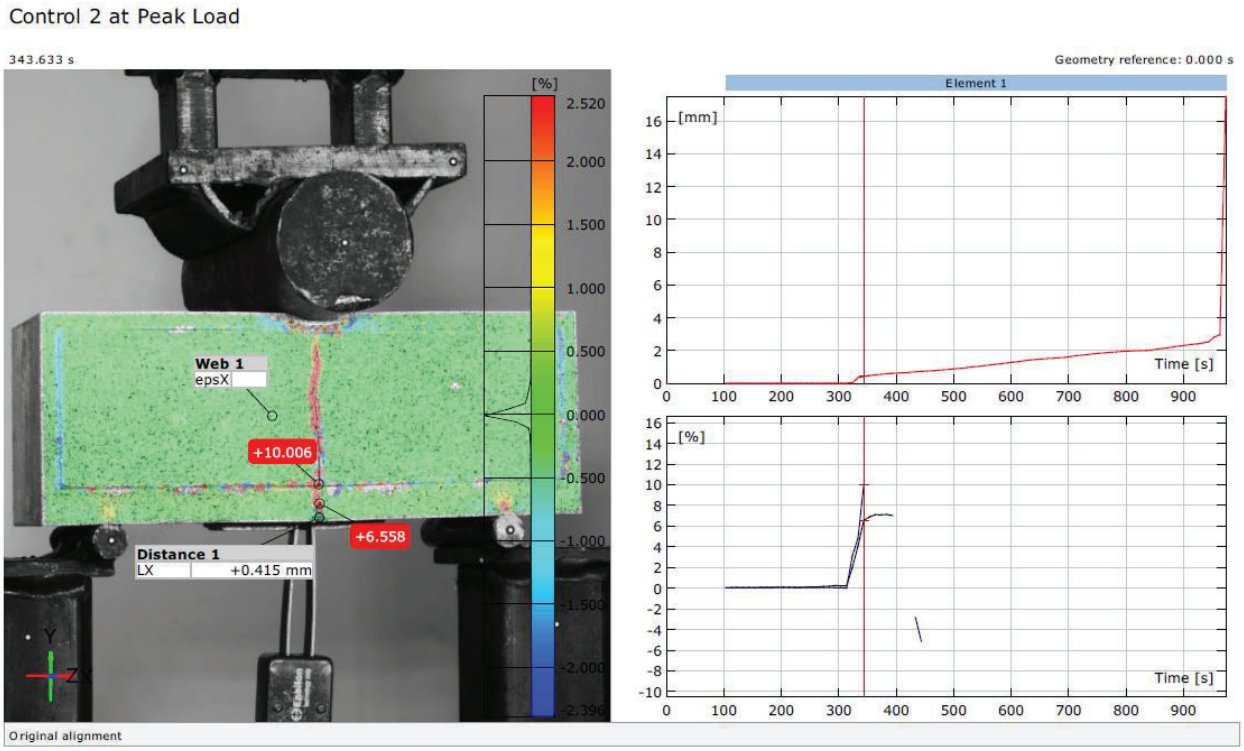

Figure 7.6: DIC Data Sample Output for Control 2

8. SECTION II: RESULTS AND DISCUSSION

8.1 Results and Observations

Using the CMOD measured from the DIC data, the applied load was plotted against the CMOD for each specimen. All tests results were combined and plotted in Figure 8.1. Figures 8.2 to 8.4 separate the results into the Control, 3-Row, and 5-Row groups, respectively.

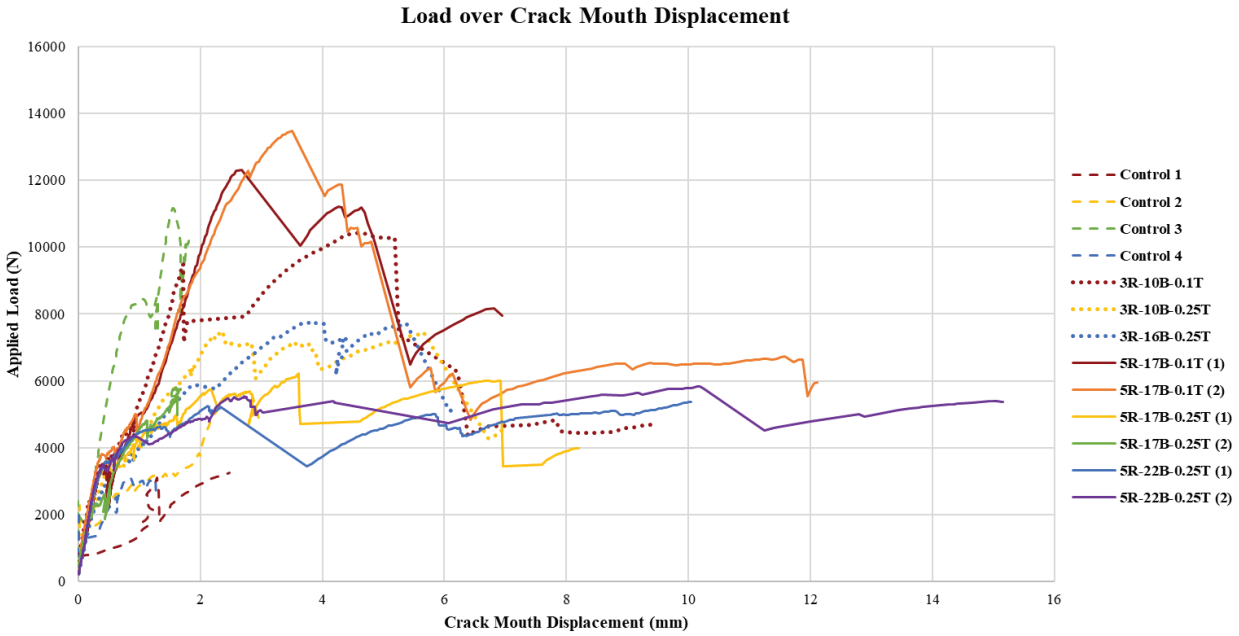

Figure 8.1: Load vs. CMOD – All Results

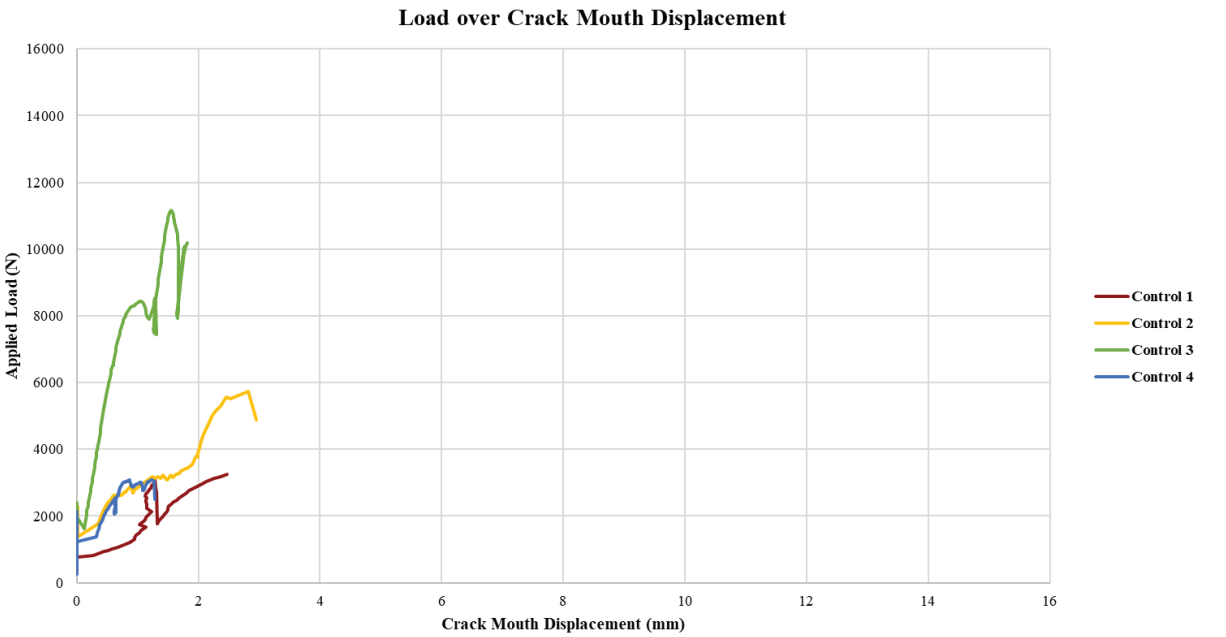

Figure 8.2: Load vs. CMOD – Control Specimens

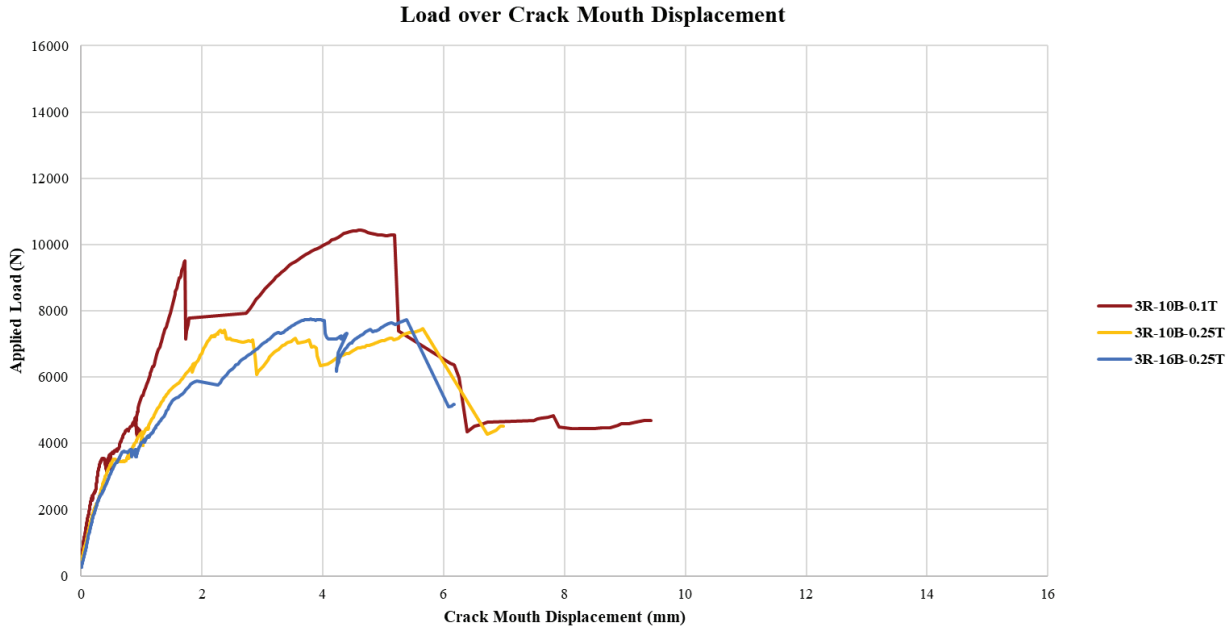

Figure 8.3: Load vs. CMOD – 3-Row Specimens

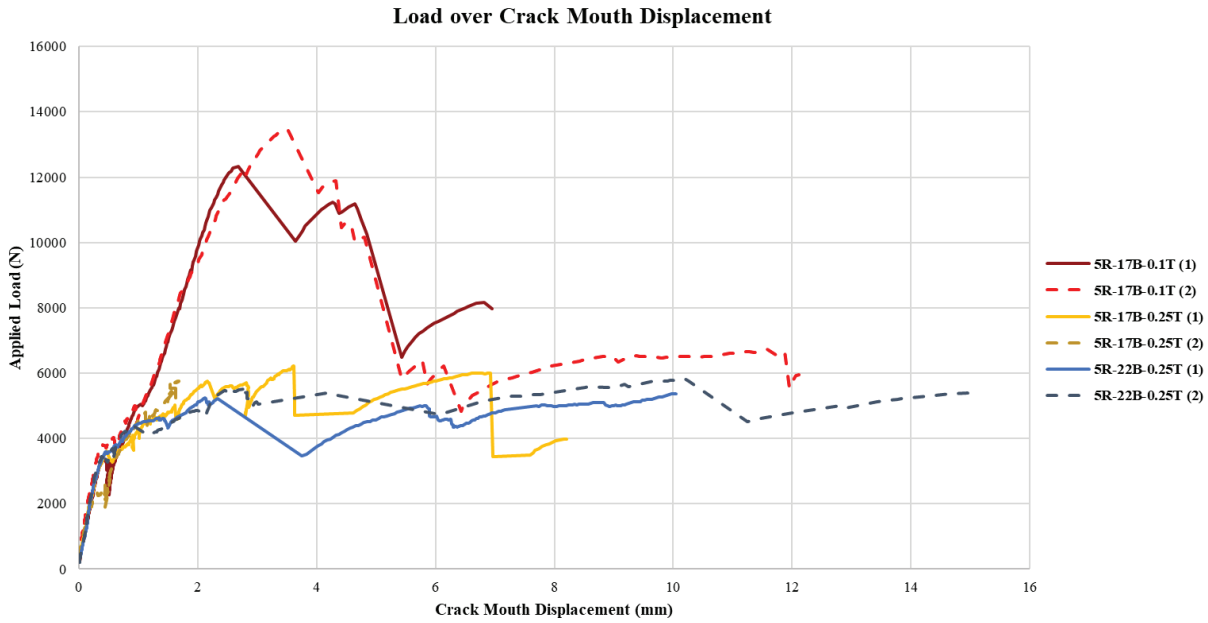

Figure 8.4: Load vs. CMOD – 5-Row Specimens

For each specimen, the peak load, the CMOD at peak load, and CMOD at failure were recorded newtons and millimeters, respectively. A summary of these results can be found in Table 8.1. Value bars have been included in the table to more clearly visualize which specimens performed better compared to the others. Because not all specimens observed a complete failure when the test was stopped, the final column of Table 8.1 lists whether the specimen had failed or if the test had been stopped.

Table 8.1: Summary of Load vs. CMOD Curves

Specimen	Peak Load P, N	CMOD at Peak Load e, mm	CMOD at Failure e, mm	Did Specimen Fail?
Control 1	**3,411**	2.48	**2.48**	Yes
Control 2	**5,737**	2.82	**2.96**	Yes
Control 3	**11,164**	1.56	**1.82**	Yes
Control 4	**3,088**	1.28	**1.28**	Yes
3R-10B-0.1T	**10,439**	4.64	**9.43**	No
3R-10B-0.25T	**7,456**	6.52	**6.98**	Yes
3R-16B-0.25T	**7,746**	3.79	**6.18**	Yes
5R-17B-0.1T (1)	**12,317**	2.91	**6.95**	No
5R-17B-0.1T (2)	**13,465**	3.82	**12.11**	No
5R-17B-0.25T (1)	**6,223**	3.61	**7.84**	No
5R-17B-0.25T (2)	**5,797**	1.60	**1.63**	Yes
5R-22B-0.25T (1)	**5,375**	10.05	**10.05**	Yes
5R-22B-0.25T (2)	**6,112**	3.89	**15.15**	No

To estimate the energy dissipation as the beam deflects from the subjected load, the area under the Load vs. CMOD curves was calculated for each specimen. The area was recorded to the nearest 0.1 N-m. Because the pattern of the cement paste bricks and plastic varied between specimens, the cross-sectional area of polymer was determined at the notch and divided by the total cross-sectional area of the beam of 9 in^2. This was recorded as the percent polymer (%polymer) for each specimen and was recorded to the nearest 0.1%. The area under the Load vs. CMOD curves was then normalized by using Equation 10:

$$A_{\%P} = A * \%P \tag{10}$$

Where $A_{\%P}$ is the normalized area under the load vs. CMOD curve in N-m, A is the unadjusted area under the load vs. CMOD curve in N-m, and %P is the %polymer at the cross-section of the notch.

The fracture energy of each specimen was determined using the method described in Hillerborg, 1985 [77]. Because the exact weights of the specimens were unknown, the fracture energy equation was modified in Equation 11:

$$G_F = \frac{1550A}{A_{lig}} \tag{11}$$

Where G_F is the calculated fracture energy of the specimen at failure or when the test was stopped in N/m, A is the unadjusted area under the load vs. CMOD curve in N-m, and A_{lig} is the cross-sectional area of the specimen at the notch in square inches. For the 3"x3"x8" beam specimens, the cross-sectional area at the notch of 8.75 in^2 was used in determining the fracture energy.

The fracture energy was normalized also using Equation 11 by substituting the area, A, with the normalized area, $A_{\%P}$. The fracture energies were calculated to the nearest 1 N/m. A summary of both the normalized and unadjusted areas, normalized and unadjusted fracture energy, as well as the %polymer for each specimen, can be found in Table 8.2.

Table 8.2: Summary of Calculated Areas, Fracture Energy, and %Polymer

Specimen	Area Under Load vs. CMOD A, N-m	Fracture Energy G_F, N/m	%Polymer @ Notch Cross-Section %P	Normalized Area Under Load vs. CMOD $A_{\%P}$, N-m	Normalized Fracture Energy $G_{F,\%P}$, N/m
Control 1	4.9	913	25.0%	1.2	228
Control 2	10.5	1965	25.0%	2.6	491
Control 3	13.1	2457	25.0%	3.3	614
Control 4	3.0	556	25.0%	0.7	139
3R-10B-0.1T	62.5	11751	54.4%	34.1	6398
3R-10B-0.25T	41.3	7751	61.1%	25.2	4736
3R-16B-0.25T	36.8	6915	80.6%	29.7	5571
5R-17B-0.1T (1)	58.2	10943	63.0%	36.7	6894
5R-17B-0.1T (2)	90.3	16960	63.0%	56.9	10685
5R-17B-0.25T (1)	39.4	7396	66.7%	26.2	4930
5R-17B-0.25T (2)	7.0	1306	66.7%	4.6	871
5R-22B-0.25T (1)	45.6	8560	83.3%	38.0	7134
5R-22B-0.25T (2)	76.3	14342	83.3%	63.6	11952

The calculated areas under the load vs. CMOD curves were displayed graphically in Figures 8.5 and 8.6 for the unadjusted and normalized areas, respectively. The Controls, 3-Row, and 5-Row specimens were grouped together to better compare like specimens.

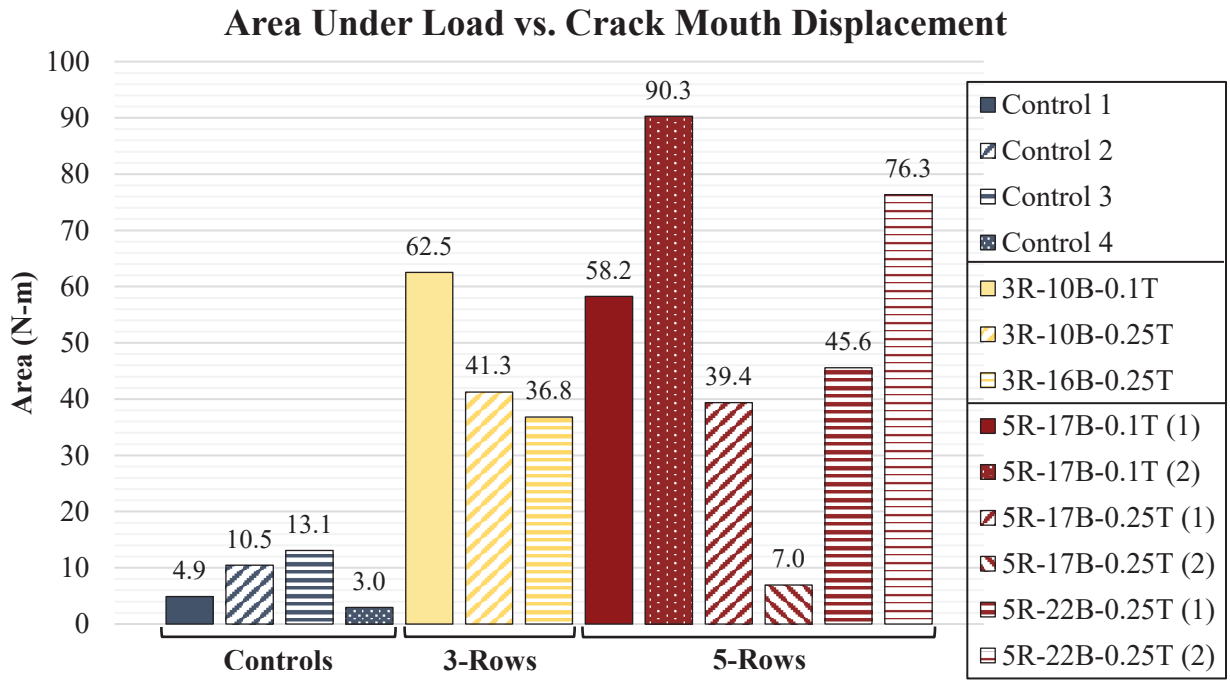

Figure 8.5: Unadjusted Area Under Load vs. CMOD Curves

The calculated fracture energy for each specimen was displayed graphically in Figures 8.7 and 8.8 for the unadjusted and normalized fracture energy, respectively. The Controls, 3-Row, and 5-Row specimens were grouped together to better compare like specimens.

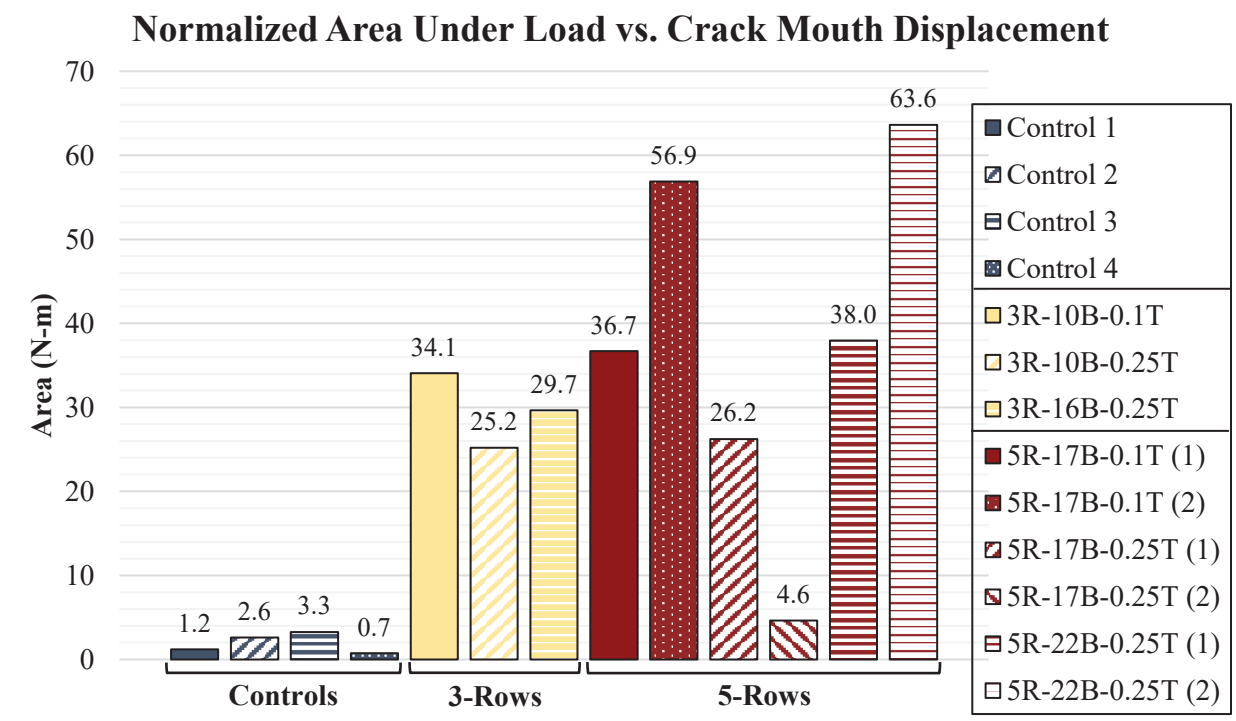

Figure 8.6: Normalized Area Under Load vs. CMOD Curves

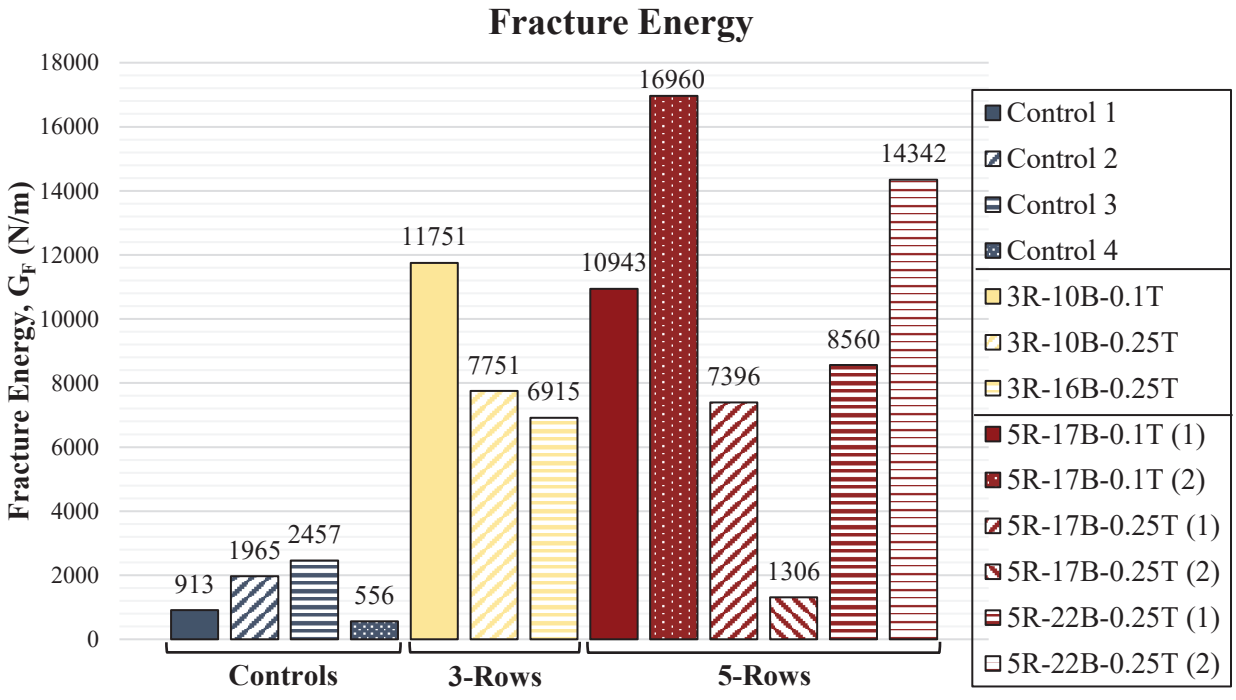

Figure 8.7: Unadjusted Fracture Energy of Each Specimen

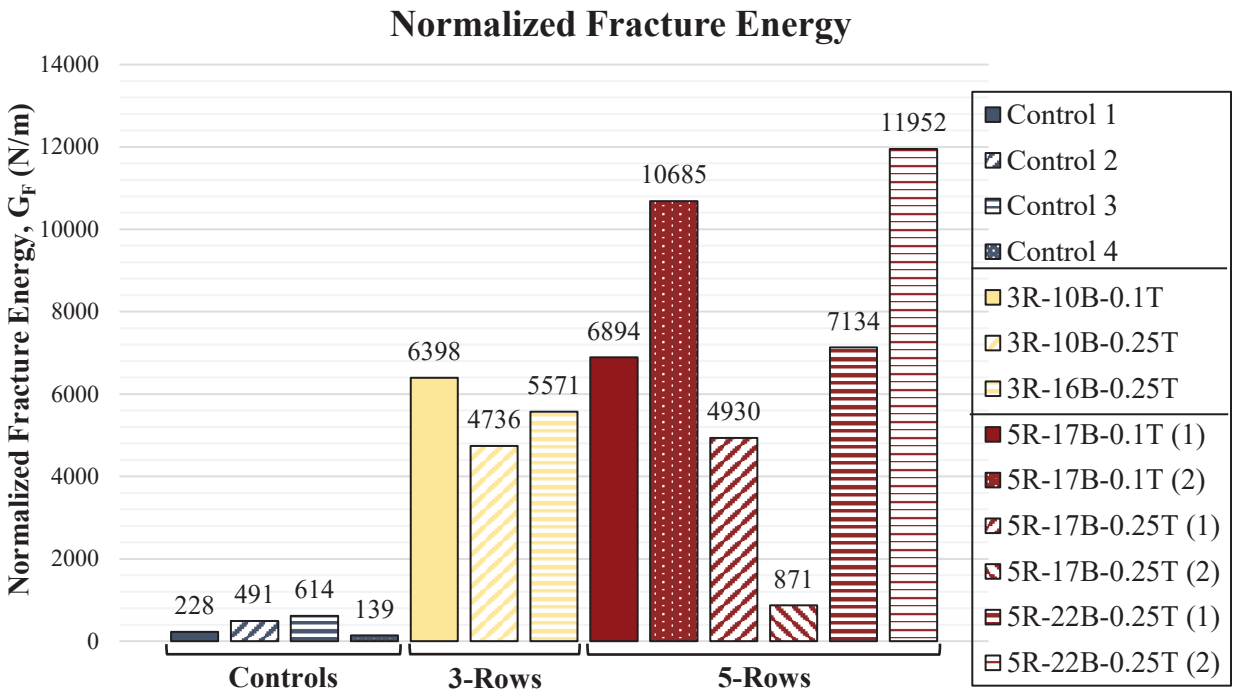

Figure 8.8: Normalized Fracture Energy of Each Specimen

The toughness index is the measure of the amount of energy required to deflect the beam by a given amount compared to the energy required to bring the beam to the point of first crack [78]. This definition has been adjusted to use the CMOD rather than the deflection of the beam. The energy required to deflect the beam by a given amount was found using the unadjusted areas under the load vs. CMOD curves at failure of the beams. The energy required to bring the beam back to the point of the first crack was estimated by taking the area of the load vs. CMOD curve at the peak load. The calculation for the toughness index is given by Equation 12:

$$I = \frac{1000A}{\frac{1}{2}Pe} \tag{12}$$

where I is the toughness index, A is the area under the load vs. CMOD curves in N-m, P is the peak load in N, and e is the CMOD at peak load in mm. A summary of the toughness index

calculation is given in Table 8.2. The toughness index results using the idealized calculation from Equation 11 for each specimen were displayed graphically in Figure 8.9.

Table 8.3: Toughness Index Calculations

Specimen	Peak Load P, N	CMOD at Peak Load e, mm	Area Under Load A, N-m	Normalized Area Under Load $A_{\%P}$, N-m	Toughness Index I	Normalized Toughness Index $I_{\%P}$
Control 1	3,411	2.48	4.9	1.2	0.576	0.144
Control 2	5,737	2.82	10.5	2.6	0.646	0.161
Control 3	11,164	1.56	13.1	3.3	0.752	0.188
Control 4	3,088	1.28	3.0	0.7	0.749	0.187
3R-10B-0.1T	10,439	4.64	62.5	34.1	1.290	0.703
3R-10B-0.25T	7,456	6.52	41.3	25.2	0.848	0.518
3R-16B-0.25T	7,746	3.79	36.8	29.7	1.253	1.010
5R-17B-0.1T (1)	12,317	2.91	58.2	36.7	1.627	1.025
5R-17B-0.1T (2)	13,465	3.82	90.3	56.9	1.756	1.107
5R-17B-0.25T (1)	6,223	3.61	39.4	26.2	1.750	1.167
5R-17B-0.25T (2)	5,797	1.60	7.0	4.6	0.748	0.499
5R-22B-0.25T (1)	5,375	10.05	45.6	38.0	0.844	0.703
5R-22B-0.25T (2)	6,112	3.89	76.3	63.6	3.212	2.676

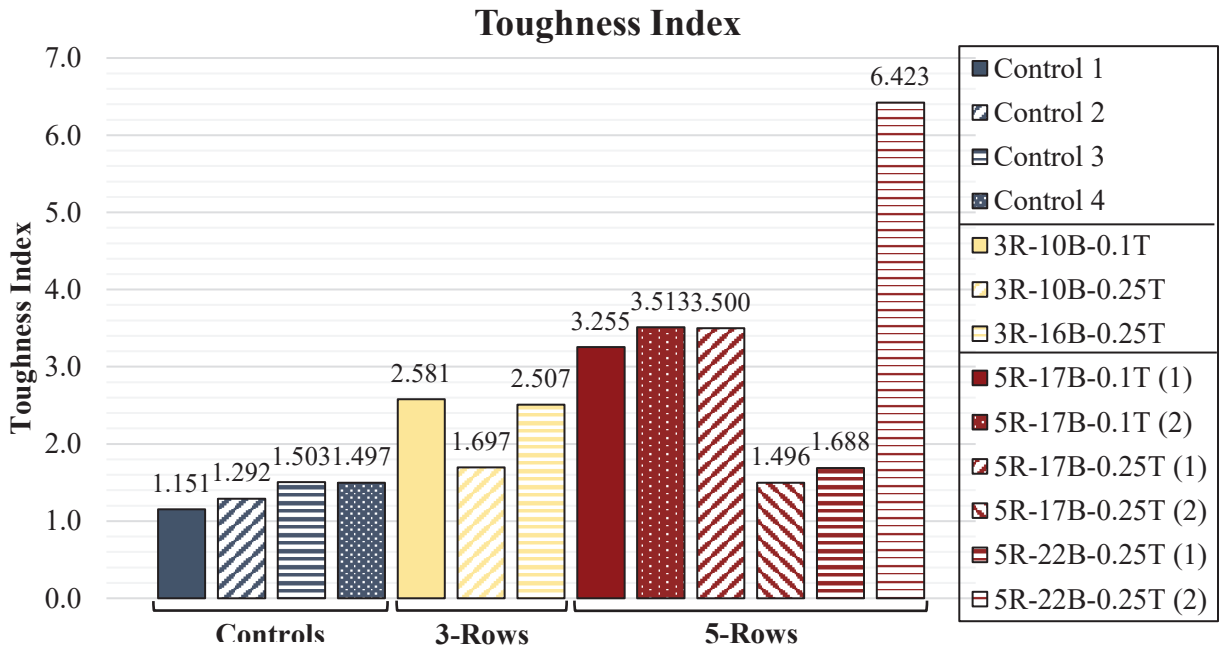

Figure 8.9: Unadjusted Toughness Index Results

Figurea 8.10 through 8.13 show the DIC output for the specimen 5R-17B-0.1T (2). Various pictures were taken at CMOD of 0.0, 0.5, 1.0, 2.0, 3.0 mm. Pictures were then taken at failure of the bottom brick layer, second from the bottom brick layer, and then when the test was stopped.

The gradient on the face of the member shows the localized strains in the x-direction. The strains ranged from 1.5% in compression to 2.1% in tension, as displayed with the color scale on the right side of each picture. Red was used to denote the strains in tension and blue to denote the strains that were in compression.

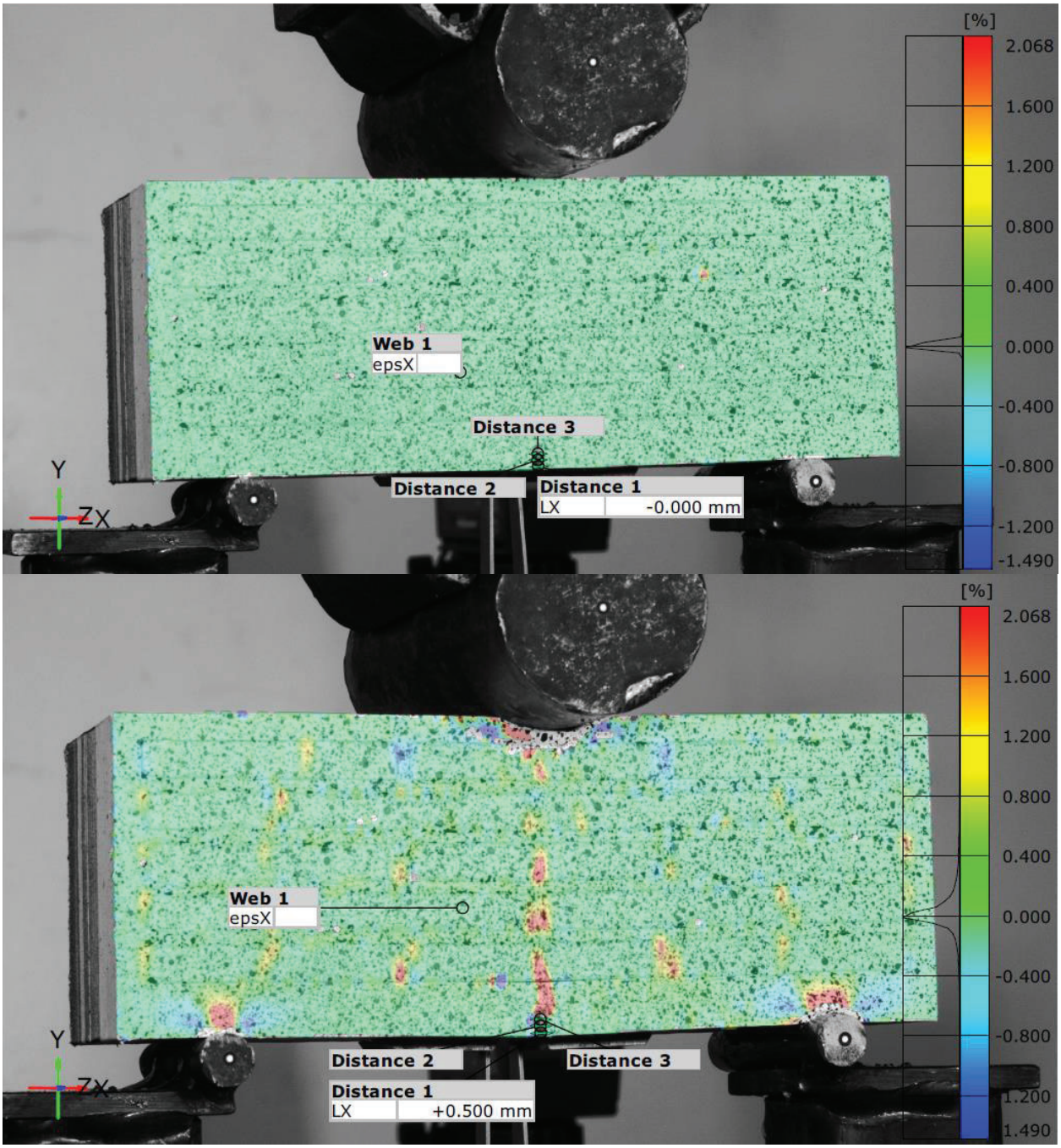

Figure 8.10: Specimen 5R-17B-0.1T (2) DIC Output at 0.0 mm (Top) and 0.5 mm CMOD (Bottom)

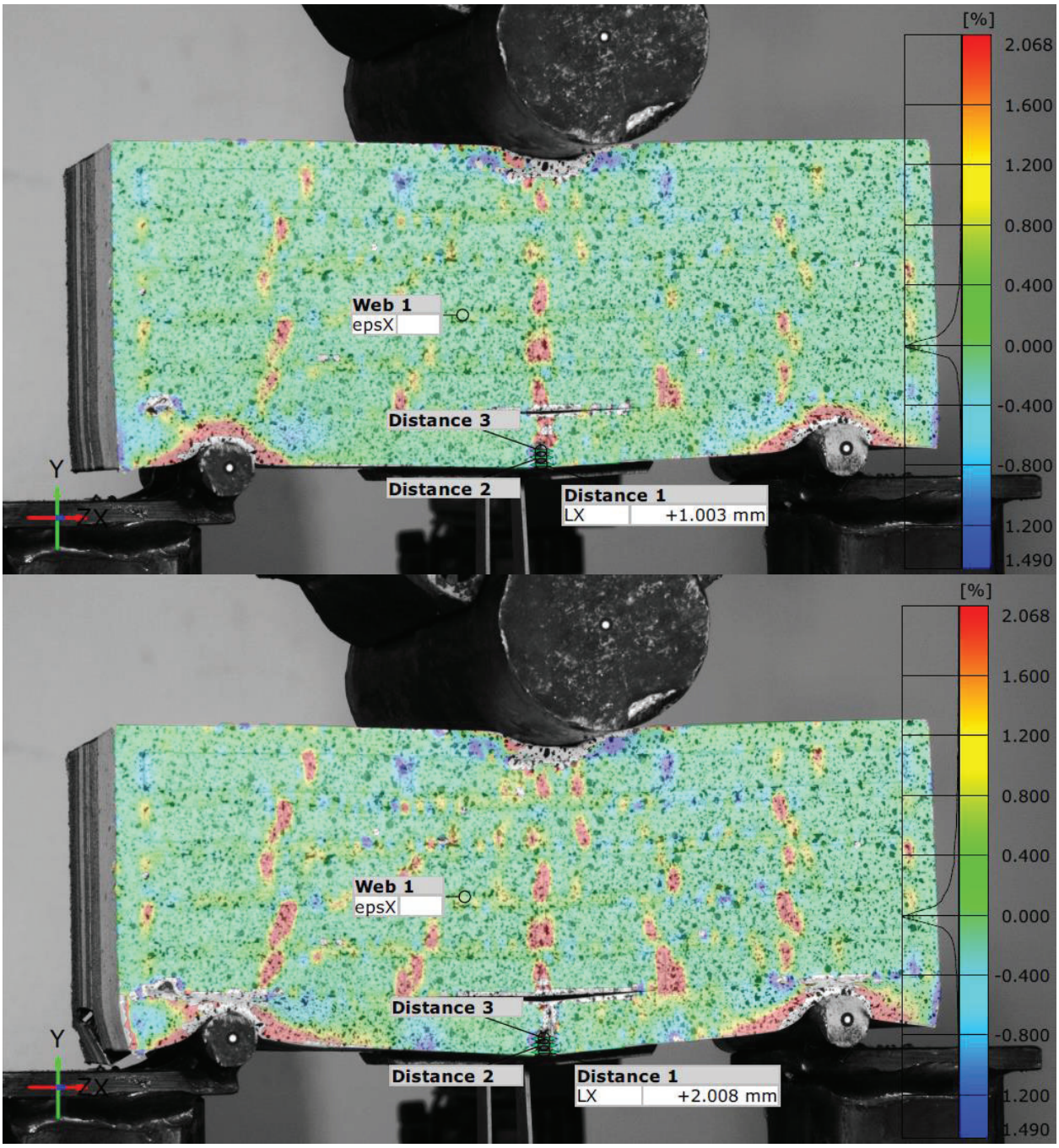

Figure 8.11: Specimen 5R-17B-0.1T (2) DIC Output at 1.0 mm (Top) and 2.0 mm CMOD (Bottom)

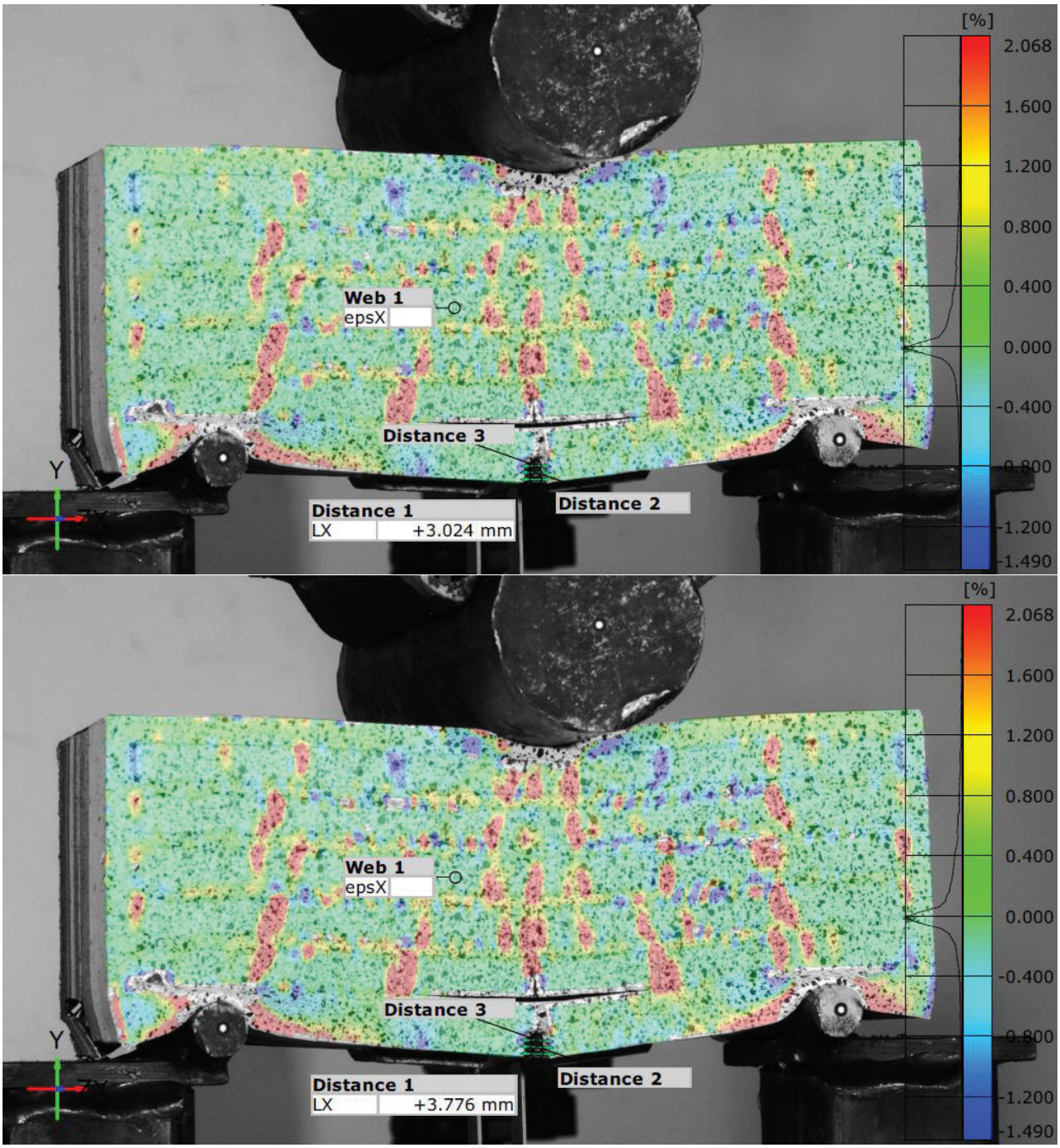

Figure 8.12: Specimen 5R-17B-0.1T (2) DIC Output at 3.0 mm CMOD (Top) and Bottom Brick Layer Failure (Bottom)

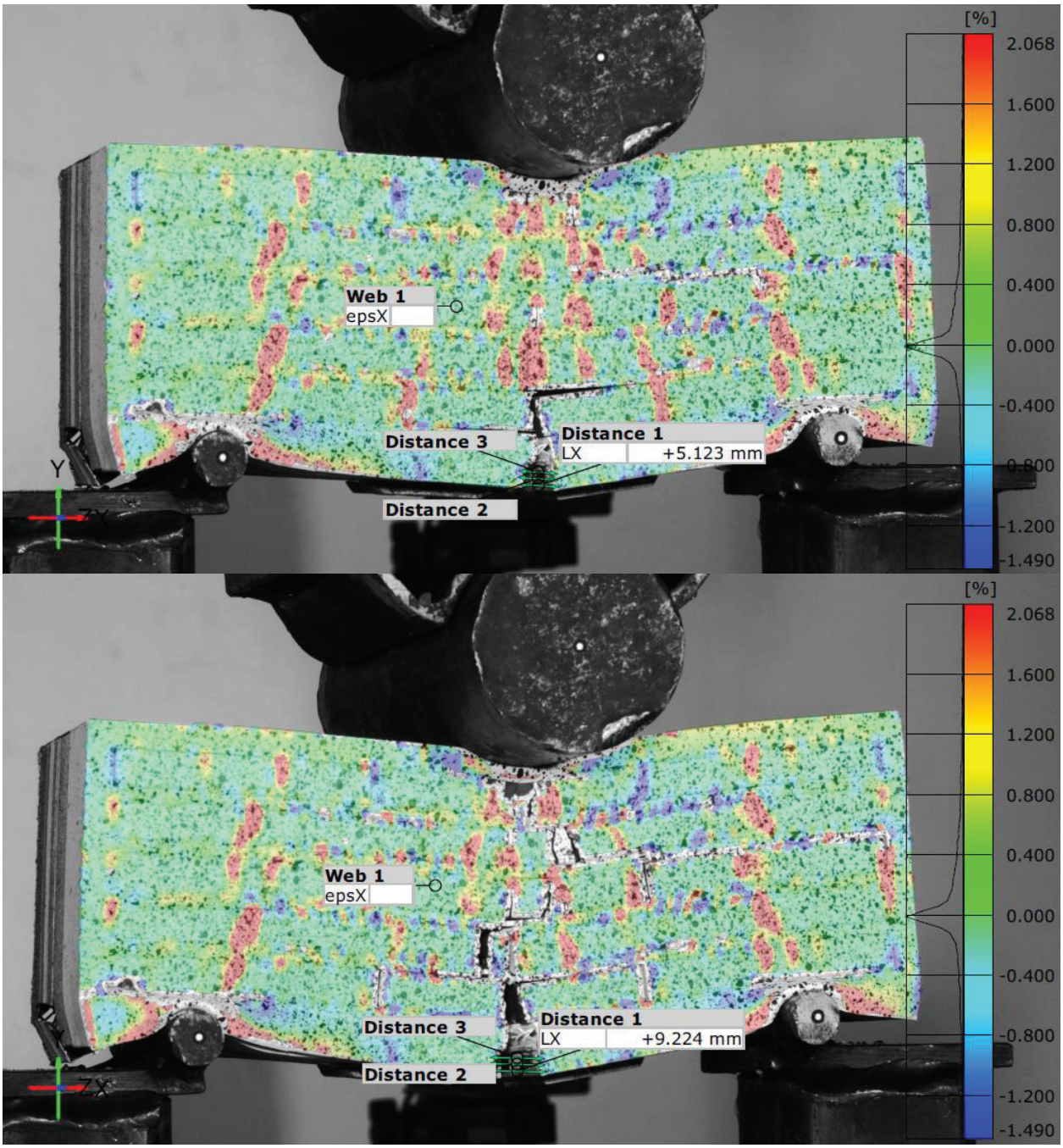

Figure 8.13: Specimen 5R-17B-0.1T (2) DIC Output at Second from Bottom Brick Layer Failure (Top) and Test End (Bottom)

Cracks did not form until approximately 0.5 mm of CMOD was observed, as show in Figure 8.10. The red locations show cracks forming along the center of the beam in both the concrete brick and in the plastic joints. This shows the beam acting compositely up to this point. When the initial crack formed in the bottom tension brick, the load was shown to redistribute to

the surrounding bricks through the plastic joints. This is reflected by the red areas in the middle-thirds of the bottom brick layer in the 0.5 mm CMOD picture.

Deformation of the plastic at the supports and load head were observed around 1 mm of CMOD, as shown Figure 8.11. The concrete brick began to delaminate with the plastic as the beam further deformed with more applied load. More tension locations and cracks were observed in regions outside the center of the beam, further reflecting the load redistribution of the beam.

Delamination of the concrete and plastic were observed in more layers than the bottom brick layer after 2.0 mm of CMOD, as shown in Figure 8.12 by the various “dots” of red and blue along the horizontal plane where the concrete brick meets the horizontal plastic joint. At approximately 3.78 mm of CMOD, complete failure of the center brick in the bottom most layer was observed. Redistribution of the load occurred immediately and simultaneously.

Similar redistribution occurred when the second from the bottom layer failed in the edges of the concrete next to the center plastic joint, as seen in Figure 8.13. When the test was concluded, tension cracks were observed in each of the center concrete bricks, as shown in Figure 8.13. The specimen had yet to completely fail as the 3D printed plastic was still intact and transferring the load to the concrete that had yet to failed and to the supports. The continued to deflect indefinitely without much increase in load, due to the failure of the center concrete bricks, which is why the test was stopped.

Similar phenomenon was observed in the other bioinspired nacreous beams except for the control specimens. Without another concrete layer to redistribute the stresses in the beam, when the singular concrete brick failed, so too did the composite beam.

8.2 Discussion of Results

The Control specimens did not experience any significant increase in CMOD after the initial crack. This lack of increased deflection made the beams more brittle than the 3-Row and 5-Row specimens, and they had much lower areas under the curve as a result. Except for Control 3, the Controls experienced lower peak loads as well, which further aided to their lower areas.

Overall, the 3-Row specimens experienced much larger CMOD and peak loads. Failure of the beams was noticed after 5 mm of CMOD, and the load vs. CMOD curves were fairly consistent for each of the three specimens. The 3R-10B-0.1T specimen had the largest area under the curve of the 3-Row specimens. This was due to having the highest peak load and CMOD of this group.

In general, the 5-Row specimen group had the highest peak loads and the largest CMOD. As a result, this group had some of the highest areas under the curve and fracture energy. This is most likely a result of these beams having larger %polymer cross-sections at the notch, which allowed more of the polymer joints to deform plastically rather than the brittle cement paste. As observed in Figure 8.4, the applied load began to level around 5,000 N to 7,000 N as the beam continued to deform. Because of this flat region, it was unclear when to stop the test. The specimens that deformed for longer produced higher areas under the curve, which may have skewed their results from not stopping the tests earlier. The 5R-17B-0.1T specimens produced similar tall and wide load vs. CMOD curves, which produced higher areas. The 5R-22B-0.25T specimens had the largest recorded CMOD, but relatively low and flat load vs. CMOD curves.

For all load vs. CMOD plots, the curves appeared very linear until approximately 0.5 mm of CMOD or 3,500 N of applied load. After which, the slopes of the curves flattened, and the curves began to diverge, as observed in Figure 8.1. The specimens with a plastic thickness of 0.1 inches had more of the desired tall and wide load vs. CMOD curves, which produced higher areas

under the curves. Whereas the specimens with 0.25” plastic thicknesses experienced lower and flatter curves that extended for longer, on average.

When normalizing the area, both the 3-Row and 5-Row groups greatly outperformed the Controls. Specimen 3R-10B-0.1T observed the highest normalized area of the 3-Row group, and specimens 5R-17B-0.1T (2) and 5R-22B-0.25T (2) recorded the highest normalized area of the 5-Row group and overall.

After observing the load vs. CMOD curves, it was noted that some specimens did not observed the ideal behavior assumed when initially deriving Equation 11. When developing that equation, a linear slope up until the peak load was assumed generating a triangular area for the denominator. Considering several specimens had peak loads after plastic deformations were noted and some specimens never achieved a clearly identified peak, this idealistic calculation was not representative of the data and potentially skewed the toughness index results. Due to the unique load vs. CMOD curves brought by these specimens, conventional procedures may not apply in calculating the toughness index.

Rather than assuming the peak load as the end of the linear region, the calculations should be performed again using more precise values of the load and CMOD at that load where the curves begin to enter plastic deformation. Future analysis shall be performed to better determine which specimen configuration produced the highest toughness index. The current results are inconclusive.

9. SECTION II: CONCLUSIONS

The beams with the “brick-and-mortar” architecture greatly outperformed the control specimens in observed peak load, CMOD, area under the load vs. CMOD curve, and toughness index, both normalized and unadjusted. Therefore, the structure of the plastic allows the specimens to undergo plastic deformation and absorb more energy from the additional applied loads. Specimens with smaller plastic wall thicknesses observed load vs. CMOD curves with relatively higher peaks and wider shapes, which aided in their energy absorption.

Specimens with more %polymer were found to have higher energy dissipation and toughness index due to more plastic deformation in the polymer wall sections than in the brittle concrete. Many of these specimens could withstand very high deflections before failure, which would make them the most efficient for energy dissipation, of the specimens that were tested.

The toughness index should be recalculated using more accurate date points that designate the completion of a linear load vs. CMOD curve and enter plastic deformations in the beam. The current toughness index results are inconclusive and potentially skewed in favor of the beams that deformed indefinitely.

10. SECTION II: FUTURE WORK

Based on the results of the testing from this project, there are several suggestions and recommendations for improving these methods for future work and analysis.

- Further analysis should be performed on the test specimens to determine their effect moment capacity at peak load. The transform method should be used which would substitute the plastic "mortar" with an equivalent volume of the cement paste.
- More test specimens should be developed with varying plastic thicknesses and number of blocks to determine the most efficient 3D-printed design for maximizing energy dissipation.
- To determine the individual contribution of the polymer itself, solid 3"x3"x8" 3D-printed plastic beams with the 0.1"x0.25" notch should be tested. This would better determine when the plastic is working independently from the concrete and not compositely. Failure would then be observed when the cement paste no longer contributes to the overall strength or deflection of the member.
- The "brick-and-mortar" architecture should be explored in all three dimensions, rather than the extruded 2D plane in these tests performed. This could potentially increase the observed energy dissipation and strength of the beam, but the constructability of the concrete bricks would be much more difficult, if the same casting procedures of this thesis were followed.

REFERENCES

1. Hoff, G. C. (1975). *A Concept for Rapid Repair of Bomb-Damaged Runways Using Regulated-Set Cement. Final Technical Report C-75-2.*

2. Barna, L. A., Tingle, J. S., & McCaffrey, P. S. (2010). Laboratory and Field Evaluation of Rapid Setting Cementitious Materials for Large Crater Repair. ERDC TR 10-4. In *ERDC TR* (Vol. 10, Issue 4). https://doi.org/https://hdl.handle.net/11681/8467

3. Biswas, S. K., Sano, H., Shams, M. I., & Yano, H. (2017). Three-Dimensional-Moldable Nanofiber-Reinforced Transparent Composites with a Hierarchically Self-Assembled "Reverse" Nacre-like Architecture. *ACS Applied Materials & Interfaces*, *9*(35), 30177–30184. https://doi.org/10.1021/acsami.7b09390

4. Sarikaya, M. (1994). An introduction to biomimetics: a structural viewpoint. *Microscopy Research and Technique*, *27*(5), 360–375. https://doi.org/10.1002/jemt.1070270503

5. Meyers, M. A., Chen, P.-Y., Lin, A. Y.-M., & Seki, Y. (2008). Biological materials: Structure and mechanical properties. *Progress in Materials Science*, *53*(1), 1–206. https://doi.org/https://doi.org/10.1016/j.pmatsci.2007.05.002

6. Barthelat, F., & Rabiei, R. (2011). Toughness amplification in natural composites. *Journal of the Mechanics and Physics of Solids*, *59*(4), 829–840. https://doi.org/https://doi.org/10.1016/j.jmps.2011.01.001

7. Katzer, J., & Szatkiewicz, T. (2019). Properties of concrete elements with 3-D printed formworks which substitute steel reinforcement. *Construction and Building Materials*, *210*, 157–161. https://doi.org/https://doi.org/10.1016/j.conbuildmat.2019.03.204

8. Ohama, Y. (2008). 12 - Polymer concrete. In S. Mindess (Ed.), *Developments in the Formulation and Reinforcement of Concrete* (pp. 256–269). Woodhead Publishing. https://doi.org/https://doi.org/10.1533/9781845694685.256

9. Fowler, D. W. (1999). Polymers in concrete: a vision for the 21st century. *Cement and Concrete Composites*, *21*(5–6), 449–452.

10. Frigione, M. (2013). 16 - Concrete with polymers. In F. Pacheco-Torgal, S. Jalali, J. Labrincha, & V. M. John (Eds.), *Eco-Efficient Concrete* (pp. 386–436). Woodhead Publishing. https://doi.org/https://doi.org/10.1533/9780857098993.3.386

11. Fowler, D. W. (2009). 7 - Repair materials for concrete structures. In N. Delatte (Ed.), *Failure, Distress and Repair of Concrete Structures* (pp. 194–207). Woodhead Publishing. https://doi.org/https://doi.org/10.1533/9781845697037.2.194

12. Kim, D. H. (1995). *Composite Structures for Civil and Architectural Engineering* (1st ed.). E & FN Spon. https://doi.org/https://doi.org/10.4324/9780203474969

13. Barbuta, M., Taranu, N., & Harja, M. (2009). Wastes used in obtaining polymer composite. *Environmental Engineering and Management Journal*, *8*(5), 1145–1150.

14. Barbuta, M., Harja, M., & Baran, I. (2010). Comparison of mechanical properties for polymer concrete with different types of filler. *Journal of Materials in Civil Engineering*, *22*(7), 696–

701.

15. Vipulanandan, C., & Dharmarajan, N. (1987). Flexural behavior of polyester polymer concrete. *Cement and Concrete Research*, *17*(2), 219–230. https://doi.org/https://doi.org/10.1016/0008-8846(87)90105-0

16. Jo, B.-W., Park, S.-K., & Park, J.-C. (2008). Mechanical properties of polymer concrete made with recycled PET and recycled concrete aggregates. *Construction and Building Materials*, *22*(12), 2281–2291. https://doi.org/https://doi.org/10.1016/j.conbuildmat.2007.10.009

17. Wongpa, J., Kiattikomol, K., Jaturapitakkul, C., & Chindaprasirt, P. (2010). Compressive strength, modulus of elasticity, and water permeability of inorganic polymer concrete. *Materials & Design*, *31*(10), 4748–4754. https://doi.org/https://doi.org/10.1016/j.matdes.2010.05.012

18. Bedi, R., Chandra, R., & Singh, S. P. (2013). Mechanical Properties of Polymer Concrete. *Journal of Composites*, *2013*, 948745. https://doi.org/10.1155/2013/948745

19. Abdel-Fattah, H., & El-Hawary, M. M. (1999). Flexural behavior of polymer concrete. *Construction and Building Materials*, *13*(5), 253–262.

20. Kobayashi, K., Ohama, Y., & Ito, T. (1974). Fatigue properties of resin concrete under repeated compression loads. *Seisan Kenkyu*, *26*(3), 116–118.

21. Rebeiz, K. S. (1996). Precast use of polymer concrete using unsaturated polyester resin based on recycled PET waste. *Construction and Building Materials*, *10*(3), 215–220. https://doi.org/https://doi.org/10.1016/0950-0618(95)00088-7

22. Farahat, M. S., Abdel-Azim, A.-A. A., & Abdel-Raowf, M. E. (2000). Modified unsaturated polyester resins synthesized from poly(ethylene terephthalate) waste, 1. Synthesis and curing characteristics. *Macromolecular Materials and Engineering*, *283*(1), 1–6. https://doi.org/https://doi.org/10.1002/1439-2054(20001101)283:1<1::AID-MAME1>3.0.CO;2-V

23. Rebeiz, K. S. (1995). Time-temperature properties of polymer concrete using recycled PET. *Cement and Concrete Composites*, *17*(2), 119–124.

24. Fontana, J. J., & Bartholomew, J. (1981). Use of concrete polymer materials in the transportation industry. *ST-69-2. Applications of Polymer Concrete*, 21–43.

25. Fowler, D. W. (1989). Future trends in polymer concrete. *Special Publication*, *116*, 129–144.

26. Guide to the use of polymers in concrete. (1986). *ACI*, *83*(5), 792–829.

27. Allahvirdizadeh, R., Rashetnia, R., Dousti, A., & Shekarchi, M. (2011). Application of polymer concrete in repair of concrete structures: A literature review. *Concrete Solutions*, 435–444.

28. Goli, N., & S., H. R. (2010). Improved Repair of Concrete Structures Using Polymer Concrete Patch and FRP Overlay. *Journal of Materials in Civil Engineering*, *22*(4), 314–322. https://doi.org/10.1061/(ASCE)MT.1943-5533.0000020

29. Greene, J., Iyer, S., Hammons, M., & Mellerski, R. (2007). *Airfield Damage Repair (ADR);*

Polymer Repair of Airfields Summary of Research. 30.

30. Jung, K.-C., Roh, I.-T., & Chang, S.-H. (2014). Evaluation of mechanical properties of polymer concretes for the rapid repair of runways. *Composites Part B: Engineering*, *58*, 352–360.

31. McNerney, M. T., Ballentine, G. D., Rollings, R. S., & Pizzuto, J. S. (1978). *An Investigation Into tho Use of Polymer-Concrete for Rapid Repair of Airfield Pavements. CEEDOTR-78-10*. https://doi.org/https://apps.dtic.mil/dtic/tr/fulltext/u2/a059121.pdf

32. Webster, R. P., Fontana, J. J., & Kukacka, L. E. (1978). *Rapid patching of concrete using polymer concrete*.

33. Wegst, U. G. K., Bai, H., Saiz, E., Tomsia, A. P., & Ritchie, R. O. (2015). Bioinspired structural materials. *Nature Materials*, *14*(1), 23–36. https://doi.org/10.1038/nmat4089

34. Askarinejad, S., & Rahbar, N. (2018). Mechanics of bioinspired lamellar structured ceramic/polymer composites: Experiments and models. *International Journal of Plasticity*, *107*, 122–149. https://doi.org/https://doi.org/10.1016/j.ijplas.2018.04.001

35. Gu, G. X., Libonati, F., Wettermark, S. D., & Buehler, M. J. (2017). Printing nature: Unraveling the role of nacre's mineral bridges. *Journal of the Mechanical Behavior of Biomedical Materials*, *76*, 135–144. https://doi.org/10.1016/j.jmbbm.2017.05.007

36. Barthelat, F., Tang, H., Zavattieri, P. D., Li, C.-M., & Espinosa, H. D. (2007). On the mechanics of mother-of-pearl: A key feature in the material hierarchical structure. *Journal of the Mechanics and Physics of Solids*, *55*(2), 306–337. https://doi.org/https://doi.org/10.1016/j.jmps.2006.07.007

37. Mayer, G. (2006). New Classes of Tough Composite Materials — Lessons from Natural Rigid Biological Systems. *Materials Science and Engineering: C*, *26*, 1261–1268. https://doi.org/10.1016/j.msec.2005.08.031

38. Bentur, A., & Mindess, S. (2007). *Fibre reinforced cementitious composites*. Taylor & Francis.

39. Pan, B. (2018). Digital image correlation for surface deformation measurement: Historical developments, recent advances and future goals. *Measurement Science and Technology*, *29*, 82001. https://doi.org/10.1088/1361-6501/aac55b

40. Hamrat, M., Boulekbache, B., Chemrouk, M., & Amziane, S. (2016). Flexural cracking behavior of normal strength, high strength and high strength fiber concrete beams, using Digital Image Correlation technique. *Construction and Building Materials*, *106*, 678–692. https://doi.org/10.1016/j.conbuildmat.2015.12.166

41. Pan, B., Wang, Z., & Lu, Z. (2010). Genuine full-field deformation measurement of an object with complex shape using reliability-guided digital image correlation. *Optics Express*, *18*(2), 1011—1023. https://doi.org/10.1364/oe.18.001011

42. Krawczyk, Ł., Gołdyn, M., & Urban, T. (2019). Digital Image Correlation Systems in the Experimental Investigations: Capabilities and Limitations. *Archives of Civil Engineering*, *65*, 171–180. https://doi.org/10.2478/ace-2019-0012

43. *C33/C33M-18 Standard Specification for Concrete Aggregates*. (2018). ASTM International.

https://doi.org/10.1520/C0033_C0033M-18

44. *C127-15 Standard Test Method for Relative Density (Specific Gravity) and Absorption of Coarse Aggregate*. (2015). ASTM International. https://doi.org/10.1520/C0127-15

45. *C128-15 Standard Test Method for Relative Density (Specific Gravity) and Absorption of Fine Aggregate*. (2015). ASTM International. https://doi.org/10.1520/C0128-15

46. Barthel, H., Rösch, L., & Weis, J. (1995). Fumed Silica - Production, Properties, and Applications. In *Organosilicon Chemistry II* (pp. 761–778). https://doi.org/https://doi.org/10.1002/9783527619894.ch91

47. Mamlouk, M. S., & Zaniewski, J. P. (2011). *Materials for Civil and Construction Engineers* (3rd ed.). Pearson.

48. Wang, W., Martin, J. C., Zhang, N., Ma, C., Han, A., & Sun, L. (2011). Harvesting silica nanoparticles from rice husks. *Journal of Nanoparticle Research*, *13*(12), 6981–6990. https://doi.org/10.1007/s11051-011-0609-3

49. Flörke, O. W., Graetsch, H. A., Brunk, F., Benda, L., Paschen, S., Bergna, H. E., Roberts, W. O., Welsh, W. A., Libanati, C., Ettlinger, M., Kerner, D., Maier, M., Meon, W., Schmoll, R., Gies, H., & Schiffmann, D. (2008). Silica. In *Ullmann's Encyclopedia of Industrial Chemistry*. https://doi.org/https://doi.org/10.1002/14356007.a23_583.pub3

50. Priddy, L. P., Bell, H. P., Edwards, L., Carruth, W. D., & Rowland., J. F. (2016). *Evaluation of the structural performance of Rapid Set Concrete Mix®. ERDC/GSL TR-16-20.* https://doi.org/https://hdl.handle.net/11681/20287

51. Bell, H. P., Cox, B. C., Edwards, L., Garcia, L. I., Hoffman, N. R., Mejías, M., & Johnson, J. L. (2019). *Rapid airfield damage recovery technology integration experiment. ERDC TR-19-8.* https://doi.org/https://hdl.handle.net/11681/33049

52. *C150/C150M-20 Standard Specification for Portland Cement*. (2020). ASTM International. https://doi.org/10.1520/C0150_C0150M-20

53. *C31/C31M-19a Standard Practice for Making and Curing Concrete Test Specimens in the Field*. (2019). ASTM International. https://doi.org/10.1520/C0031_C0031M-19A

54. *C39/C39M-20 Standard Test Method for Compressive Strength of Cylindrical Concrete Specimens*. (2020). ASTM International. https://doi.org/10.1520/C0039_C0039M-20

55. *C109/C109M-20b Standard Test Method for Compressive Strength of Hydraulic Cement Mortars (Using 2-in. or [50 mm] Cube Specimens)*. (2020). ASTM International. https://doi.org/10.1520/C0109_C0109M-20B

56. *C579-18 Standard Test Methods for Compressive Strength of Chemical-Resistant Mortars, Grouts, Monolithic Surfacings, and Polymer Concretes*. (2018). ASTM International. https://doi.org/10.1520/CO579-18

57. Sigvaldason, O. T. (1966). The influence of testing machine characteristics upon the cube and cylinder strength of concrete. *Magazine of Concrete Research*, *18*(57), 197–206. https://doi.org/10.1680/macr.1966.18.57.197

58. Testing Protocol for Rapidsetting Rigid Repair Materials. TSPWG M 3-270-01.08-2. (2020). *Tri-Service Pavements Working Group Manual*. https://www.wbdg.org/FFC/DOD/STC/tspwg_m_3-270-01.08-2.pdf

59. Mindess, S., Young, J. F., & Darwin, D. (2003). *Concrete* (2nd ed.). Prentice Hall.

60. *C293/C293M-16 Standard Test Method for Flexural Strength of Concrete (Using Simple Beam With Center-Point Loading)*. (2016). ASTM International. https://doi.org/10.1520/C0293_C0293M-16

61. *C78/C78M-18 Standard Test Method for Flexural Strength of Concrete (Using Simple Beam with Third-Point Loading)*. (2018). ASTM International. https://doi.org/10.1520/C0078_C0078M-18

62. *C882/C882M-20 Standard Test Method for Bond Strength of Epoxy-Resin Systems Used With Concrete By Slant Shear*. (2020). ASTM International. https://doi.org/10.1520/C0882_C0882M-20

63. Holmes, P. (2020). *Mechanics of Materials: Bending – Shear Stress » Mechanics of Slender Structures.* Boston University. https://www.bu.edu/moss/mechanics-of-materials-bending-shear-stress/

64. *C143/C143M-20 Standard Test Method for Slump of Hydraulic-Cement Concrete*. (2020). ASTM International. https://doi.org/10.1520/C0143_C0143M-20

65. *C469/C469M-14 Standard Test Method for Static Modulus of Elasticity and Poisson’s Ratio of Concrete in Compression*. (2014). ASTM International. https://doi.org/10.1520/C0469_C0469M-14

66. Humboldt. (n.d.). *Compressometers / Extensometers Product Manual*. 3.

67. *C531-18 Standard Test Method for Linear Shrinkage and Coefficient of Thermal Expansion of Chemical-Resistant Mortars, Grouts, Monolithic Surfacings, and Polymer Concretes*. (2018). ASTM International. https://doi.org/10.1520/C0531-18

68. Chung, Y., & Shin, H.-C. (2010). Characterization of the coefficient of thermal expansion and its effect on the performance of Portland cement concrete pavements. *Canadian Journal of Civil Engineering*, *38*(2), 175–183. https://doi.org/10.1139/L10-122

69. Federal Highway Administration Research and Technology. (2016). *Thermal Coefficient Of Portland Cement Concrete*. U.S. Department of Transportation. https://www.fhwa.dot.gov/publications/research/infrastructure/pavements/pccp/thermal.cfm

70. Kosmatka, S. H., & Wilson, M. L. (2011). *Design and Control of Concrete Mixtures* (15th ed.). Portland Cement Associate.

71. Yeon, K.-S., & Yeon, J.-H. (2012). Setting Shrinkage, Coefficient of Thermal Expansion, and Elastic Modulus of UP-MMA Based Polymer Concrete. *Journal of the Korea Concrete Institute*, *24*(4), 491–498. https://doi.org/https://doi.org/10.4334/jkci.2012.24.4.491

72. Jung, K.-C., Roh, I.-T., & Chang, S.-H. (2015). Thermal behavior and performance evaluation of epoxy-based polymer concretes containing silicone rubber for use as runway repair

materials. *Composite Structures*, *119*, 195–205. https://doi.org/https://doi.org/10.1016/j.compstruct.2014.08.038

73. *Rapid Set® Concrete Maintenance – General Purpose Repair & Resurfacing Specification*. (2020). https://www.ctscement.com/assets/doc/products/CONCRETE_MIX_SPEC_EN.pdf

74. *Products | CTS Cement*. (2020). CTScement.Com. https://www.ctscement.com/product/concrete-mix?c=PRODUCTS&t=

75. *Overview of materials for Polylactic Acid (PLA) Biopolymer*. (2020). Matweb.Com. http://www.matweb.com/search/DataSheet.aspx?MatGUID=ab96a4c0655c4018a8785ac4031b9278

76. *C309-19 Standard Specification for Liquid Membrane-Forming Compounds for Curing Concrete*. (2019). ASTM International. https://doi.org/10.1520/C0309-19

77. Hillerborg, A. (1985). The theoretical basis of a method to determine the fracture energyGFof concrete. *Materials and Structures*, *18*(4), 291–296. https://doi.org/10.1007/BF02472919

78. Barr, B. I. G., Liu, K., & Dowers, R. C. (1982). A toughness index to measure the energy absorption of fibre reinforced concrete. *International Journal of Cement Composites and Lightweight Concrete*, *4*(4), 221–227. https://doi.org/https://doi.org/10.1016/0262-5075(82)90025-2

APPENDIX A

Slump Test Pictures

17 wt.% Resin mixes:

Luna PC Phase I: 17wt.% Resin w/ #78 Dolomite and SAP 1

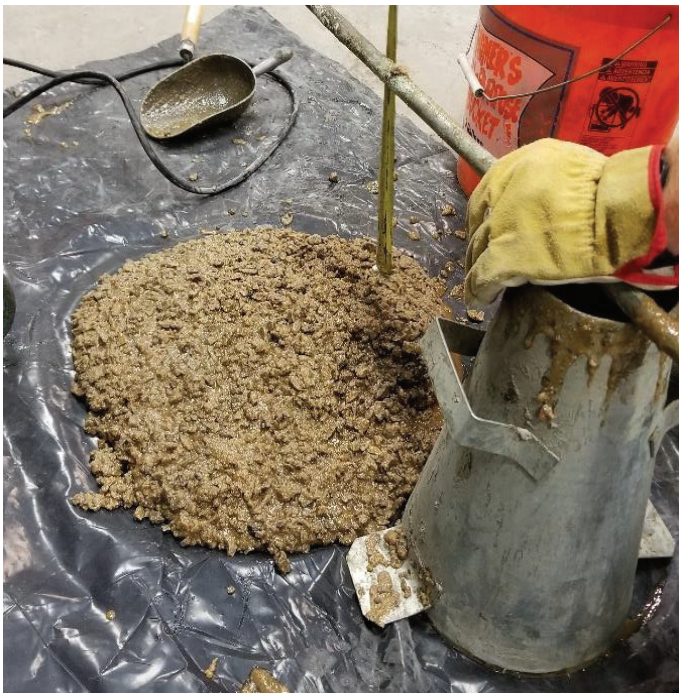

Luna PC Phase II: 17wt.% Resin w/ #68 Granite

Luna PC Phase II: 17wt.% Resin w/ #57 Dolomite

Luna PC Phase II: 17wt.% Resin w/ #68 Dolomite

10 wt.% Resin mixes:

Luna PC Phase II: 10wt.% Resin w/ #78 Dolomite

Luna PC Phase II: 10wt.% Resin w/ #68 Granite

Luna PC Phase II: 10wt.% Resin w/ #57 Dolomite

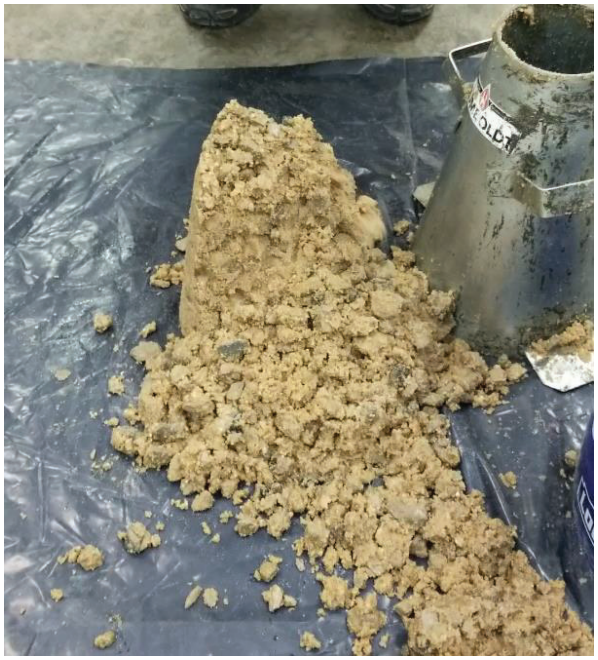

Luna PC Phase II: 10wt.% Resin w/ #68 Dolomite

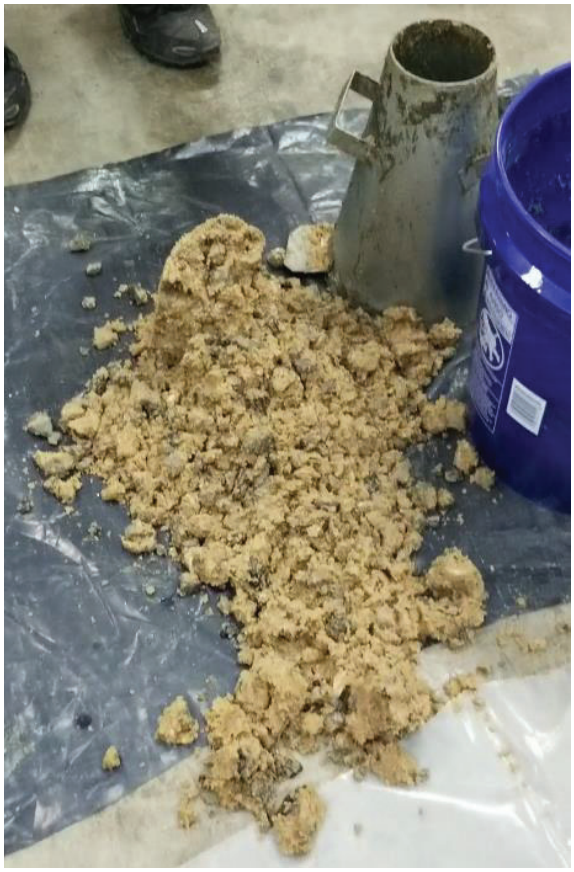

12 and 15 wt.% Resin mix:

Luna PC Phase II: 12wt.% Resin – Before Shear Failure

Luna PC Phase II: 12wt.% Resin – After Shear Failure

Luna PC Phase II: 15wt.% Resin

CTS Concrete mix:

CTS Concrete

Luna PC mixes with Various Silica Packages:

Luna PC Phase II: 15wt.% Resin w/ SAP 2

Luna PC Phase II: 17wt.% Resin w/ SAP 3

Luna PC Phase II: 17wt.% Resin w/ SAP 4

APPENDIX B

Modulus of Elasticity Trendline Data

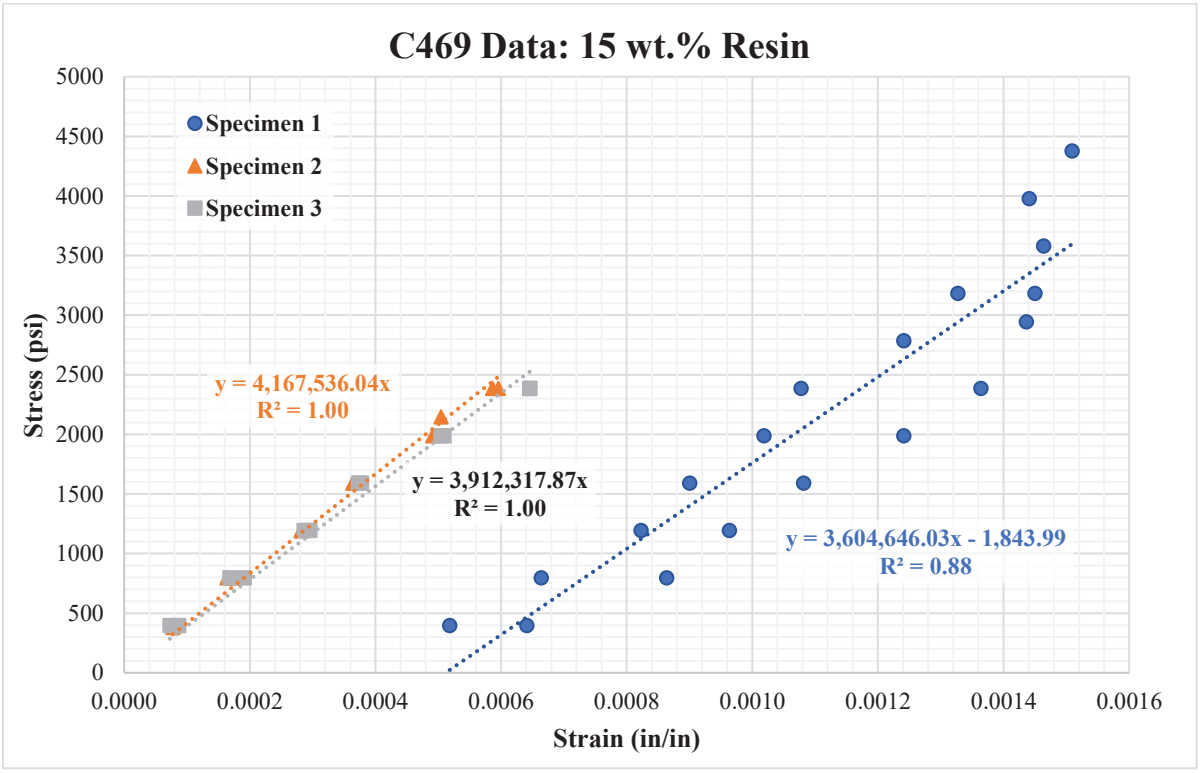

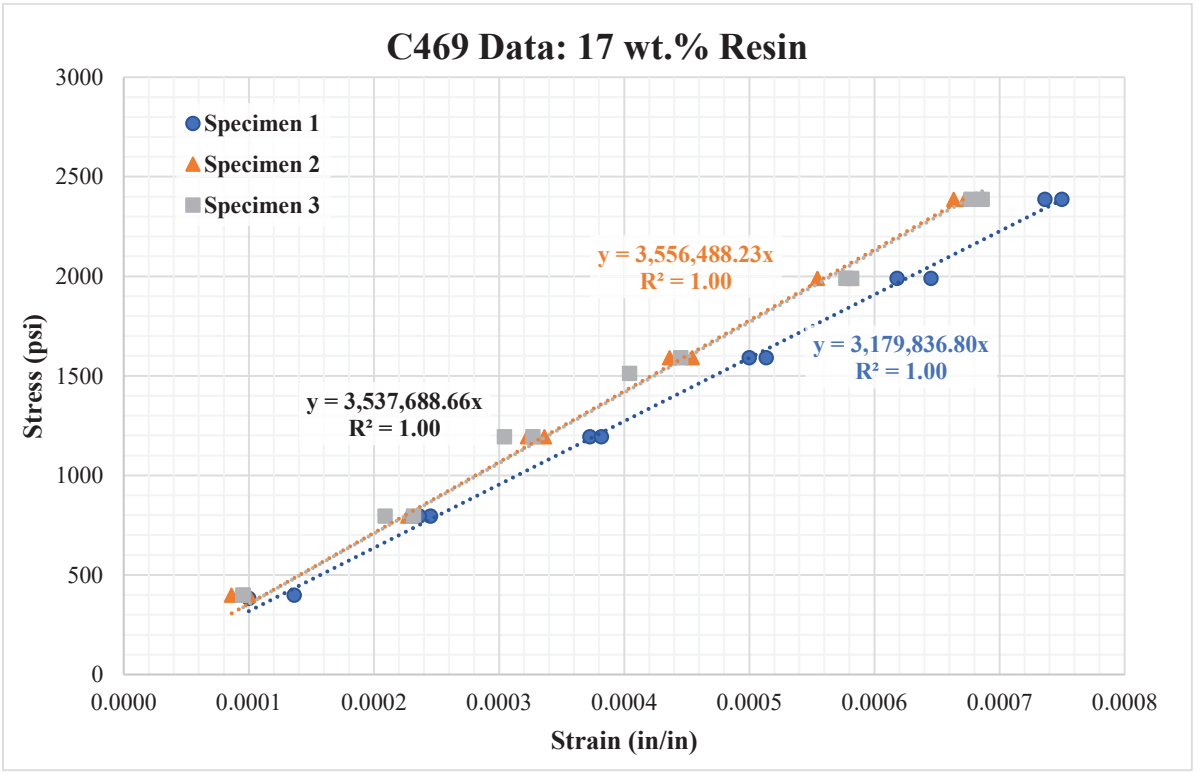

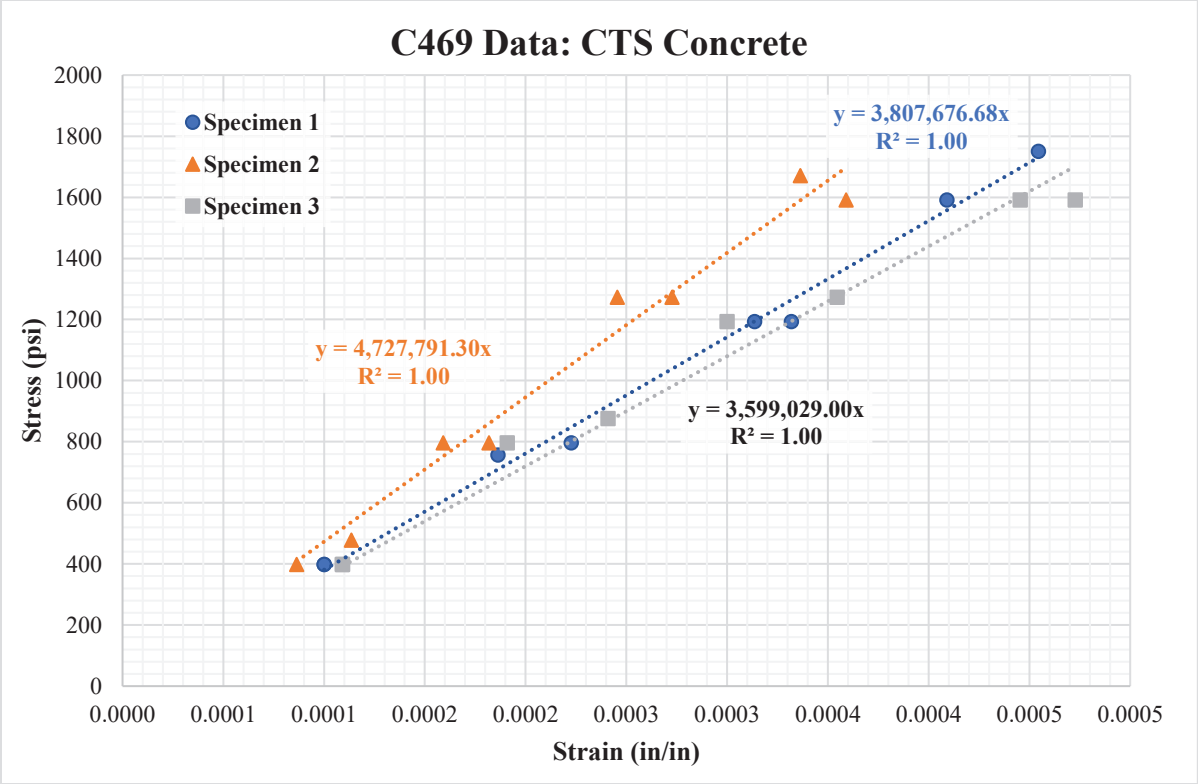

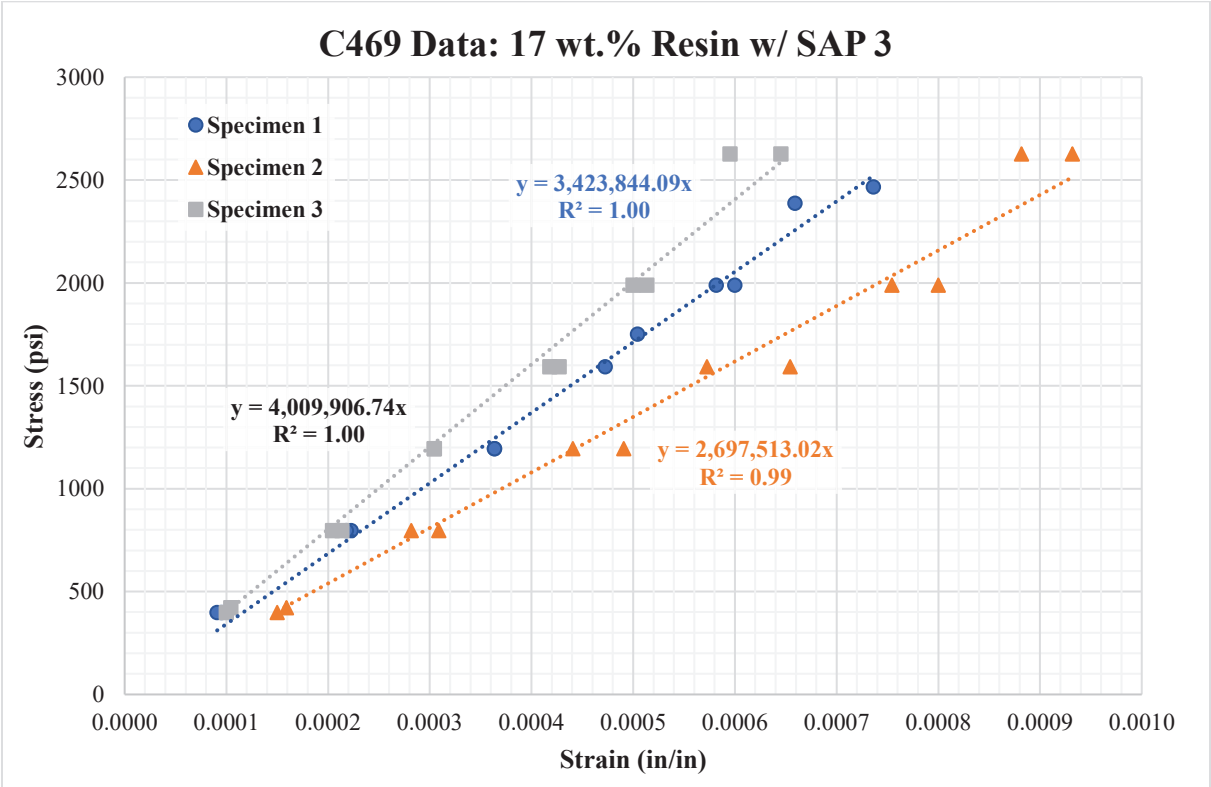

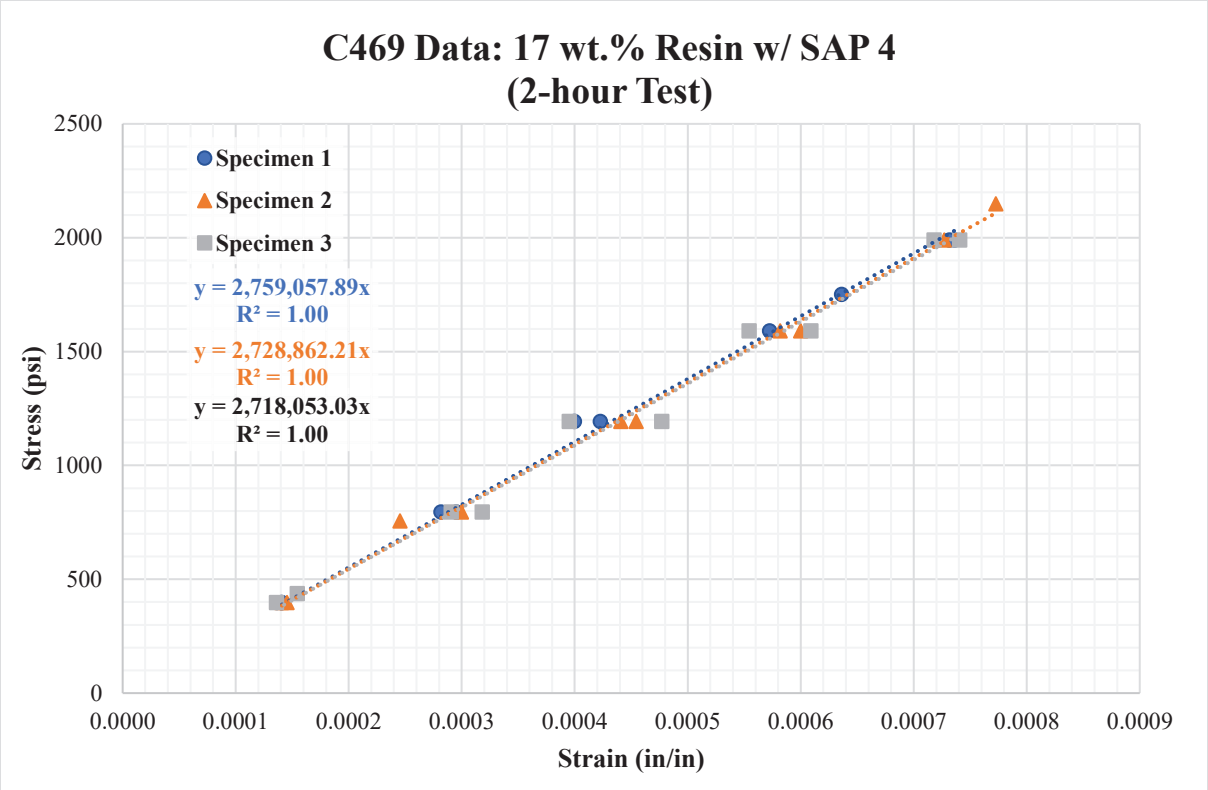

APPENDIX C

Coefficient of Thermal Expansion Raw Data

CTS Concrete

CTS Concrete

Specimen #	Temperature °F	Recorded Length in	Strain in/in	Strain mε	Strain in/in	Strain mε
1	73.9	11.8941	0.000589	0.589	0.000580	0.580
2	73.8	11.8505	0.000608	0.608	0.000599	0.599
3	73.9	11.8764	0.000397	0.397	0.000413	0.413
1	224.0	11.8921	0.000224	0.224	0.000412	0.412
2	221	11.8555	0.000930	0.930	0.001022	1.022
3	220.2	11.8819	0.000768	0.768	0.000876	0.876
1	1.2	11.8872	0.000000	0.000	0.000000	0.000
2	-1.6	11.8434	0.000000	0.000	0.000000	0.000
3	3.1	11.8715	0.000000	0.000	0.000000	0.000
1	145.7	11.9017	0.001248	1.248	0.001220	1.220
2	149	11.8534	0.000806	0.806	0.000844	0.844

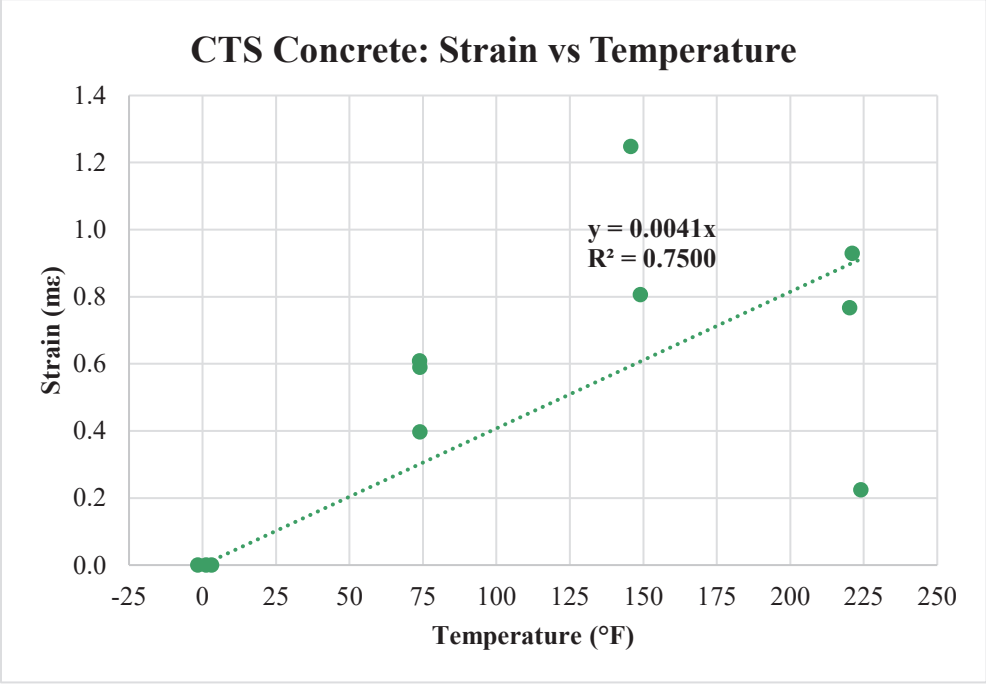

Luna PC Phase II: 17 wt.% Resin w/ SAP 3

17 wt.% Resin w/ SAP 3

Specimen #	Temperature °F	Recorded Length in	Strain in/in	Strain mε	Strain in/in	Strain mε
1	74.0	11.8359	0.000823	0.823	0.000786	0.786
2	74.4	11.8597	0.001066	1.066	0.000996	0.996
1	228.7	11.8591	0.002919	2.919	0.002748	2.748
2	228.1	11.9204	0.006824	6.824	0.006119	6.119
3	229.9	11.8585	0.003049	3.049	0.002858	2.858
1	-3.0	11.8266	0.000000	0.000	0.000000	0.000
2	-2.6	11.8479	0.000000	0.000	0.000000	0.000
3	0.2	11.8247	0.000000	0.000	0.000000	0.000
1	149.5	11.8427	0.001403	1.403	0.001361	1.361
2	149.3	11.8692	0.001909	1.909	0.001798	1.798
3	150.4	11.8467	0.001984	1.984	0.001861	1.861

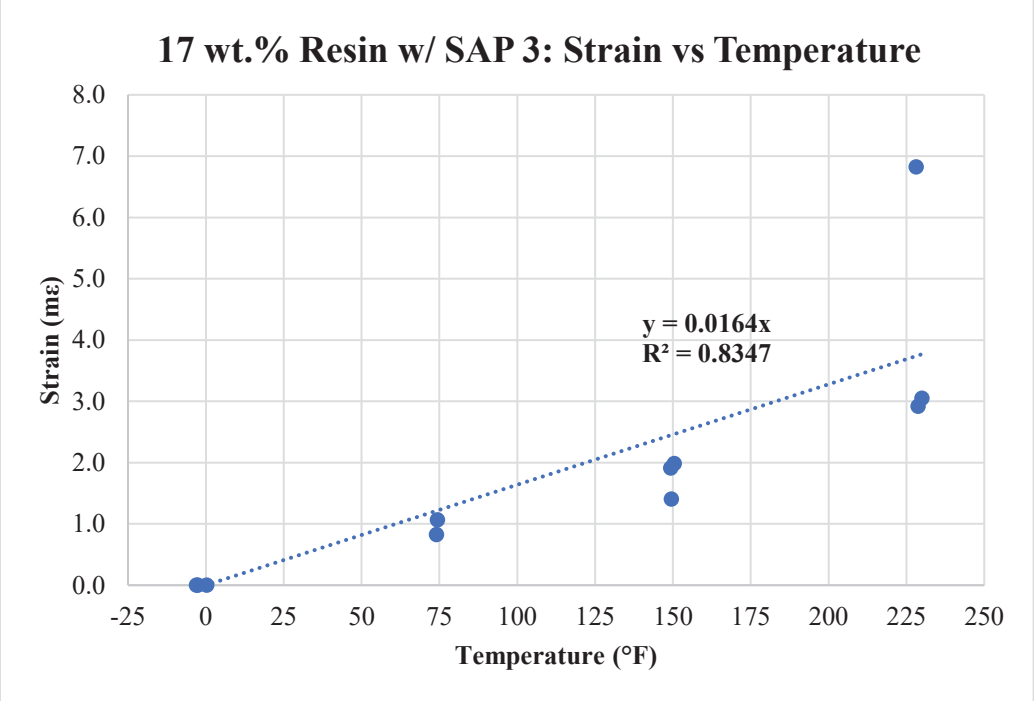

Luna PC Phase II: 17 wt.% Resin w/ SAP 4

17 wt.% Resin w/ SAP 4

Specimen #	Temperature °F	Recorded Length in	Strain in/in	Strain mε	Strain in/in	Strain mε
1	73.0	11.8581	0.001173	1.173	0.001081	1.081
2	72.9	11.8269	0.002207	2.207	0.001974	1.974
3	72.9	11.8616	0.001328	1.328	0.001215	1.215
1	229.0	11.8968	0.004779	4.779	0.004348	4.348
2	227.5	11.8574	0.005024	5.024	0.004558	4.558
3	228.6	11.8929	0.004210	4.210	0.003857	3.857
1	3.8	11.8453	0.000000	0.000	0.000000	0.000
2	2.3	11.8036	0.000000	0.000	0.000000	0.000
3	2.5	11.8472	0.000000	0.000	0.000000	0.000
1	151.2	11.8730	0.002541	2.541	0.002338	2.338
2	148.3	11.8369	0.003102	3.102	0.002821	2.821
3	149.4	11.8755	0.002599	2.599	0.002389	2.389

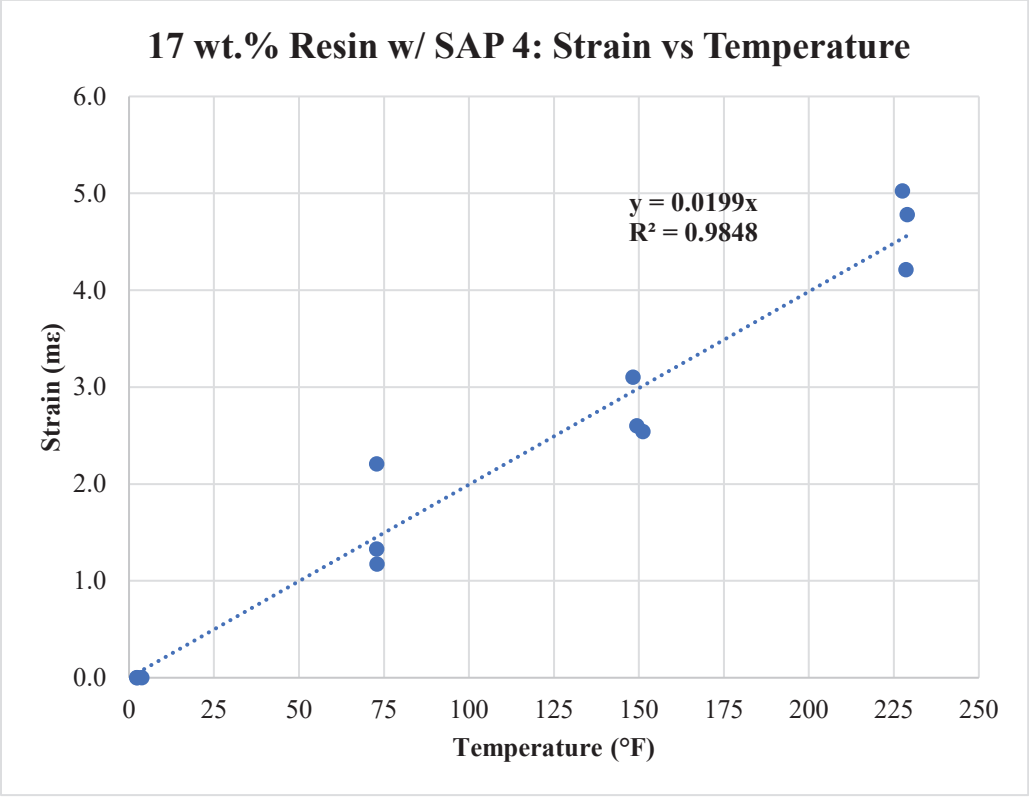

APPENDIX D

3D-Printed Plastic-Concrete Composite Beams

Control 1

Before Testing

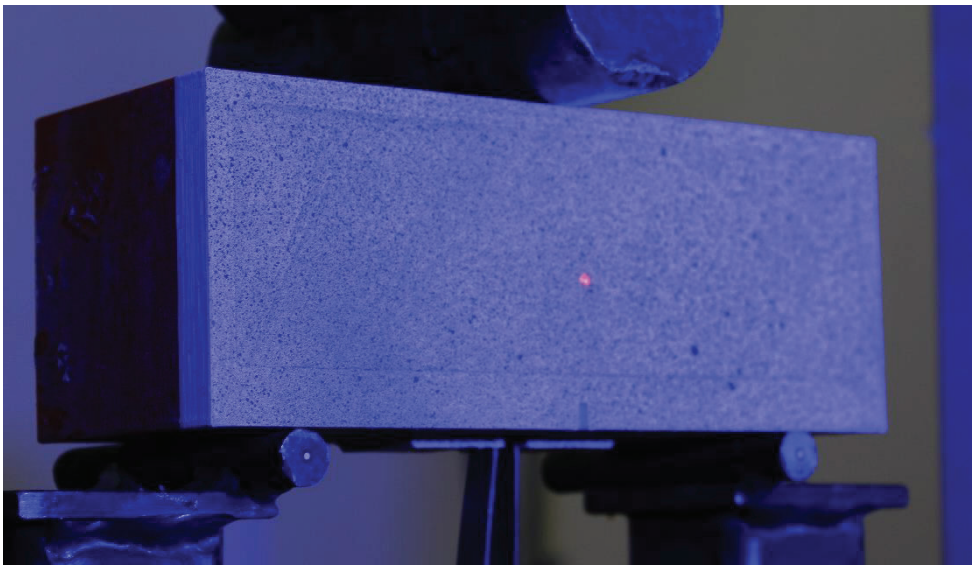

After Testing

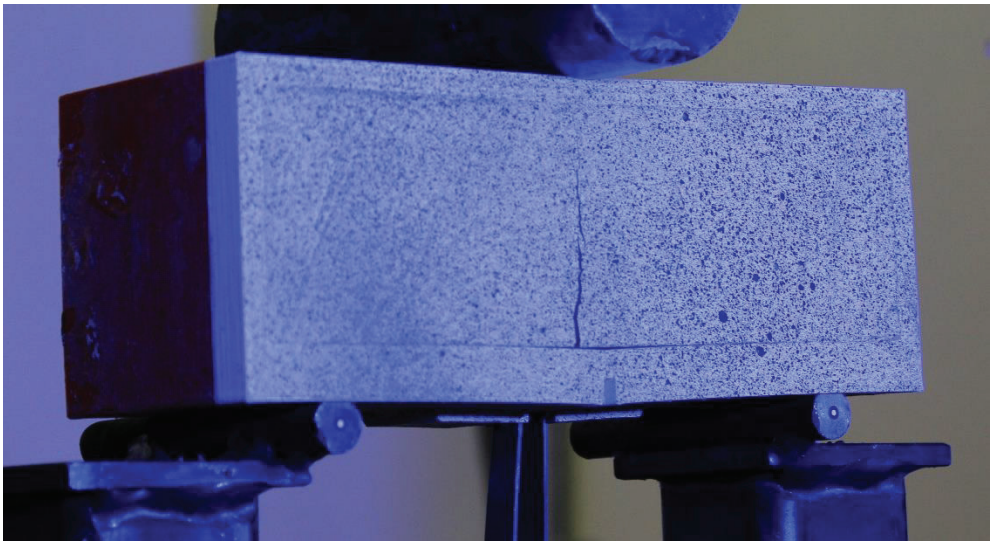

Control 2

After Testing

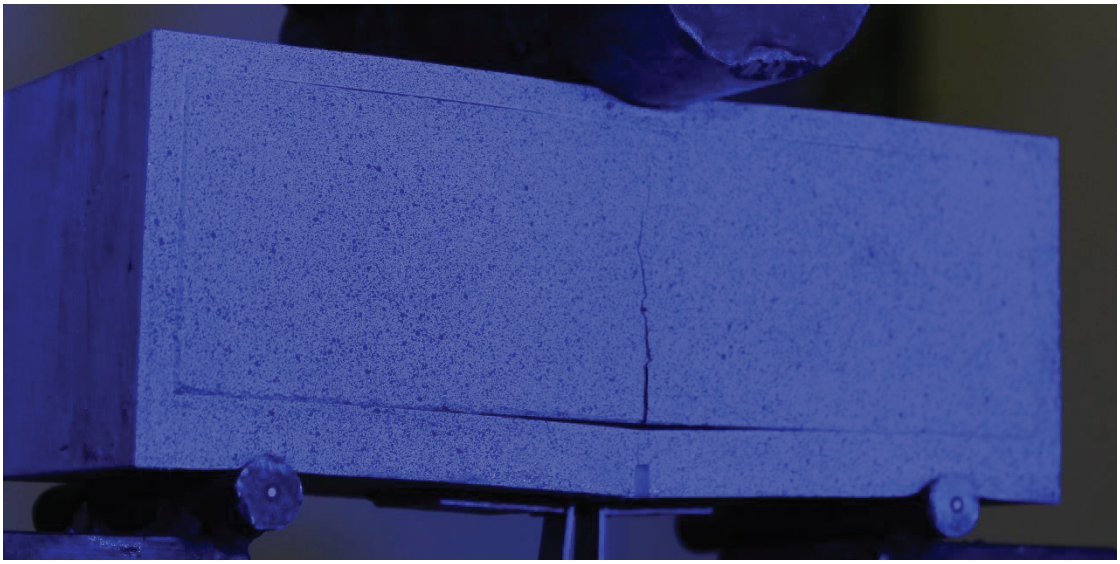

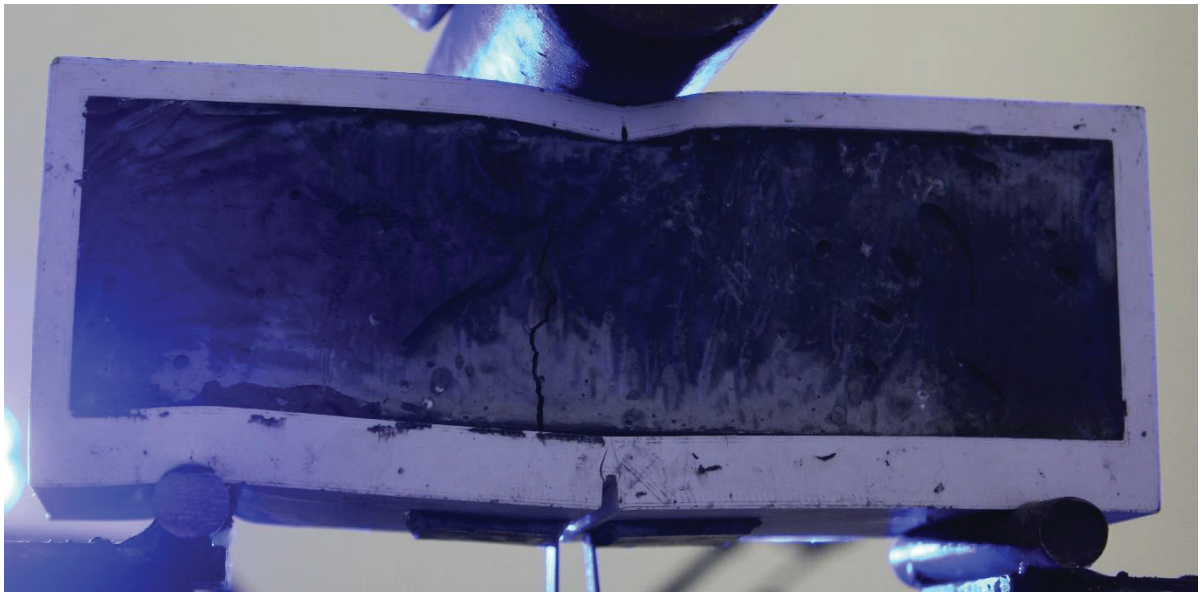

Control 3

Before Testing

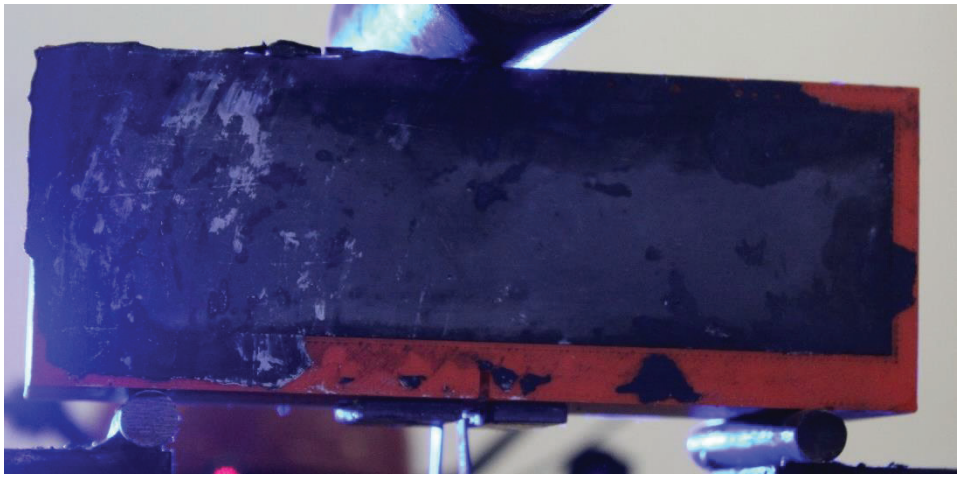

After Testing

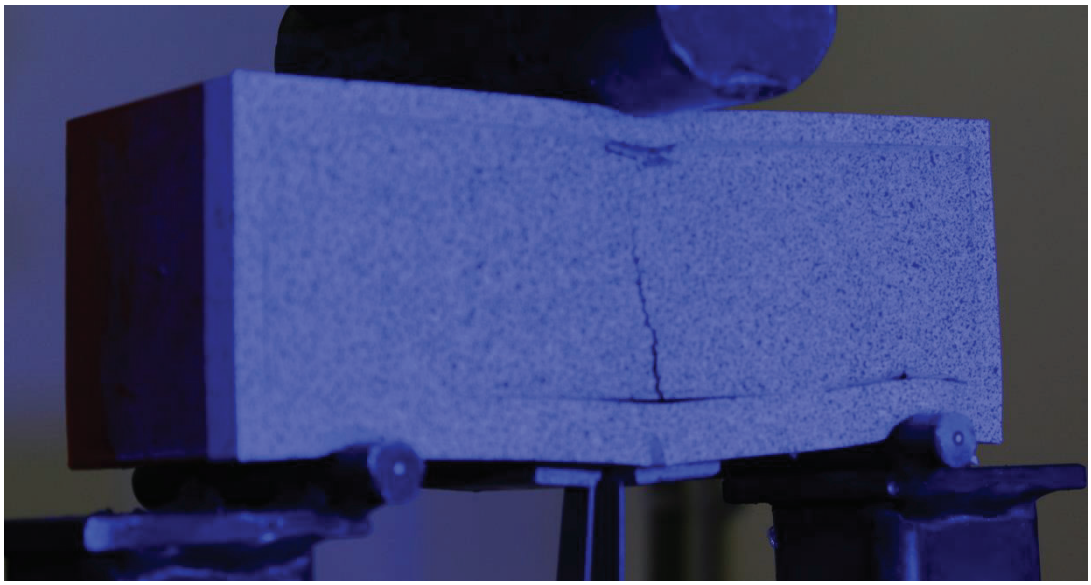

Control 4

After Testing

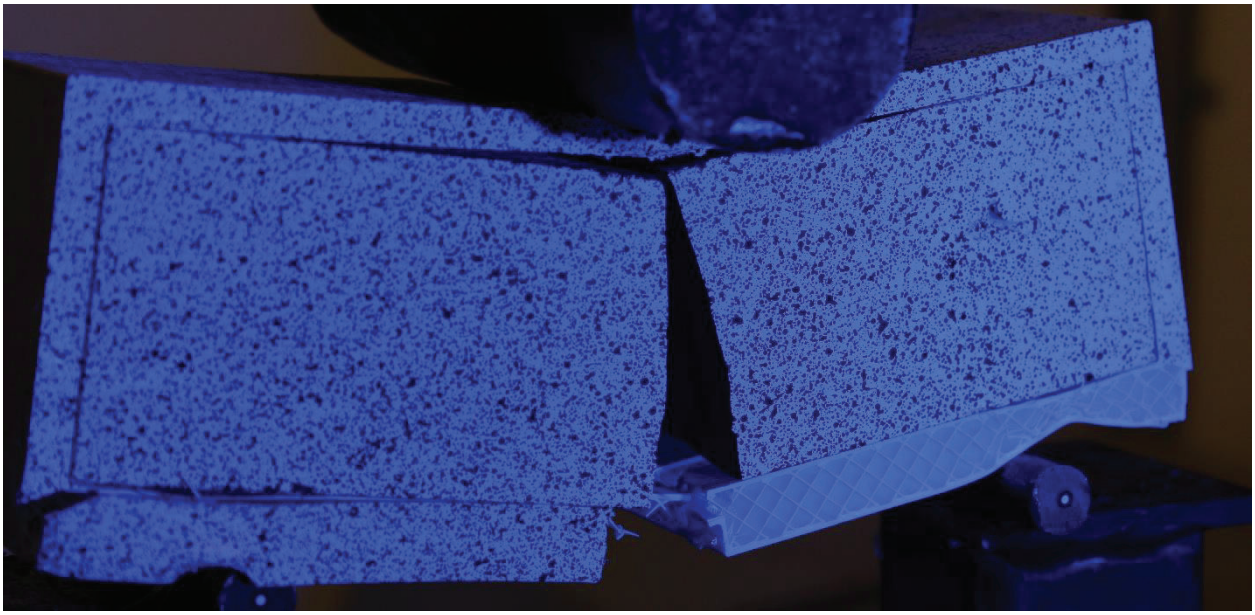

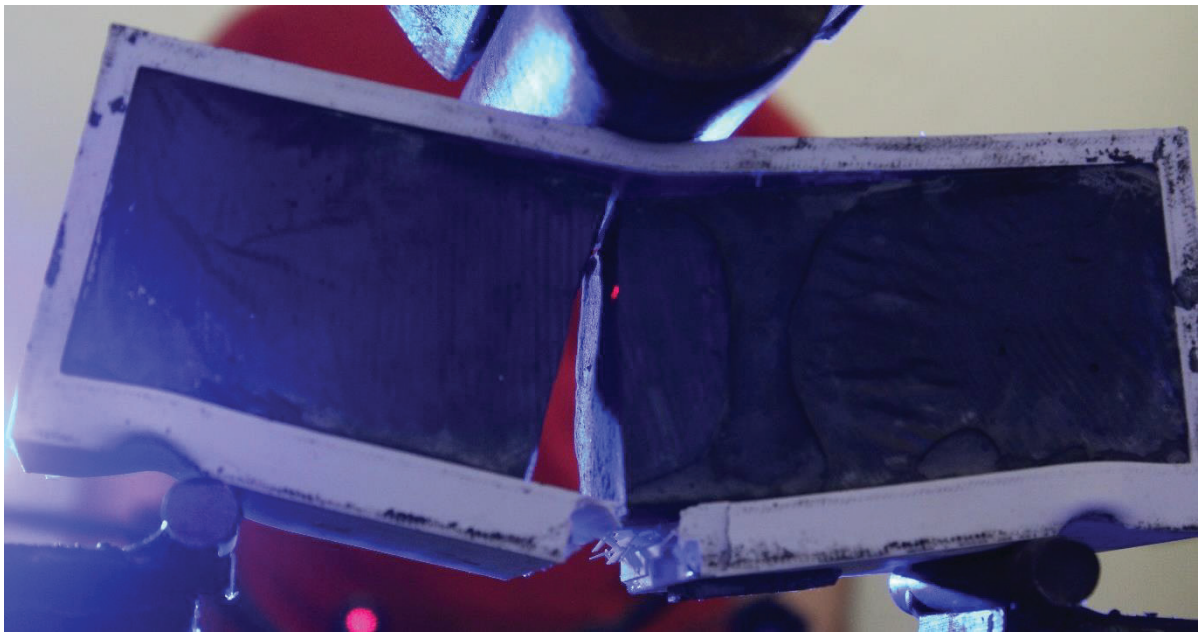

3R-10B-0.1T

Before Testing

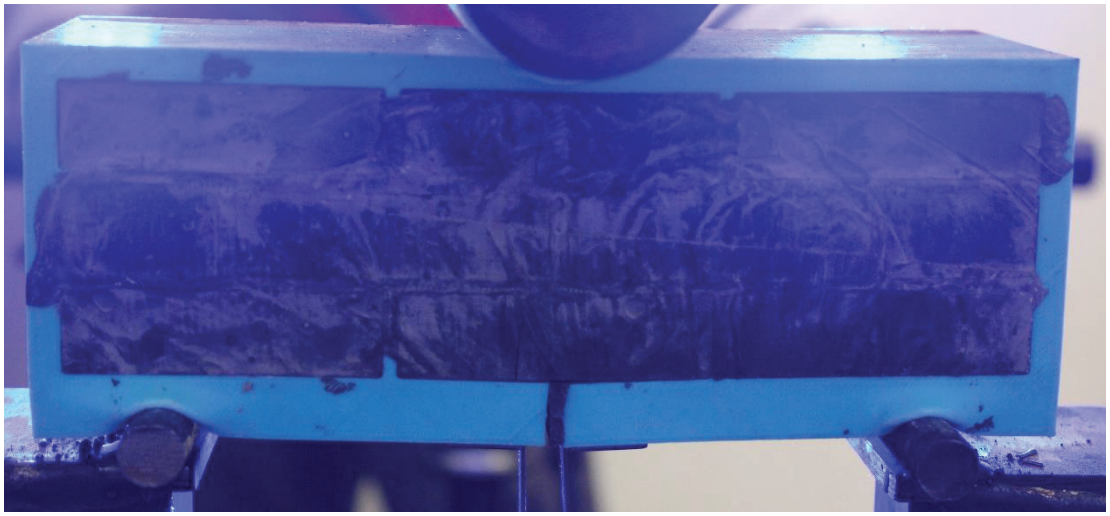

After Testing

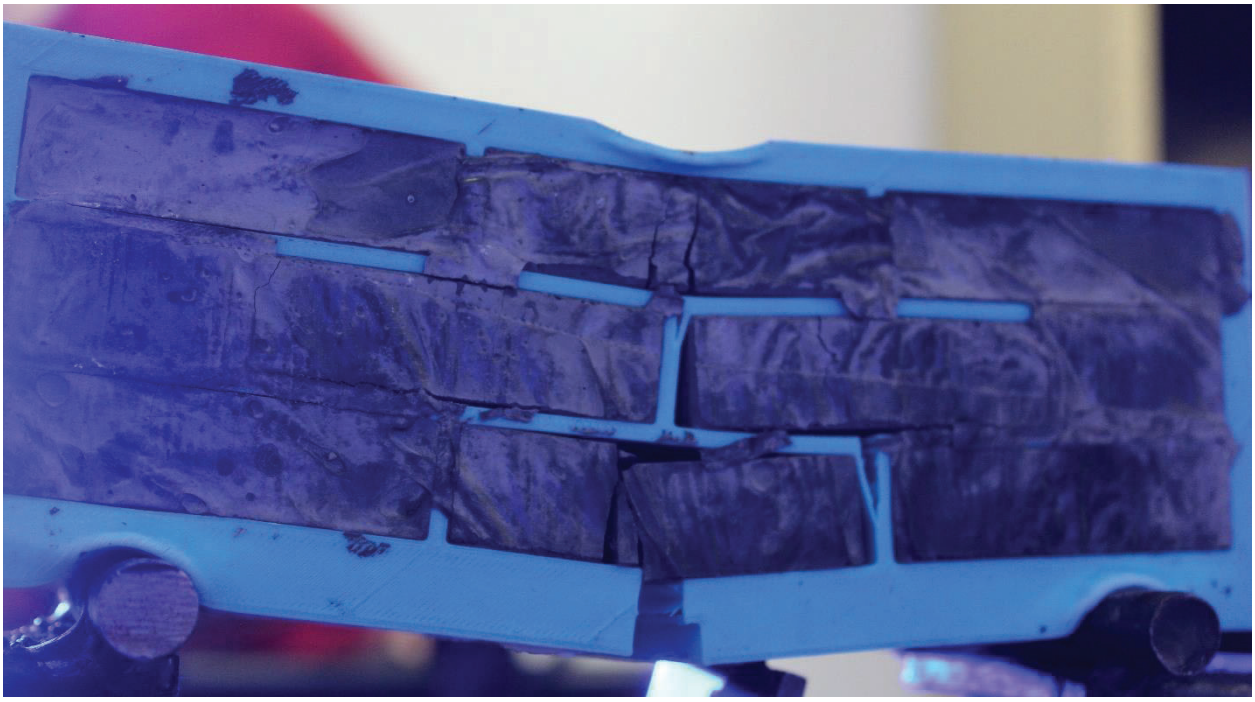

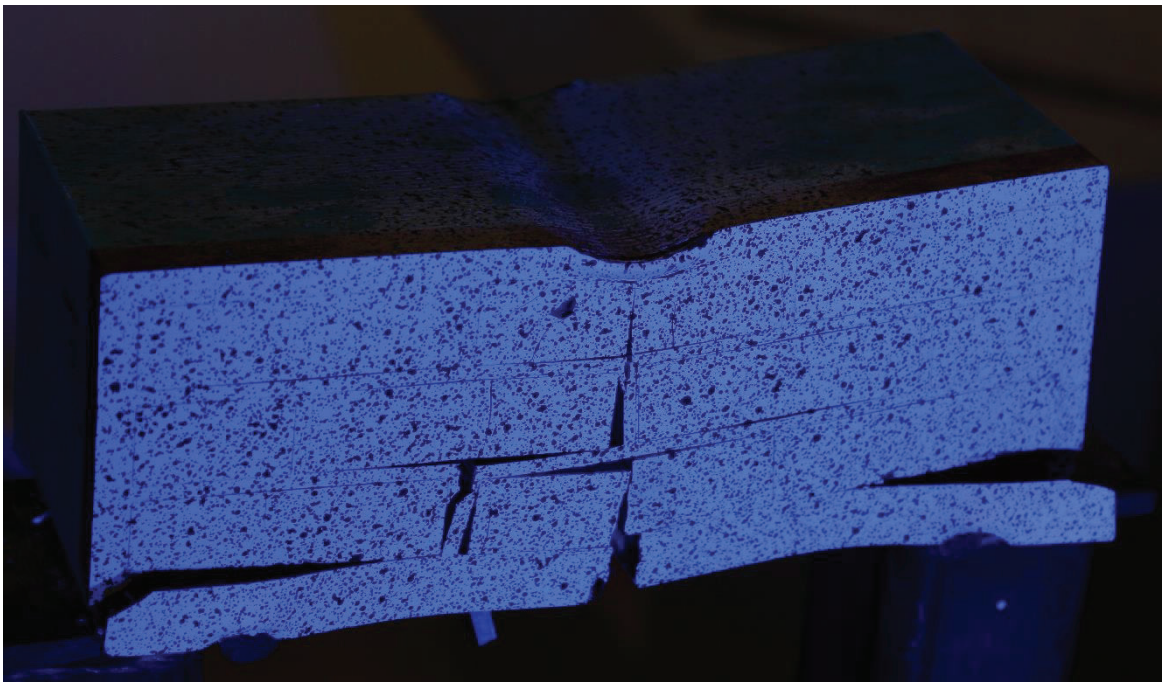

3R-10B-0.25T

After Testing

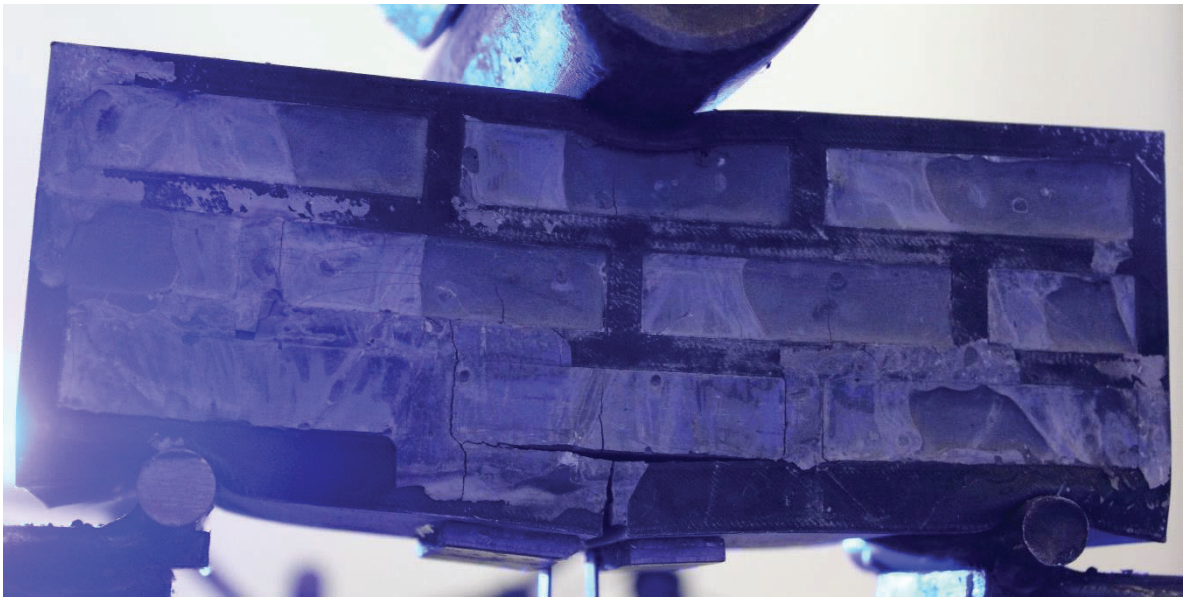

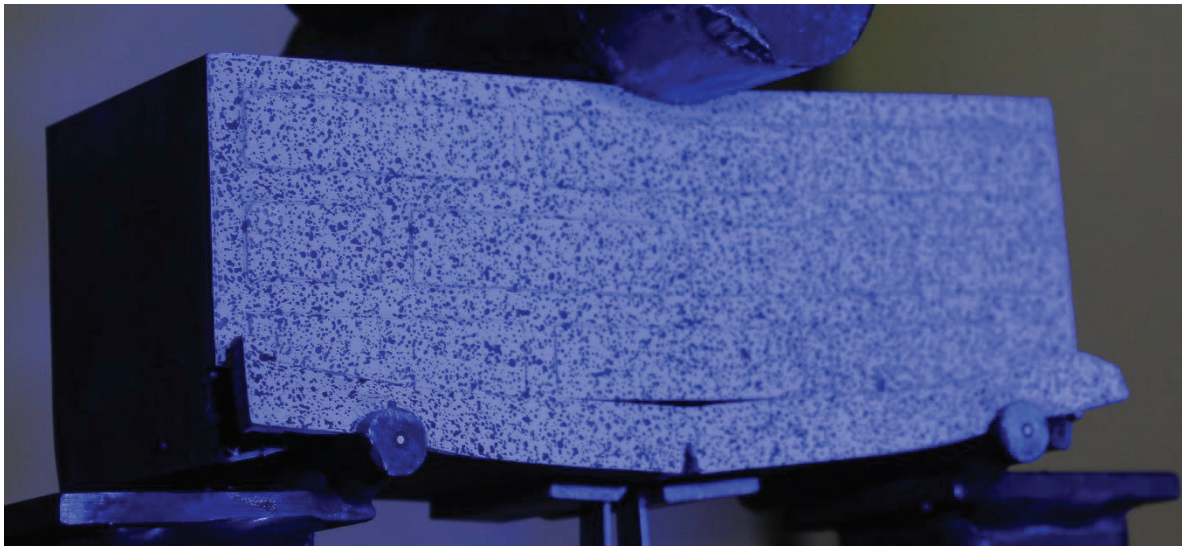

At Failure

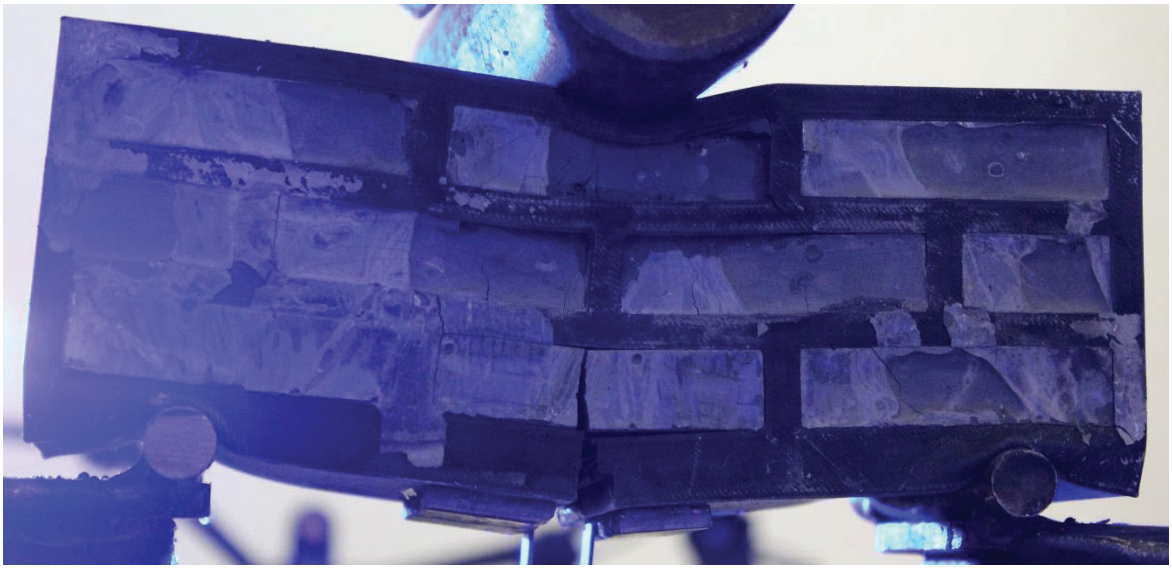

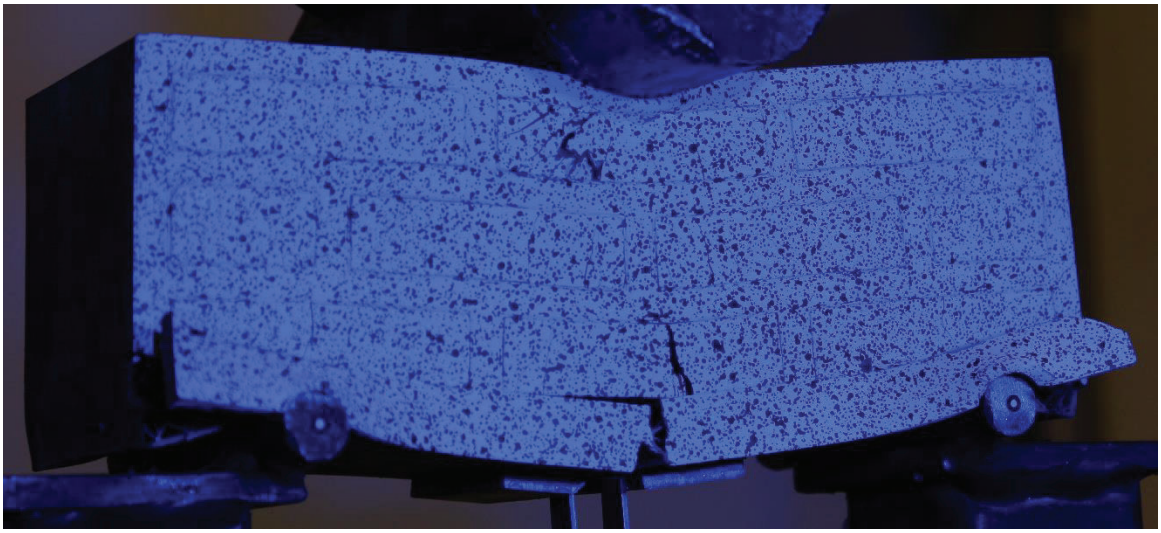

3R-16B-0.25T

After Testing

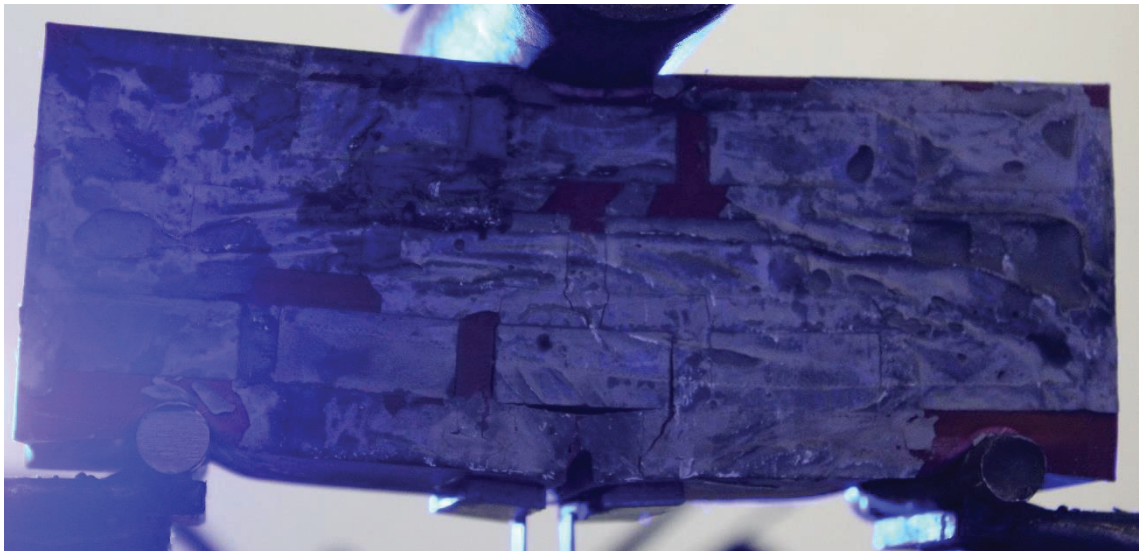

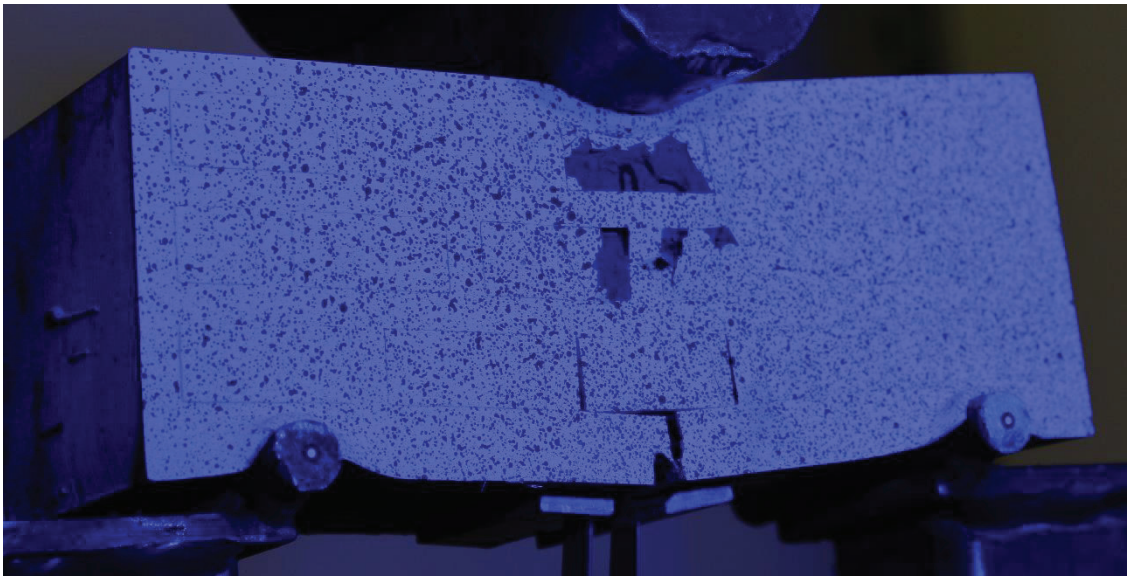

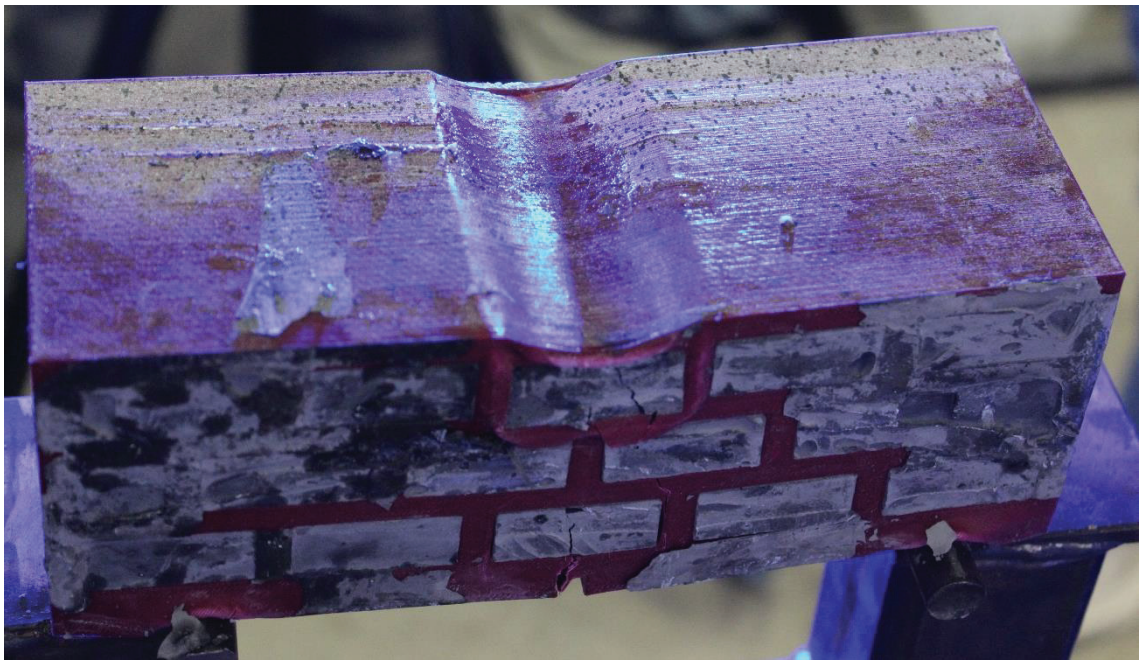

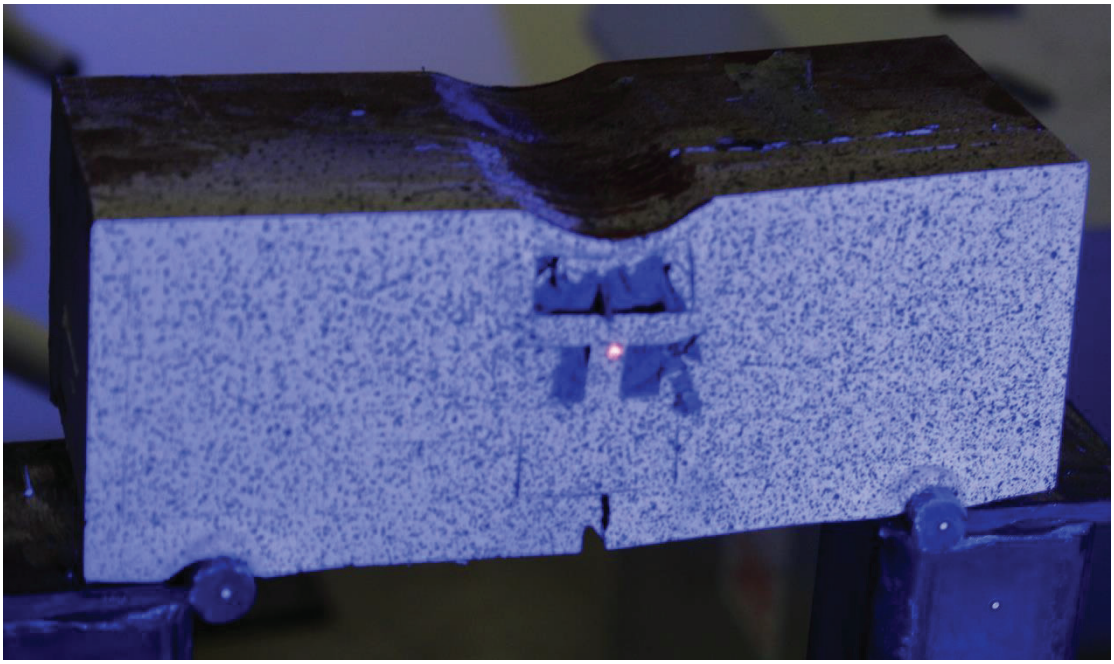

5R-17B-0.1T (1)

Before Testing

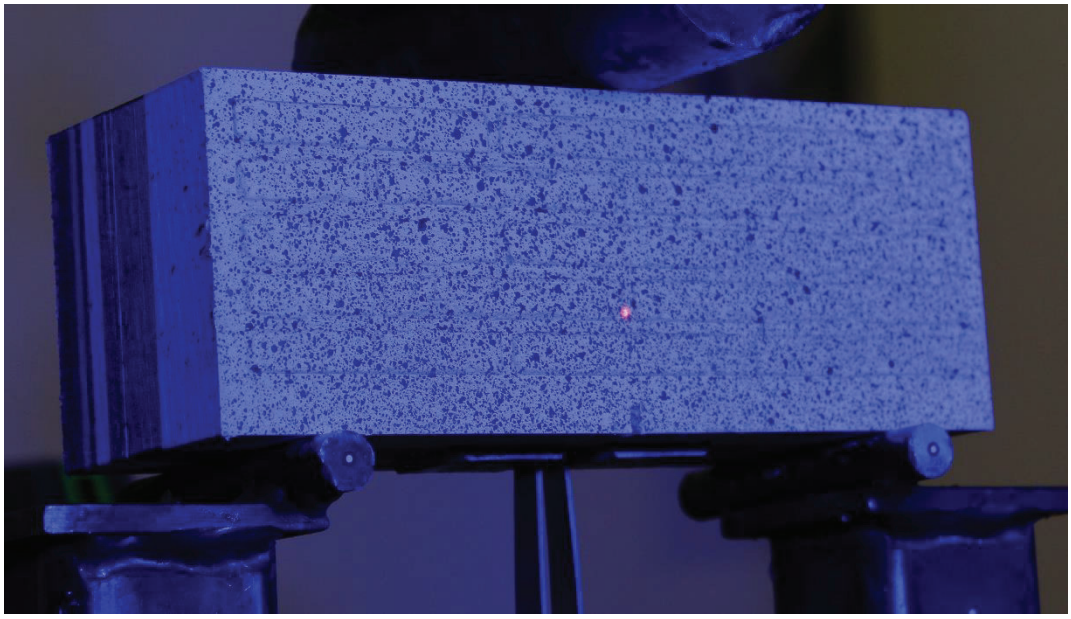

After Testing

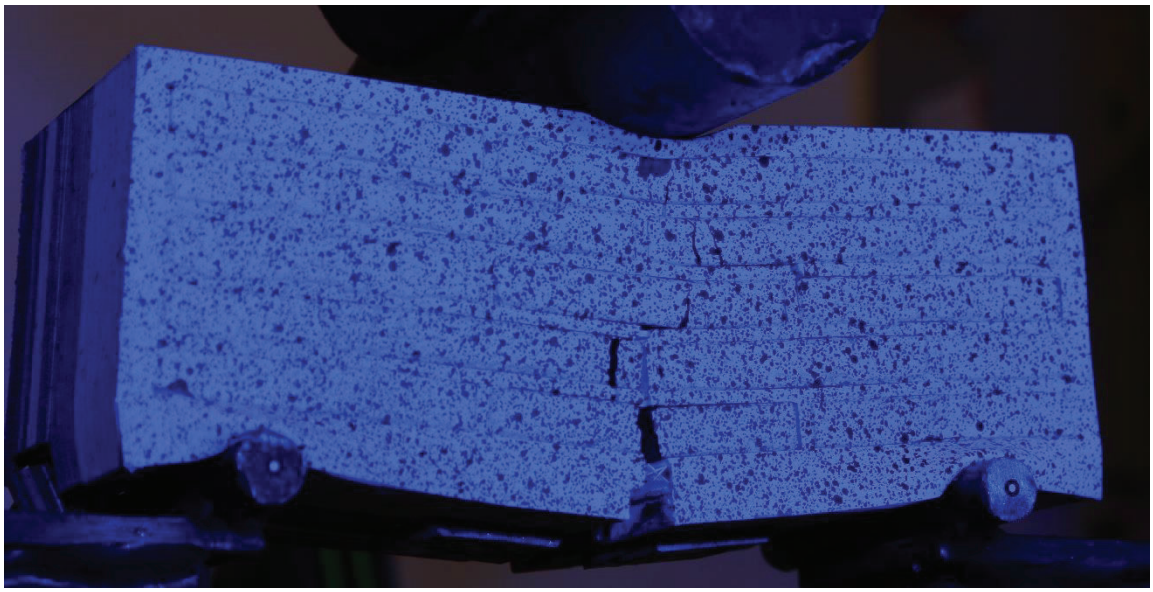

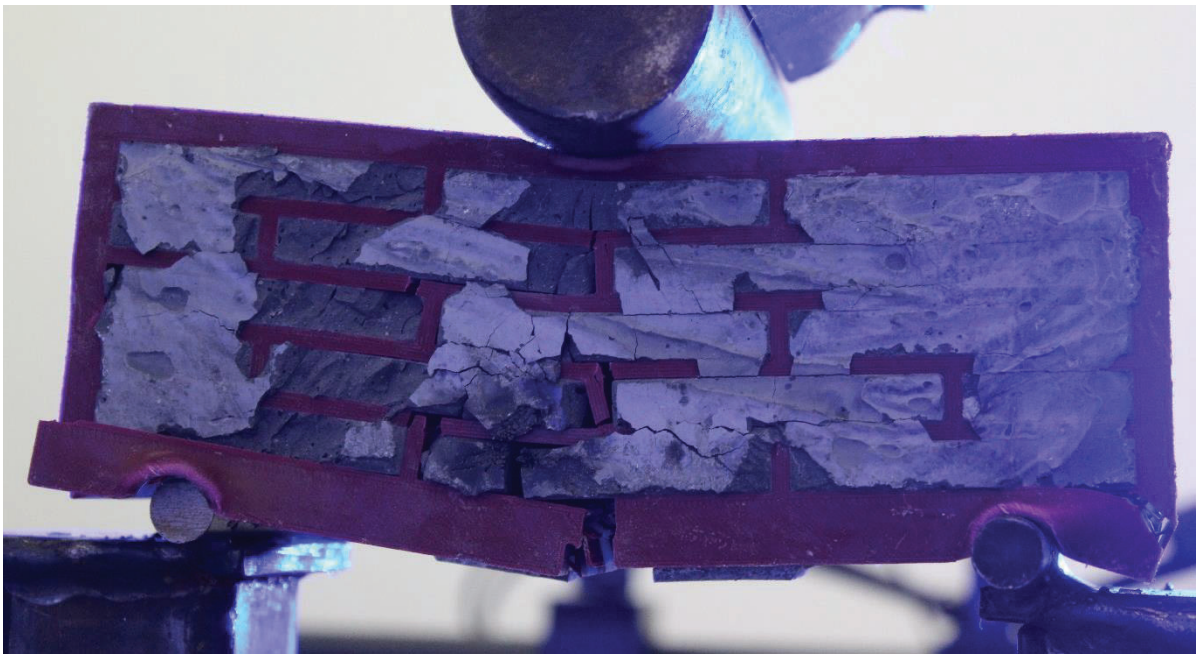

5R-17B-0.1T (2)

After Testing

5R-17B-0.25T (1)

After Testing

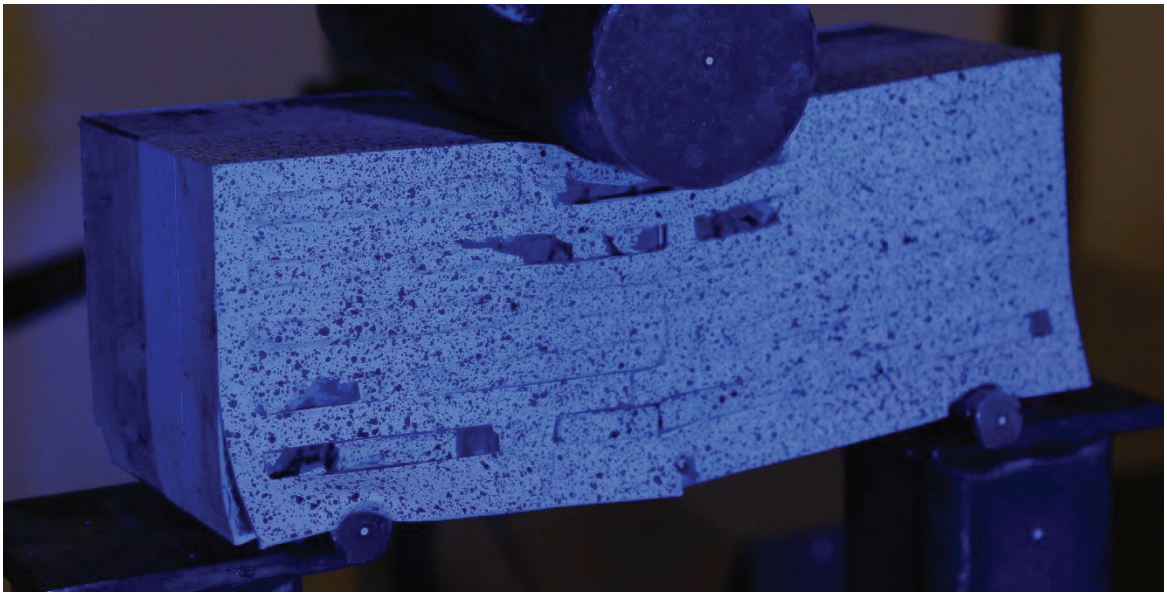

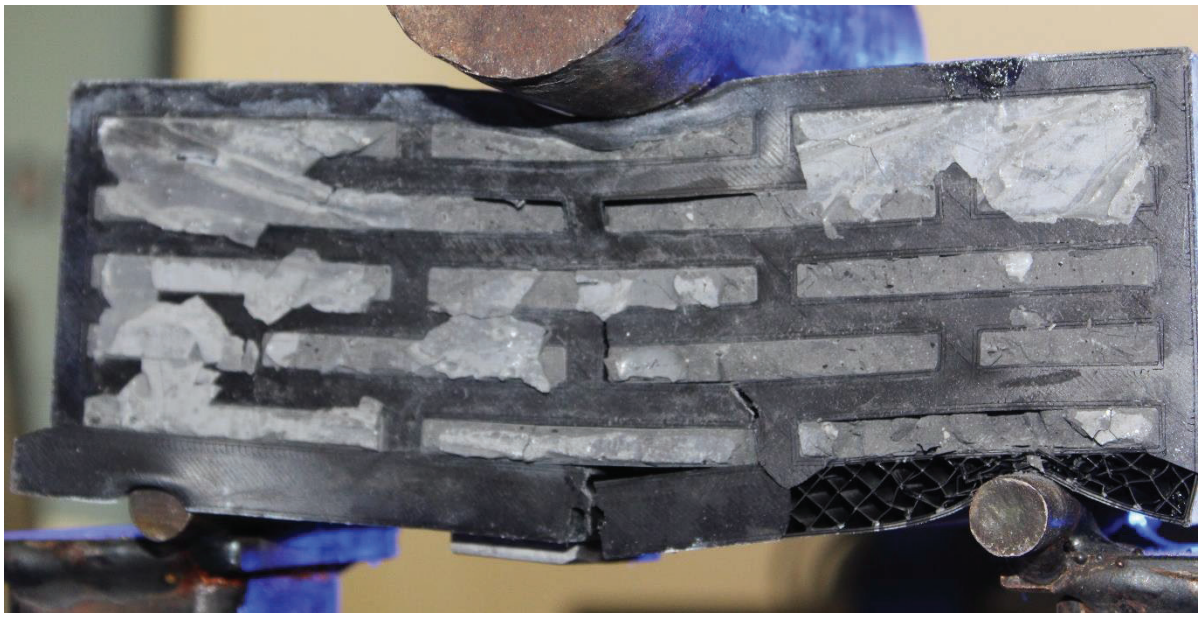

5R-17B-0.25T (2)

After Testing

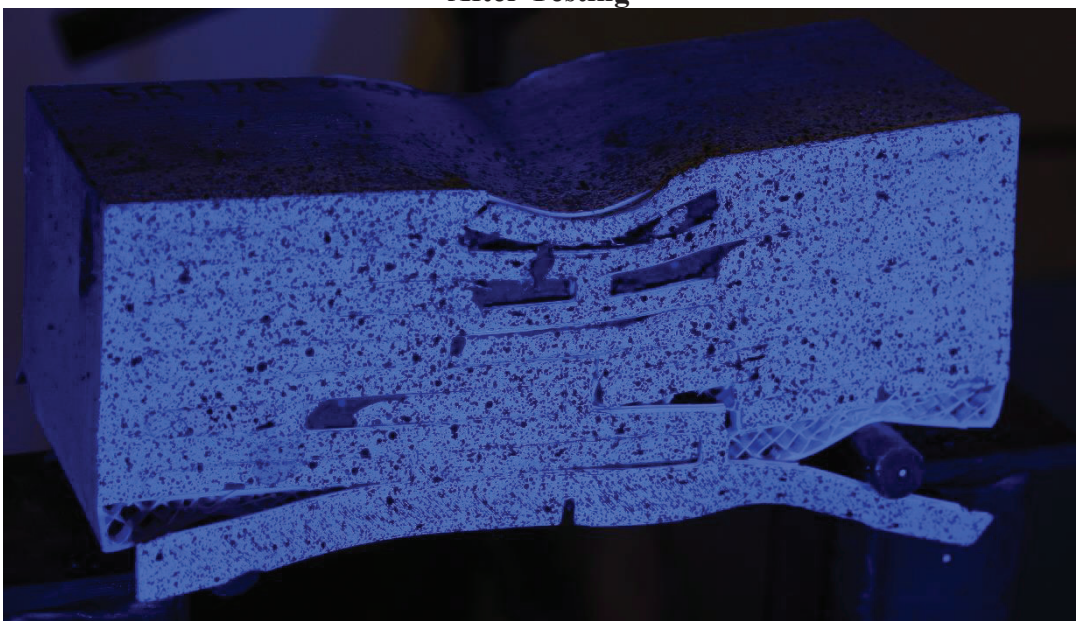

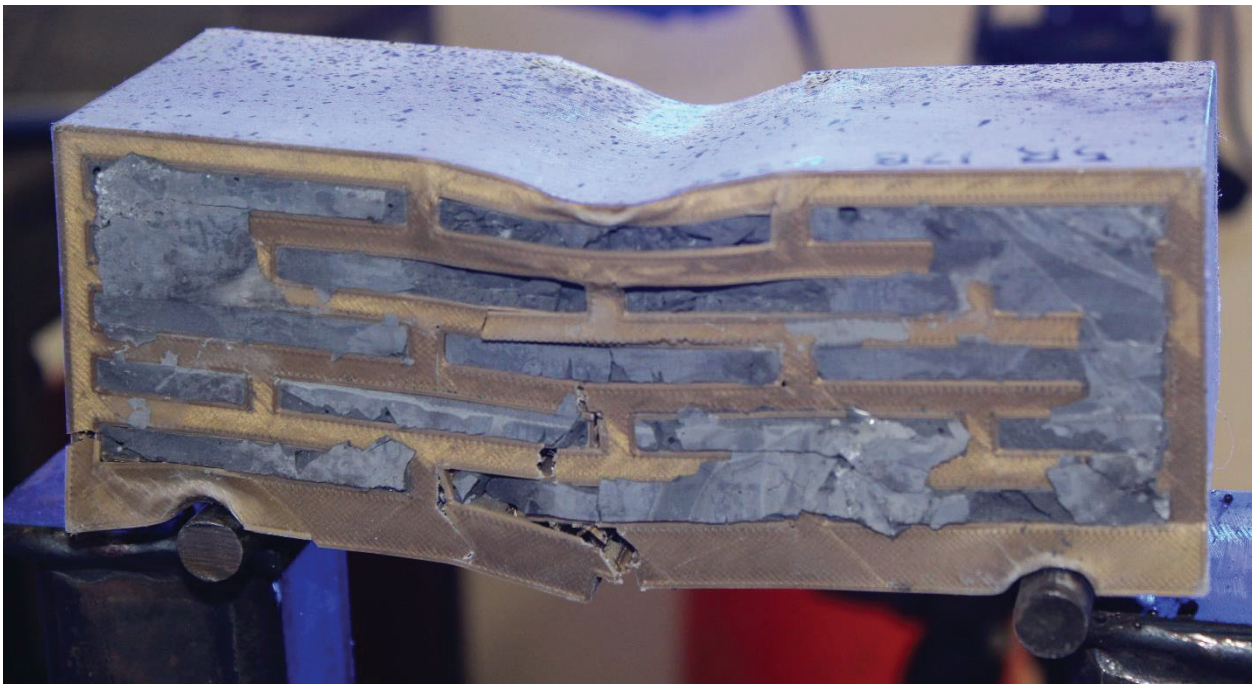

5R-22B-0.25T (1)

After Testing

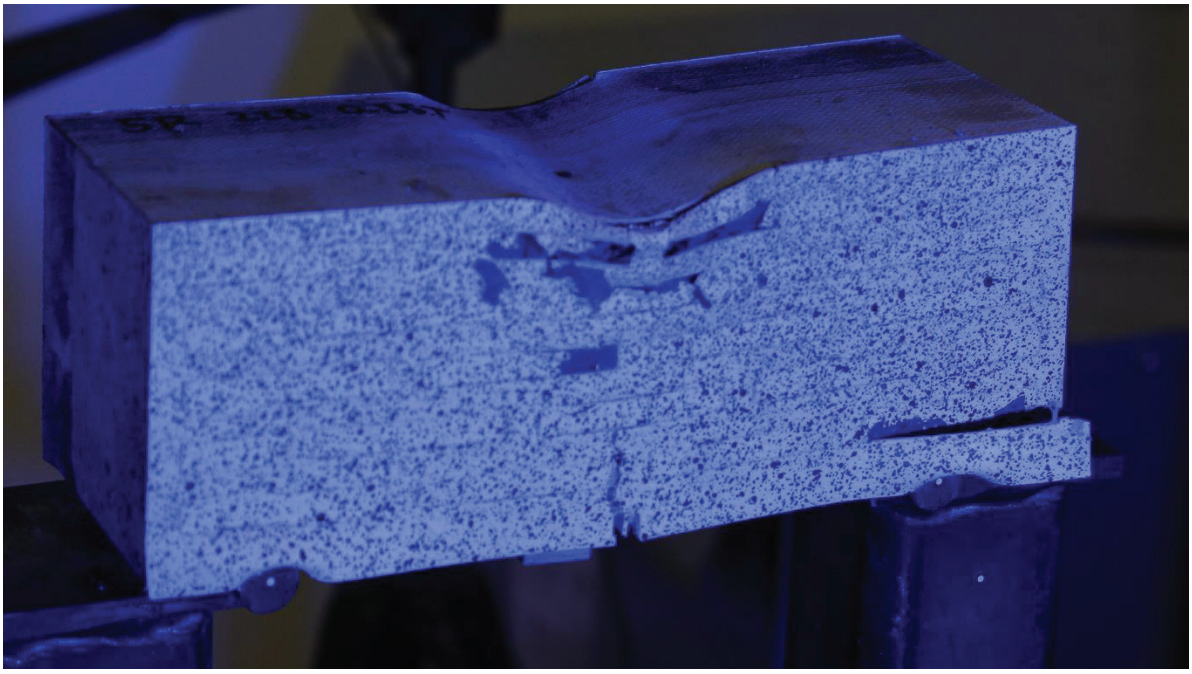

5R-22B-0.25T (2)

After Testing